Politecnico di Torino

Politecnico di Torino

Master's Degree in Mechatronic Engineering

April 2024

High-Performance Torque Control of Electrical Excited Synchronous Motors

Supervisors:

Rubino Sandro

Bojoi Iustin Radu

Mandrile Fabio

Candidate:

Macri' Nicola

Abstract

Energy is a key aspect of maintaining economic growth and daily living. The world's energy system's heavy dependence on fossil fuels has unfortunately directly threatened human existence due to ascending phenomena like air pollution and climate change. The transportation sector is one of the largest consumers of energy and a major contributor to air pollutants and greenhouse gas (GHG) emissions. This is the reason why transport electrification is a highly researched area nowadays.

Nevertheless, the production of electric transport makes use of critical materials, including Rare-Earth Elements (REE), such as ferromagnetic materials, most of which commercial electric motors rely on. REE availability and cost increasingly depend on geopolitical and economic factors.

EESMs (also known as wound-field synchronous motors) have recently been garnering attention from the automotive industry as a compelling permanent magnet-free alternative motor. It replaces PMs with an excitation winding placed on the rotor, and the injected current can be regulated using slip rings or wireless power transfer solutions. This way, the magnetization level can be calibrated at any operating point to maximize motor efficiency.

Currently, the technical literature reports few control algorithms for EESMs able to guarantee high-performance torque regulation in any operating condition, including deep flux weakening under voltage and current constraints imposed by the whole eDrive chain.

This thesis will address the problem and perform advanced elaboration of torque and flux maps of an EESM to support the development of an innovative torque controller characterized by the best dynamic performance of torque regulation in any possible machine's operating point.

Beyond the various torque control algorithms proposed by technical literature, analyzed one by one by means of pros and cons for the specific mission, the choice fell on the recently proposed Flux Polar Control (FPC), which performs torque regulation by directly controlling the stator flux vector in terms of amplitude and load angle, thus involving two control loops. This approach guides through some additional advantages with respect to other solutions (such as CVC, DTC, or DFVC): (i) the performance of the load angle control loop is independent of the machine's operating point, and implementing a normalization to the actual stator flux amplitude, the gains of the load angle regulator are automatically self-calibrated to retain the same dynamic performance in any possible operating point, (ii) MTPV operation can be straightforwardly performed by simply limiting the reference load angle, thus avoiding time-consuming outer regulators. The two control loops feature the same performance, decoupled voltage margins, and independence of the machine's operating point.

FPC properties potentially lead to the highest dynamic performance of torque regulation compared to other proposed control algorithms, with the only drawback of not automatically preserving linearity of torque regulation. Therefore, one of the challenges of this work is to overcome this drawback by computing a proper load angle look-up table, interpolated to get the reference load angle, fulfilled with all the needed constraints.

The proposed methodology is experimentally validated considering, as a case study, the wound field traction motor adopted by Renault ZOE R135.

Contents

List of Figures

List of Tables

Chapter 1

Introduction

1.1 Background

In the last decades planet Earth has suffered human hands, through air and water pollution, land exploitation and other phenomena that lead from greenhouse gases emissions(GHG) to climate change. Even humans have faced the consequences, health is directly compromised by industry and transport noxious emissions, such as CO2, NOX, and worse, particulate matters PM, in the case of 10-100um or <4um. Nowadays, noxious emissions are highly concentrated in the cities, and majority of them yield to transport sector, related to ICE vehicles, which combustion process leads to GHG emissions, as well as CO2 and NOX. Just think about the pandemic in 2020, when transport emissions reached an historical minimum: in the aggregate, surface passenger transport emissions fell by 11.2% corresponding to 40.3 MtCO2 in Europe. This decline was predominantly due to the reduction of private passenger transport in five European countries (France, Germany, Italy, Spain, and the UK). During the first lockdown in April 2020, CO2 emissions from surface passenger transport declined by 50% in Europe, resulting in a 7.1% reduction in total CO2 emissions [3].

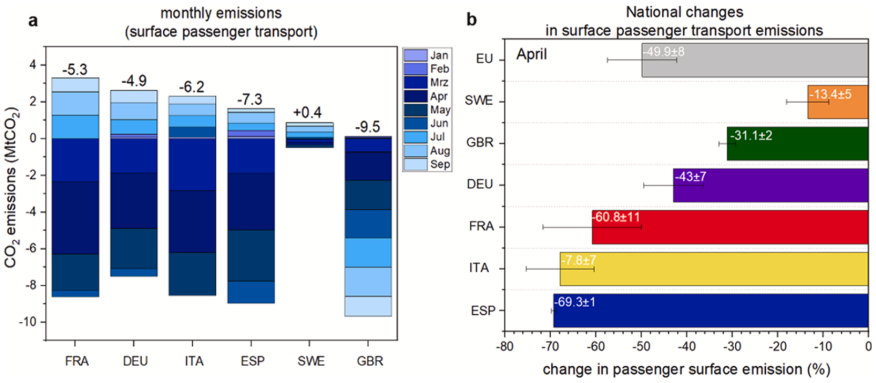

Figure 1.1: monthly changes in surface passenger transport emissions in MtCO2 from January to September (a) and percentage change of total emissions for surface passenger transport in April for individual focus countries (b). High and low estimates, calculated as the standard deviation from the different mobility datasets, are represented by arrow bars [3].

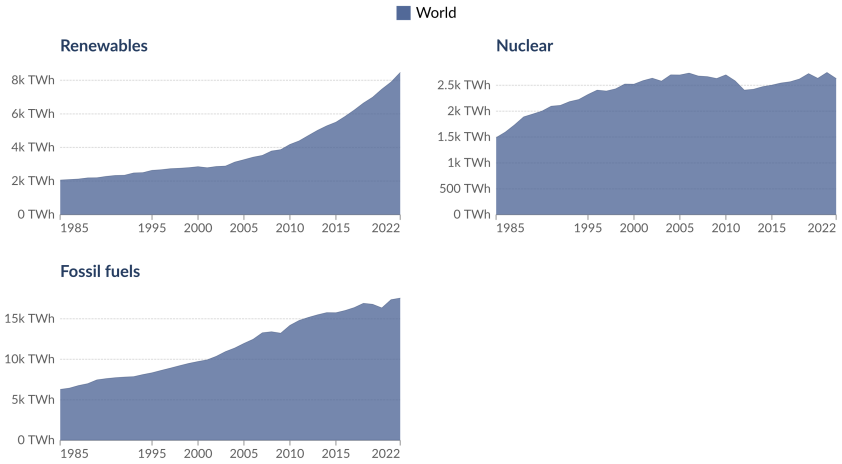

Figure 1.2: Energy sources.

Here electrification pays a crucial role as alternative to common ICE vehicles, since BEVs surely guarantee zero direct emissions. The term direct is expressly used, since energy production related to BEVs can be subjected to fossil fuels consumptions as well, as only a portion if this energy comes from ascending renewable solutions, even though there are controversies about huge drilling operations lead by superpowers. Nevertheless, other drawbacks of BEVs is related to batteries disposal, as well as every elements made with rare earth elements (REE) or other critical elements. Most of the actual BEVs batteries are lithium-ion batteries, also a mix of cobalt, nickel and manganese: materials that have to be mined and extracted, that means land corruption and energy consumption. Be that as it may, almost every electronic device we use every day is supplied by lithium-ion batteries, so it is a problem that science has already taken into account, with ascending more-sustainable methods

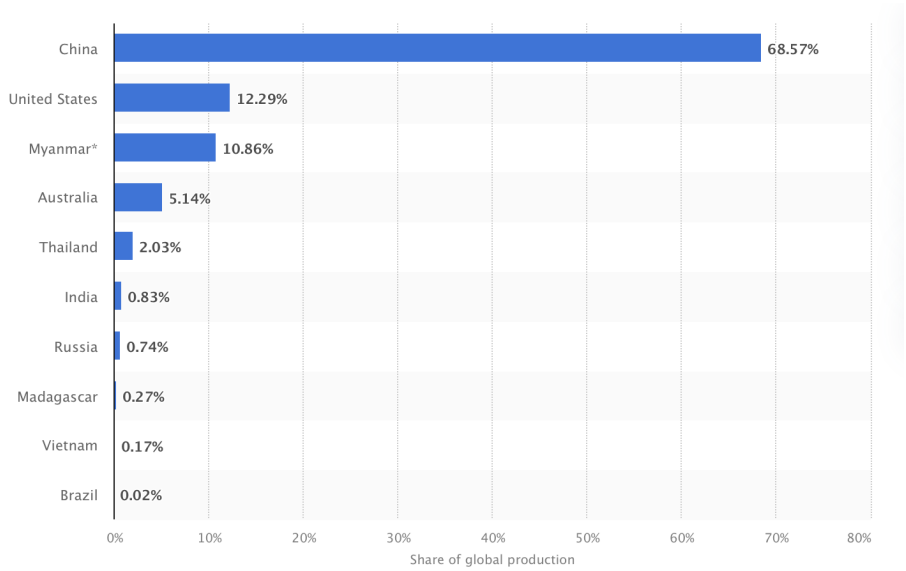

Figure 1.3: Share of REEs global production.

for extracting lithium.

Ensemble, rare earth elements are mostly employed in permanent magnets (PMs) solutions, as majority of actual BEVs are designed on PMs electric motors. REEs are a group of 17 chemical elements considered critical for digitalization and for the energy transition. While called "rare", they are not in fact rare in the Earth's crust and can be found in many places. REEs have unique magnetic, optical and electronic properties that make them crucial (and difficult to substitute) for many uses. However, REE mining has been linked to larger environmental impacts than other minerals and metals. REEs are usually present in very low concentrations and are combined; this means that their extraction and separation are expensive, require large amounts of energy and water, and generate large quantities of waste. Furthermore, they are often mixed with different radioactive and hazardous elements such as uranium, thorium, arsenic and other heavy metals which pose high health and environmental pollution risks. Here we can add their social and economic problems, since, from 2023 data, it is highlighted that REEs production is highly unbalanced, only few countries are contending this market, with huge majority for China and its almost 70% of global production.

1.1.1 Advantages and drawbacks of PMs in automotive field

The wide spreading use of PMs synchronous motors is justified by their advantages: high efficiency even at part load and low speeds, high power density, that also guarantees to reduce motor dimension, one of the main design tasks. Unfortunately, this hides other disadvantages (beyond already mentioned REE problem): (i) PMs are highly influenced by temperature with lower performance index as it increases, and together with high magnetic field exposure, it can lead to lower torque capability and demagnetization phenomena; (ii) one of the most welcomed SMs feature is their flex weakening capability, i.e. reduction of the magnetic flux in order to reach speeds beyond base speed, while injecting additive currents to contrast PMs flux. Indeed, PMs magnetic field cannot be modulated, and the procedure may be complex and energetically expensive, as well as including the risk of demagnetization.

In this context, alternatives to PMSMs can be identified, for instance, in induction motors, reluctance motors, or PMSMs made up without REEs, in the case of ferrite-based motors. Therefore, an ascending alternative, already dimly embedded in the BEVs market, can be found on Wound Field Synchronous Motors (WFSM, also known as Electrical Excited Synchronous Motors, EESM): thesis work will face a WFSM overview, focusing on torque control performed on Renault ZOE 135, topic supplied by the lack of a wide technical literature about high performance torque control algorithms.

1.2 WFSM overview

As already mentioned, WFSMs main difference with respect to PMs solutions, is the lack of magnets right behind a wounded rotor, supplied in DC to generate and excitation field in the airgap. Usually, and as the case of Renault ZOE, excitation system consists on sliding contacts between stationary graphite brushes and rotating slip rings: one of the characteristic that shows both benefits and drawbacks for this machine.

Indeed, high controllability of the excitation field brings some of the advantages we can't find in PMs solutions: (i): preserved safety related to the possibility to overcome uncontrollable generation operations, removing the source of excitation, while PMs cannot be shut down; (ii) maximum torque won't be limited by the current rating of the source, as high torques can be reached also at low speeds; (iii) high pawer factors can be reached, regulating reactive power exchanged by the machine through the rotor current; (iv) more flexible flux weakening operations,

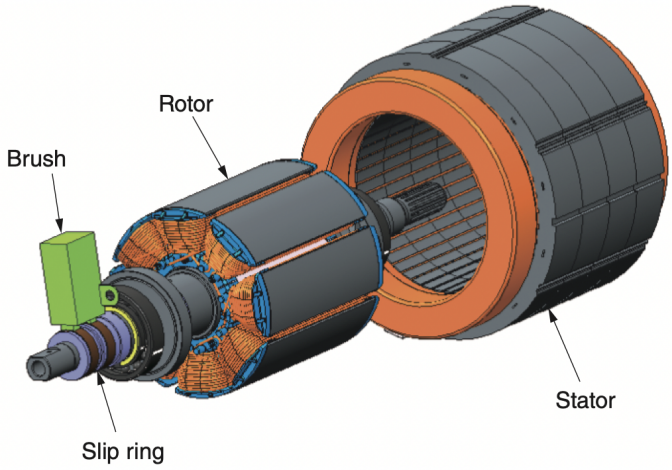

Figure 1.4: WFSM external appearance.

since magnetic flux can be easily reduced controlling the field current. Despite the canonic synchronous machines models, the one related to WFSMs introduce a third degree of freedom beyond the field current (rotor current), and its influence on other electrical parameters shows one of the main control challenges.

First approach to control field requires the knowledge of the machine and its magnetic model, so interaction between stator and rotor currents and fluxes: next pages will focus on WFSM's magnetic model exploitation.

Technical literature proposes approaches based on space vectors analysis, starting from a three-phase supply system, then turned in dq reference frame coordinates: at steady-state, the space vectors of current, flux and voltage rotate at the electrical synchronous speed

$$\omega = pp \cdot \omega_m$$

where ω_m is the mechanical synchronous speed. Here, it's convenient to model the machine in a rotating reference frame synchronous with w, and so is the dq reference frame. Indeed, at steady-state, for a balanced operations with sinusoidal phase quantities, dq ones become DC. Voltage equations show up that quantity in each phase is represented both by voltage drop across the stator (and rotor, for an EESM, i.e. joule losses), and flux linkage variation (induced electro-motive force):

$$\begin{aligned} v_a &= R_s \cdot i_a + \frac{d\lambda_a}{dt} \\ v_b &= R_s \cdot i_b + \frac{d\lambda_b}{dt} \\ v_c &= R_s \cdot i_c + \frac{d\lambda_c}{dt} \end{aligned} \tag{1.1}$$

Moreover, the model is usually expressed in matrix form, as follows

$$\begin{bmatrix} v_a \\ v_b \\ v_c \end{bmatrix} = R_s \cdot \begin{bmatrix} i_a \\ i_b \\ i_c \end{bmatrix} + \frac{d}{dt} \cdot \begin{bmatrix} \lambda_a \\ \lambda_b \\ \lambda_c \end{bmatrix} \tag{1.2}$$

where EMFs are equivalent to three voltage generators, imposing a voltage equal to the derivative of the flux linkage, as it is *speed dependant*. Now, direct Clarke Transformation is applied [ref], to get $\alpha\beta$ frame, then dq frame, just rotating it by the electrical angular position θ: since

$$\begin{aligned} \mathbf{v}_{\alpha\beta} &= R_s \cdot \mathbf{i}_{\alpha\beta} + \frac{d}{dt}\lambda_{\alpha\beta} \\ \mathbf{v}_{\alpha\beta} &= \mathbf{v}_{dq} \cdot e^{j\theta} \\ \mathbf{i}_{\alpha\beta} &= \mathbf{i}_{dq} \cdot e^{j\theta} \\ \lambda_{\alpha\beta} &= \lambda_{dq} \cdot e^{j\theta} \end{aligned} \tag{1.3}$$

then

$$\mathbf{v}_{dq} \cdot e^{j\theta} = R_s \cdot \mathbf{i}_{dq} \cdot e^{j\theta} + \tfrac{d}{dt}(\lambda_{dq} \cdot e^{j\theta})$$

that leads to the voltage equation in dq frame

$$\mathbf{v}_{dq} = R_s \cdot \mathbf{i}_{dq} + \frac{d}{dt}\lambda_{dq} + j \cdot \omega\lambda_{dq} \tag{1.4}$$

$$\begin{bmatrix} v_d \\ v_q \end{bmatrix} = R_s \cdot \begin{bmatrix} i_d \\ i_q \end{bmatrix} + \frac{d}{dt} \begin{bmatrix} \lambda_d \\ \lambda_q \end{bmatrix} + \mathbf{\Omega} \begin{bmatrix} \lambda_d \\ \lambda_q \end{bmatrix}$$

where

$$\mathbf{\Omega} = \begin{bmatrix} 0 & -1 \\ 1 & 0 \end{bmatrix}$$

Voltage equations in dq are valid for permanent magnets SMs, and they are represented by three terms: stator resistance voltage drop (jaule losses), dq flux variation (load variation), and a speed dependant motional term. Magnetic model is instead expressed in terms of leakage flux linkages and magnetizing flux linkages, in abc frame:

$$\begin{bmatrix} \lambda_a \\ \lambda_b \\ \lambda_c \end{bmatrix} = L_{ls} \cdot \begin{bmatrix} i_a \\ i_b \\ i_c \end{bmatrix} + \begin{bmatrix} M_{aa} & M_{ab} & M_{ac} \\ M_{ba} & M_{bb} & M_{bc} \\ M_{ca} & M_{cb} & M_{cc} \end{bmatrix} \begin{bmatrix} i_a \\ i_b \\ i_c \end{bmatrix} + \begin{bmatrix} \lambda_{m,a} \\ \lambda_{m,b} \\ \lambda_{m,c} \end{bmatrix} \tag{1.5}$$

where L_{ls} is the leakage phase inductance, and $M_{ij}, i = a, b, c, j = a, b, c$ are the magnetizing self and mutual inductances. Trying to bring magnetic model in dq

frame, as already seen for voltage equations, shows up a simpler model, at the cost of adding a motional term in previous equations:

$$\begin{bmatrix}\lambda_d\\ \lambda_q\end{bmatrix} = \begin{bmatrix}L_d & 0\\ 0 & L_q\end{bmatrix}\begin{bmatrix}i_d\\ i_q\end{bmatrix} + \begin{bmatrix}\lambda_{m,d}\\ \lambda_{m,q}\end{bmatrix} \tag{1.6}$$

At steady-state, vectorial equations in dq frame can be written in a more compact form

$$\begin{aligned}\mathbf{v} &= \mathbf{R}\mathbf{i} + \mathbf{\Omega}\lambda\\ \lambda &= \mathbf{L}\mathbf{i} + \mathbf{M}\mathbf{i}\end{aligned} \tag{1.7}$$

In the case of a Wound Field Synchronous motor, an additional degree of freedom is introduced by the rotor and its magnetic field:

$$\mathbf{v} = \begin{bmatrix}v_d\\ v_q\\ v_f\end{bmatrix}, \mathbf{i} = \begin{bmatrix}i_d\\ i_q\\ i_f\end{bmatrix}, \lambda = \begin{bmatrix}\lambda_d\\ \lambda_q\\ \lambda_f\end{bmatrix}$$

$$\mathbf{R} = \begin{bmatrix}R_s & 0 & 0\\ 0 & R_s & 0\\ 0 & 0 & R_f\end{bmatrix}, \mathbf{\Omega} = \begin{bmatrix}0 & -\omega & 0\\ \omega & 0 & 0\\ 0 & 0 & 0\end{bmatrix}$$

$$\mathbf{L} = \begin{bmatrix}L_d & 0 & 0\\ 0 & L_q & 0\\ 0 & 0 & L_f\end{bmatrix}, \mathbf{M} = \begin{bmatrix}0 & 0 & M_{sr}\\ 0 & 0 & 0\\ \frac{3}{2}M_{sr} & 0 & 0\end{bmatrix}$$

From which the system of equations can be written as

$$\begin{cases}v_d = R_s \cdot I_d - \omega \cdot \lambda_q\\ v_q = R_s \cdot I_q + \omega \cdot \lambda_d\\ v_f = R_f \cdot I_f\end{cases} \quad \begin{cases}\lambda_d = L_d \cdot I_d + M_{sr} \cdot I_r\\ \lambda_q = L_q \cdot I_q\\ \lambda_f = L_f \cdot I_f + \frac{3}{2}M_{sr} \cdot I_d\end{cases} \tag{1.8}$$

Here iron magnetic saturation is not included for sack of simplicity: for certain kind of motors, like Synchronous Reluctance Motors, or WFSMs, current-to flux relationship is highly non-linear, inductance varies with the applied current. Owing to this phenomenon, called *cross saturation*, flux on each axis depends on current of both axes, and, in the case of WFSM, it's also depending on the field current. Approaches for saturated magnetic model usually involve representing the flux maps as look-up tables (LUT), as they are usually considered in torque controller, for torque linearization purposes.

One of the goals of this thesis will be also to handle an highly saturated machine like WFSM: 2nd chapter will face the challenge to get measurements of current and fluxes, then build flux maps as LUTs taking into account all of the saturation effects.

Moreover, electromagnetic torque is expressed behind the general formula, valid for SMs of al kind

$$\mathbf{T} = \frac{3}{2} \cdot p \cdot (\overline{\lambda} \times \overline{i}) = \frac{3}{2} \cdot p \cdot (\lambda_{\mathbf{d}} \cdot \mathbf{I_q} - \lambda_{\mathbf{q}} \cdot \mathbf{I_d}) \tag{1.9}$$

Important considerations about this formula can arise when substituting λ_d and λ_q from (eq), leading to

$$\mathbf{T} = \tfrac{3}{2} \cdot p \cdot (\mathbf{M_{sr}} \cdot \mathbf{I_f} \cdot \mathbf{I_q} + (\mathbf{L_d} - \mathbf{L_q}) \cdot \mathbf{I_d} \cdot \mathbf{I_q})$$

Notice that electromagnetic torque is composed of two terms, derived from rotor magnetic field and motor anisotropy, in the general case of $L_d \neq L_q$, as for example, is the case of Permanent Magnet Syncrhonous Reluctance Machine (PMSyR), with the difference in the lack of magnets and a variable rotor magnetic field.

Indeed, rotor magnetic field variation with the applied excitation field current $\mathbf{I_f}$ makes different types of torque productions, in the case: (i) supposing *zero rotor current*, torque production is only handled by rotor anisotropy, torque profile results symmetrical with respect to *q-axis* (Fig.1.5),and the machine behaves like a syncrhonous reluctance motor (SyR); (ii) increasing rotor current, avoiding too strong ones and machine saturation, torque profile tends to be asymmetrical with respect to *q-axis*, apporaching towards negative *d-axis*(Fig.1.5). In this case, *d-axis* inductance is greater than *q-axis*, leading to

$$L_d - L_q > 0$$

From (torque eq) can be deduced that positive values of currents in *d-axis* lead to higher torque production; (iii) too high field current values lead to to the condition

$$L_d \approx L_q$$

and no reluctance torque production, just where the machine behaves like a Surface Mouted Permanent Magnets Motor (IPM).

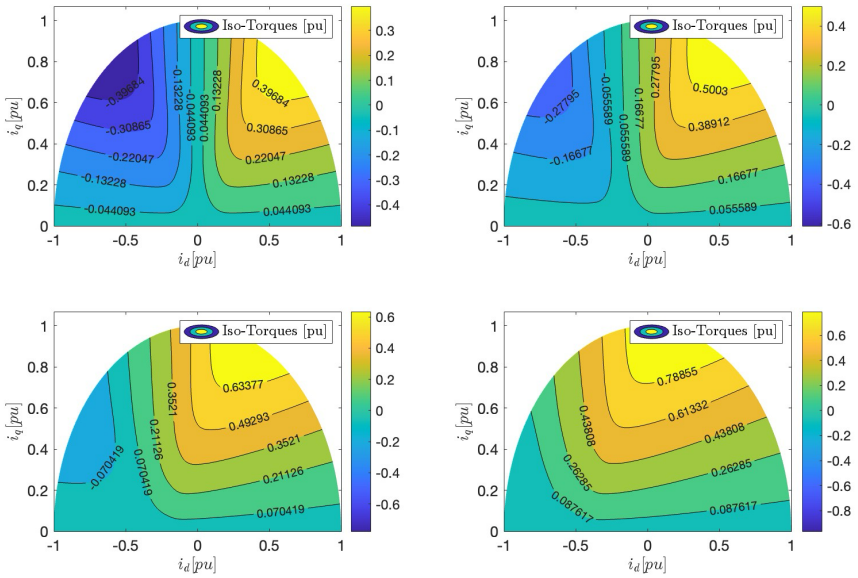

Figure 1.5: Per-unit torque profiles for $\mathbf{I_f}$ = 0pu,0.2pu,0.6pu,1pu

1.3 Control Perspective

Last section's aim was to describe equations of a general synchronous machine in dq frame, focusing con the WFSM case. Motor modelling is a necessary approach is several fields, including control. All the vector control techniques, different methods to abtain desired torque from the AC motor drive, require knowledge of the machine electrical and magnetic parameters. Furthermore, torque controllers must be established to satisfy other demanding requirements: (i) performance of all inner control loops of the torque controller and regulators should be independant of the machine's operating point, in order to avoid tuning procedures [2]; (ii) high performances of torque regulation must be kept in any operating condition, including deep flux weakening; (iii) least but not last, torque control must be easy to implement in terms of control scheme, minimizing the number of control modules.

1.3.1 Fundamentals of torque control

Torque control needs a reference torque T^*, imposed by the user, in order to set reference phase voltages v^*_{abc}, fed to the Voltage Source Inverter directly interfaced with the motor itself. Indeed, VSI acts like a voltage regulator, since it phisically imposes phase voltages v_{abc} to the motor.

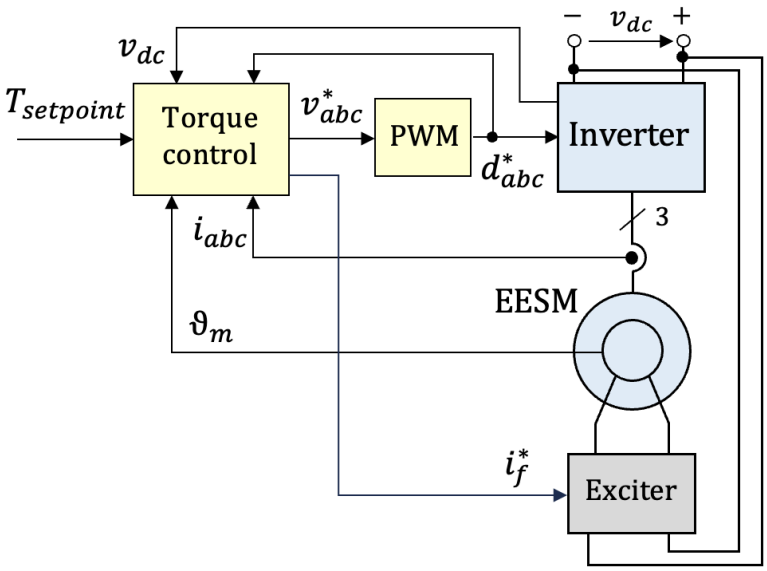

Figure 1.6: WFSM drivetrain block scheme.

Torque control algorithms are implemented in a MCU that generates proper control signal for power electronics, considering the whole eDrive chain (Fig.1.6).
Once established that control input is the reference torque $\mathbf{T}^*$, aspect shared between all torque control algorithms, proper voltages are imposed to the VSI through different methods, according to the algorithms. Indeed, torque control can be also turned in indirect control, where reference torque generates other electrical or magnetic reference quantities.
Literature provides several control algorithms able to satisfy all the mentioned requirements and constraints, and the main practical difference between them is to find into reference quantities to control: proposed control algorithms in this thesis are Current Vector Control (CVC-FOC), Direct Torque Control (DTC) and Flux Polar Control (FPC), where, for the specific purpose, only FPC will be considered.

All of the three mentioned control algorithms are briefly analyzed, with their benefits and drawbacks.

1.3.2 CVC-FOC

Current Vector Control (CVC, also known as Field Oriented Control, FOC) acts in rotor dq frame, indirectly controlling torque by generating stator current vector references, from torque reference.

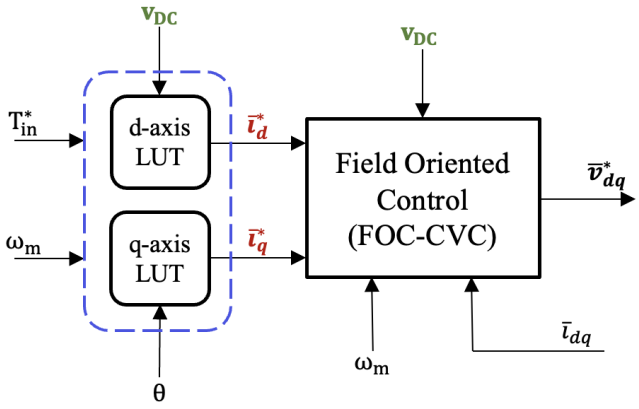

Figure 1.7: CVC-FOC control scheme.

As shown in the block scheme, reference currents are computed by means of look-up tables, so torque regulation is always linearized, even in presence of saturated machines (e.g. SyR, PMSyR, WFSM and so on). LUTs computation is crucial and its employment is justified by their possibility to regulate including all the needed constraints, such as maximum current and converters voltages, as well as MTPA, MTPV and minimum losses.
The control algorithm is analyzed through machine's magnetic model, exploiting the differential equations: for CVC-FOC, focusing on current ones.
Starting from voltage equations exploited in previous section (1.4) for a general SM in dq frame it's possible to represent them in state-space:

$$\begin{cases} l_{eq,d} \cdot \frac{d}{dt} i_d = -R_s \cdot (i_d - \frac{l_{dq}}{l_{qq}} \cdot i_q) + u_d - \frac{l_{dq}}{l_{qq}} \cdot u_q \\ l_{eq,q} \cdot \frac{d}{dt} i_q = -R_s \cdot (i_q - \frac{l_{qd}}{l_{dd}} \cdot i_d) + u_d - \frac{l_{qd}}{l_{dd}} \cdot u_d \end{cases} \tag{1.10}$$

where $l_{eq,d}$ and $l_{eq,q}$ are the equivalent differential inductances along axis d and q, respectively, computed from the differential inductances of the machine as [5]

$$l_{eq,d} = l_{dd} - \frac{l_{dq} \cdot l_{qd}}{l_{qq}}, \quad l_{eq,q} = l_{qq} - \frac{l_{dq} \cdot l_{qd}}{l_{dd}} \tag{1.11}$$

while u_d and u_q are represented by

$$u_d = v_d + \omega \cdot \lambda_q, \quad u_q = v_q - \omega \cdot \lambda_d \tag{1.12}$$

Then, if some simplifications are applied: cross-saturation inductances are neglected since they don't have a significant impact in steady state, follows resistive voltage drop, neglected as well. Equation (1.10) becomes

$$\begin{cases} l_{dd} \cdot \frac{d}{dt} i_d \simeq v_d + \omega \cdot \lambda_q \\ l_{qq} \cdot \frac{d}{dt} i_q \simeq v_q - \omega \cdot \lambda_d \end{cases} \tag{1.13}$$

Together with the benefits of using LUTs, CVC allows also to establish simple regulators to compute reference voltages from reference currents (current regulators), such as PI regulators. Nevertheless, equation (1.13) shows that perofmance of each current control loop is dependant on differential inductances on both axis (values that vary with the applied current, as already mentioned): the gains of the control loops must be adapted to the machine's operating point, avoiding instability.

1.3.3 DTC-DFVC

On the other hand, the principle of DTC is to directly select voltage vectors from reference torque and flux, then voltages can be reconstructed in different ways. Literature proposes hysteresis regulator followed by LUTs, but this solution leads to a variable swithing frequency f_{sw} of the VSI feeding the motor, then leading to torque ripple.

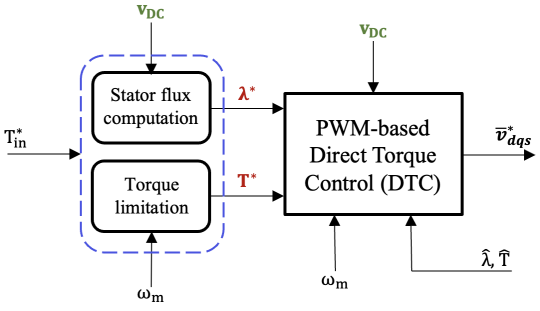

Figure 1.8: PWM-based DTC scheme.

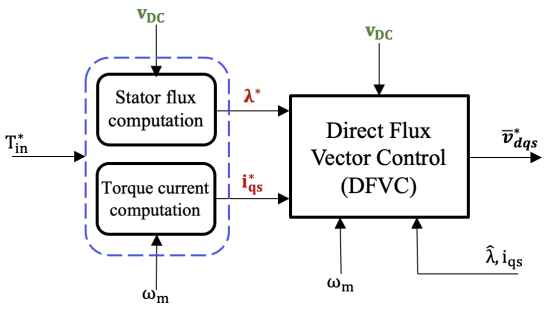

Figure 1.9: DFVC scheme.

Nevertheless, pros and cons are analyzed taking into account a PWM-based DTC solution (Fig.1.8), where a pulse with modulator si implemented, leading to constant switching frequency and low torque ripple.
Here, state space representation is built up from a different reference frame with respect to CVC-FOC, as it is exploited in stator *dqs* frame: since *ds* axis corresponds to the stator flux vector, and its angular displacement from d axis is the load angle

$$\delta = \angle(\lambda_d, \lambda_q) \tag{1.14}$$

voltage equations are obtained computing rotational transformation by angle δ, from (1.4), thus obtaining

$$\begin{cases} v_{ds} = R_s \cdot i_{ds} + \frac{d}{dt}\lambda \\ v_{qs} = R_s \cdot i_{qs} + \lambda \cdot \frac{d}{dt}\delta + \omega \cdot \lambda \end{cases} \tag{1.15}$$

where λ represents the amplitude of the magnetic flux linkage in *ds* axis. Neglecting resistive voltage drops the flux linkage state equations is

$$\frac{d}{dt}\lambda \simeq v_{ds} \tag{1.16}$$

While the latter needs general torque equation (1.9), that, in this coordinate system becomes

$$\mathbf{T} = \frac{3}{2} \cdot p \cdot (\overline{\lambda} \times \overline{i}) = \frac{3}{2} \cdot p \cdot \lambda \cdot i_{qs} \tag{1.17}$$

Here, PWM-based DTC acts directly on torque, while, other solutions, like DFVC, here act on *qs* current: analyzing i_{qs} state equation allows to exploit benefits and drawbacks of both DTC and DFVC. Torque equation (1.17) is modified including i_{qs} in order to give emphasys on DFVC as well.
Applying rotational transformation by load angle δ to (1.13):

$$l_{qs} \cdot \frac{d}{dt} i_{qs} \simeq -i_{ds} \cdot l_{qs} \cdot \frac{d}{dt}\delta + k_{ds} \cdot v_{ds} + (v_{qs} - \omega \cdot \lambda) \tag{1.18}$$

where l_{qs} is the equivalent differential inductance along *qs* axis, and k_{ds} is the voltage coefficient:

$$l_{qs} = \frac{2 \cdot l_{dd} \cdot l_{qq}}{l_{dd} + l_{qq} - (l_{qq} - l_{dd}) \cdot \cos(2 \cdot \delta)} \tag{1.19}$$

$$k_{ds} = \frac{(l_{qq} - l_{dd}) \cdot \cos(2 \cdot \delta)}{(l_{qq} + l_{dd}) \cdot \cos(2 \cdot \delta) - (l_{dd} + l_{qq})} \tag{1.20}$$

Since load angle variation acts like an additive disturbance that vanishes at steady-state, and v_{ds} is negligible as just compensate for resisitve voltage drops (according to (1.15)), equation (1.18) becomes:

$$l_{qs} \cdot \frac{d}{dt} i_{qs} \simeq v_{qs} - \omega \cdot \lambda \tag{1.21}$$

Then, applying time derivative to torque equation (1.17) and replacing i_{qs}, state space equation is:

$$\frac{2}{3 \cdot p} \cdot \frac{d}{dt} T \simeq v_{ds} \cdot i_{qs} + \frac{\lambda}{l_{qs}} \cdot (v_{qs} - \omega \cdot \lambda) \tag{1.22}$$

Again, neglecting ds axis voltage:

$$\left(\frac{2 \cdot l_{qs}}{3 \cdot p \cdot \lambda} \right) \cdot \frac{d}{dt} T \simeq v_{qs} - \omega \cdot \lambda \tag{1.23}$$

From the above equations arise several benefits of this control algorithm: torque regulation linearity is always preserved, even in deep FW operations (no need to implement LUTs), since qs axis current can be computed according to (1.17), taking care about limiting reference to all the machine constraints; at same time, equation (1.16) shows that dynamic performance of closed loop control is independant on machine's operating point, where voltage v_{ds} can be reconstructed as derivative of stator flux amplitude; dq axis current and flux amplitude regulators for DFVC operate with decoupled voltage margins, leading to high control dynamics, according to voltage equations in (1.15).
Together with these benefits, DTC and DFVC exhibits the following disadvantages: if an outer heuristic regulator is not included to limit load angle during FW operations, its tuning needs a LUT; performances in qs axis can be critical due to the dependance on the higly nonlinear behavior of l_{dq}, as well as flux linkage dependance. Thus, qs axis regulators must be tuned depending on the operating point.

1.3.4 FPC

Flux Polar Control performs torque regulation by directly acting on the stator flux, in terms of amplitude λ and load angle δ. As the case of DTC-DFVC schemes, FPC operates in dqs reference frame, where qs axis voltage equation is used to perform closed loop control of machine's load angle. According to dqs reference frame voltage equations (1.15), load angle state-space equation is obtained as:

$$\lambda \cdot \frac{d}{dt}\delta \simeq v_{qs} - \omega \cdot \lambda \tag{1.24}$$

where stator resistive voltage drop is considered negligible.

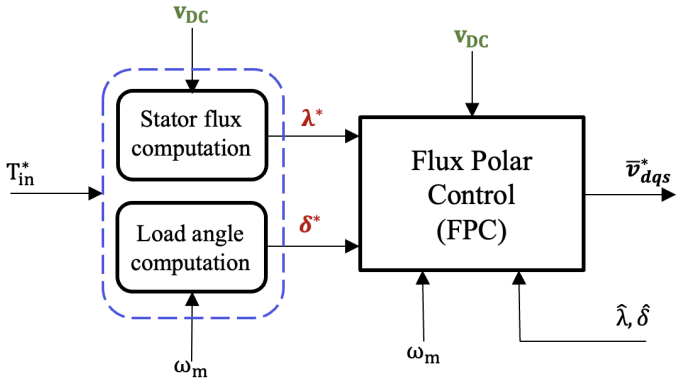

Figure 1.10: FPC scheme.

The other state space equation, reported in (1.16), already represents one of the FPC advantages, that is the presence of just two control loops, related to load angle and flux. Noteworthy is now the possibility to regulate load angle δ in order to satisfy MTPV constraints, thus without need to include other outer regulators.
Moreover, according to (1.24), the performance of load angle regulator is independant on the machine's operating point, after implementing a normalization to the actual stator flux amplitude.
Together with decoupled voltage margins (as happens for DTC-DFVC), all the proposed benefits lead FPC to the highest dynamic performance of torque regulation, and this is the reason why, in this thesis work, Flux Polar Control is implemented to face the WFSM control challenge.
Flux Polar Control detailed implementation is summaried in the following chapters:

Chapter 2: The importance of magnetic model identification for control purposes has been already mentioned in the introduction. Chapter 2 will face the challenge of magnetic model identification from measurements, with an approach valid for synchronous machines of all kind.

Chapter 3: Chapter 3 describes for the first time the eDrive block scheme, without focusing on the control block. Hence, how converters and synchronous motor are modelled for control purposes. Converters, motor and references are grouped in order to get a first simulation of the drive.

Chapter 4: Chapter 4 aims to shed light on all we need to implement FPC, i.e. MTPA, MTPV, MTPS, MEPT profiles, as well as load angle LUT. At the end, a constrained magnetic model (control maps) is obtained.

Chapter 5: Once control maps are properly computed, chapter 5 presents FPC implementation, block scheme, and simulation test in a continuous time domain. Then, since MCU implementation needs digital signals (i.e. discrete-time), control discretization is needed and implemented.

Chapter 6: Final chapter reports a working enviroment able to perform Chapter 5 simulations on a real EESM adopted by Renault Zoe 135.

Chapter 2

Magnetic Model Identification

2.1 Identification of magnetic model for syncrhonous machines

Identification of relationship between currents and flux linkages in a syncrhonous motor is a crucial aspect for design and control purposes. At same time, this approach brings nontrivial efforts, especially when handling highly saturated machines, as the case of WFSM. For this reason, the general approach proposed in [1] comes with the assumption that dq machine fluxes are a nonlinear function of dq currents. Here is presented an experimental approach, where the machine is running at steady-state speed and current, and flux linkages

$$\begin{cases} \lambda_d = f(i_d, i_q) \\ \lambda_q = g(i_d, i_q) \end{cases} \tag{2.1}$$

are obtained from voltages $\mathbf{v_{dq}}$. Model evaluation turns out to be in a dq currents rectangular domain, limited by maximum values i_{dmax}, i_{qmax} which points distribution depends on desired maps resolution. For sack of simplicity, the procedure is explained for a general SM in dq axis, and it is repeated for each field current value, since the further degree of freedom suggests that fluxes are function of three currents (i_d, i_q, i_f).

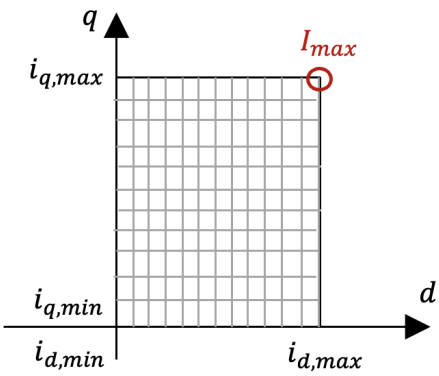

Figure 2.1: example of dq current mesh.

However, considering a rectangular currents domain (as shown in fig(2.1)) for identification procedures, when indetifying at map edges, maximum current won't be equal to $I_{dq,max}$, since it's given by

$$I_{max} = \sqrt{i_{d,max}^2 + i_{q,max}^2} = \sqrt{2} \cdot I_{max} \tag{2.2}$$

It means that, when testing the maximum overload point for current grid, losses are almost doubled with respect to maximum affordable current, that could lead to irreversible motor damaging.

For this reason is recommended to identify magnetic model starting from a *polar domain*, since model identification will be always within the range of maximum available current. Obviously, turns out that domain is now irregular, but it happens only in dq plane, not the case of amplitude and angle:

$$I_s \in [0, I_{max}]$$
$$A_s \in [0, 180°]$$

Just to make a short example, considering a stator resistance

$$R_s = 5m\Omega$$

And a maximum current amplitude

$$I_{max} = 800A$$

Testing the model in the point of maximum current amplitude produces joule losses related to stator resistance, that in this case are given by the following:

$$P_{js} = \frac{3}{2} \cdot R_s \cdot I_{max}^2$$

A single test produces around 5kW of losses, but if a rectangular domain is considered, losses are almost doubled, according to (2.2).

Independantly on the kind of domain that is considered, magnetic model identification is performed starting from a machine under test (MUT) connected with another motor (usually a bigger one), the driving machine, that imposes the MUT speed.
MUT is driven by a VSI, to control the injected currents on d and q axis (i_d, i_q): for example, a FOC can be considered, usually tuned with a small inductance, to avoid instability.
Here, one approach could be to measure line to line voltages v_{abc} (or just two of them, according to three-phase system theory [4]) in steady state conditions, where, considering the working station, they are PWM voltages, and sinusoidal plus ripple currents. Then fluxes are computed starting from steady-state voltage equations (1.4), reported again for sack of clarity

$$\begin{cases} v_d = R_s \cdot i_d - \omega \cdot \lambda_q \\ v_q = R_s \cdot i_q + \omega \cdot \lambda_d \end{cases} \tag{2.3}$$

From which fluxes could be computed as:

$$\begin{cases} \lambda_d = \frac{v_q - R_s \cdot i_q}{\omega_e} \\ \lambda_q = -\frac{(v_d - R_s \cdot i_d)}{\omega_e} \end{cases} \tag{2.4}$$

However, this approach lead to some problems, related to the voltage themselves: the goal is to obtain voltages in dq frame, but only v_{abc} are measured, furthermore PWM signals, not the fundamental component.
For this reason, an approach involing a power analyzer is more recommended, since they usually directly pin to the voltage fundamental component when measuring powers, active and reactive. From AC circuit theory, is given that:

$$\begin{aligned} P &= V \cdot I \cdot \cos(\varphi) \\ Q &= V \cdot I \cdot \sin(\varphi) \end{aligned} \tag{2.5}$$

Moreover, equation (2.5) gives information about phase angle between current and voltage, as well as power factor $cos(\varphi)$. Since it holds in whatever reference frame, in dq frame (2.5) becomes:

$$\begin{cases} P = \frac{3}{2}(i_d \cdot v_d + i_q \cdot v_q) \\ Q = \frac{3}{2}(i_d \cdot v_q - i_q \cdot v_d) \end{cases} \tag{2.6}$$

Thus becomes a system with two equations and two unknowns, which solution is trivial.

Despite that, is to say that measurements include stator resistive voltage drops, according to eq.(2.3). Indeed, they can be considered negligible only at high speed: tests must be done at low constant speed, to avoid injected currents to produce iron losses and not contribute to produce fluxes.

Nevertheless, injected current pulses should last as long as the mechanical transient in estinguished: measurements are logged within one mechanical period and then averaged, to eliminate any signal component at electrical or mechanical periodicity, including motor space harmonics, inverter dead- time harmonics, and defects of mechanical nature such as misalignments and eccentricities [1].

On the other hand, stator resistive voltage drops are compensated taking two measurements for one current couple injected: it turns out that voltage drops are compensated if a first measurement taken as

$$\begin{cases} v_d = R_s \cdot i_d - \omega \cdot \lambda_q \\ v_q = R_s \cdot |i_q| + \omega \cdot \lambda_d \end{cases}$$

is followed by

$$\begin{cases} v_d = R_s \cdot i_d - \omega \cdot \lambda_q \\ v_q = -R_s \cdot |i_q| + \omega \cdot \lambda_d \end{cases}$$

so, keeping i_d constant and changing the sign on q axis current. At the end, a 3rd measurement is included and averaged with the 1st one, in order to compensate the heating stator resistance, while a 4th measurment follows in the case of a PM motor, in order to track magnet flux linkage variation over measurements, and check is the magnet is subjected to too high temperatures.

Flux linkages in dq reference frame are then computed as follows

$$\begin{cases} \lambda_d = \frac{1}{2} \cdot \left(\frac{v_{q,1}+v_{q,3}}{2} + v_{q,2} \right) \cdot \frac{1}{\omega_e} \\ \lambda_q = -\frac{1}{2} \cdot \left(\frac{v_{d,1}+v_{d,3}}{2} - v_{d,2} \right) \cdot \frac{1}{\omega_e} \end{cases} \tag{2.7}$$

Following figures represents a first look of flux maps extracted from magnetic model identification (MMI), related to an IPM motor.

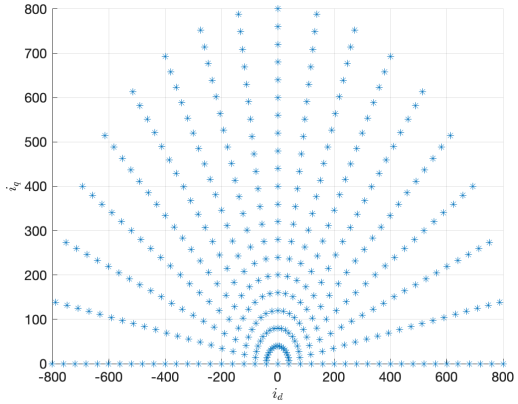

Figure 2.2: $\lambda_d(i_d, i_q)$, (current domain).

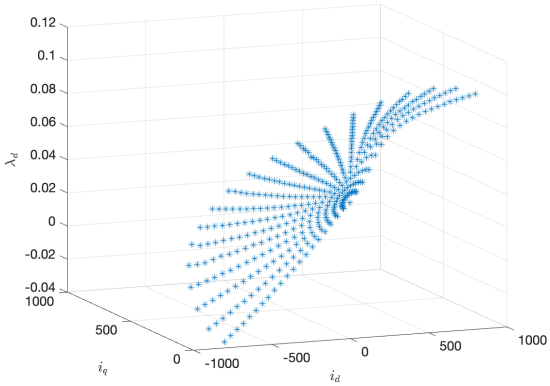

Figure 2.3: $\lambda_d(i_d, i_q)$ (full axis view).

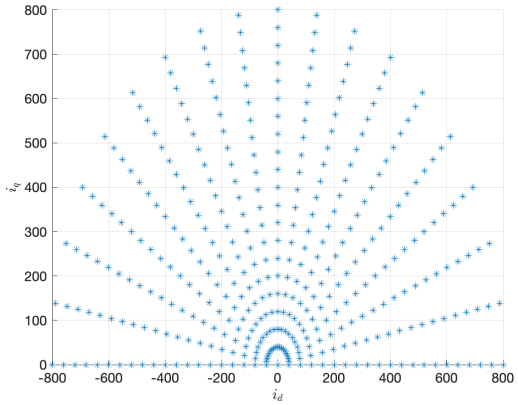

Figure 2.4: $\lambda_q(i_d, i_q)$, (current domain).

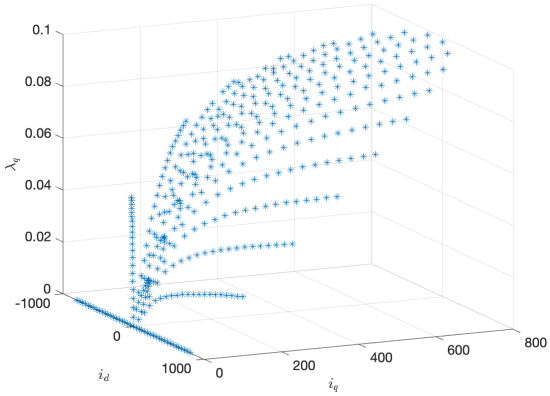

Figure 2.5: $\lambda_q(i_d, i_q)$ (full axis view).

2.2 Current and flux maps computation

Figures from (2.2) to (2.5) show that maps are built taken into account a currents polar domain.
Recall that this procedure holds for syncrhonous machines of all kinds, hence it can be applied in the case of a WFSM: the only difference is the number of identification measurements, since it must be done fixing the field current and repeating the procedure for each i_f value.
Then, obtained flux vectors are elaborated in a MATLAB environment, where, starting from *scatteredInterpolant* function, a current regular domain is used to interpolate flux vectors, to get a first look to flux maps.

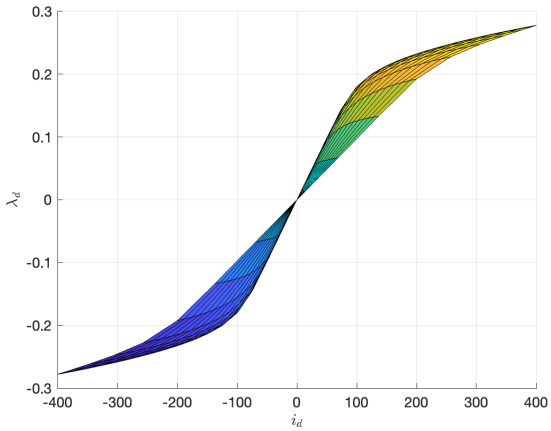

Figure 2.6: $\lambda_d(i_d, i_q, i_f = 0)$.

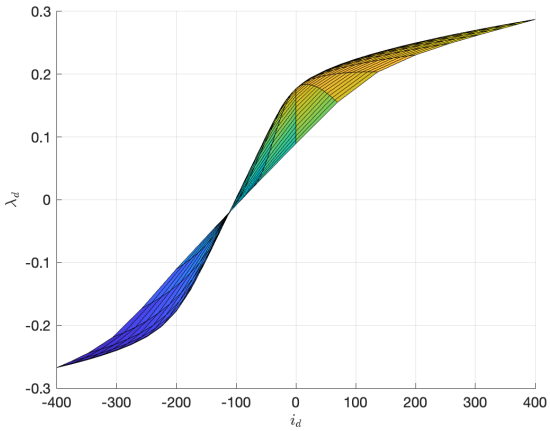

Figure 2.7: $\lambda_d(i_d, i_q, i_f = 6)$.

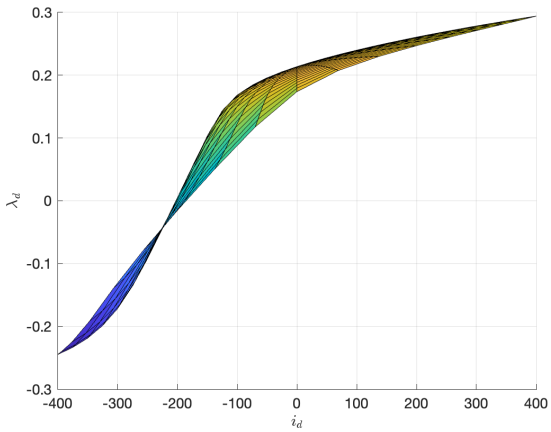

Figure 2.8: $\lambda_d(i_d, i_q, i_f = 9)$.

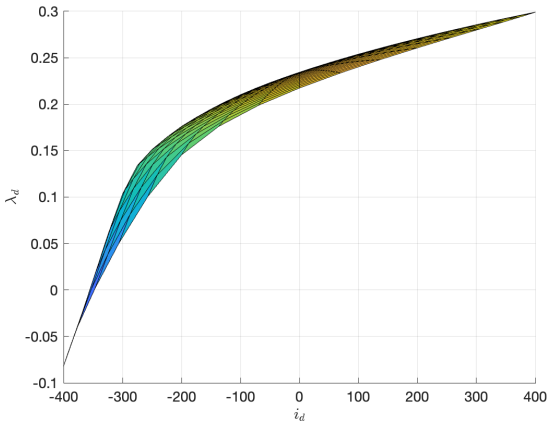

Figure 2.9: $\lambda_d(i_d, i_q, i_f = 14)$.

On the other hand, same crucial importance is given to current maps (also denoted as inverse maps), since, especially for control purposes, they give the possibility to interpolate flux values and get the corresponding current values. For sack of clarity, simulating the motor model generates fluxes from voltages, that needs to be interpolated to get associated currents in dq frame: this can be easily done with inverse maps, that, besides, can be computed offline, as in the case of this thesis work.
Again, for each field current value, a regular flux domain is established and used to interpolate corresponding current values, in the same way it's done for flux maps

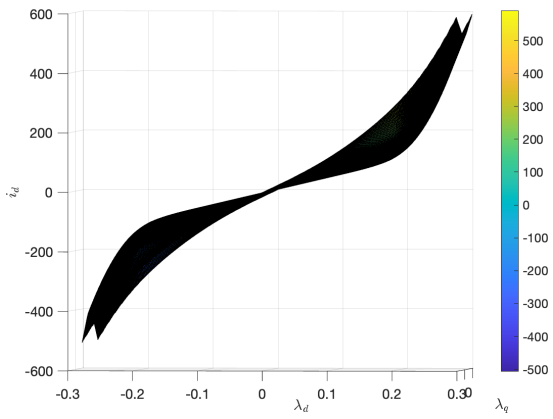

Figure 2.10: $i_d(\lambda_d, \lambda_q, i_f = 0)$.

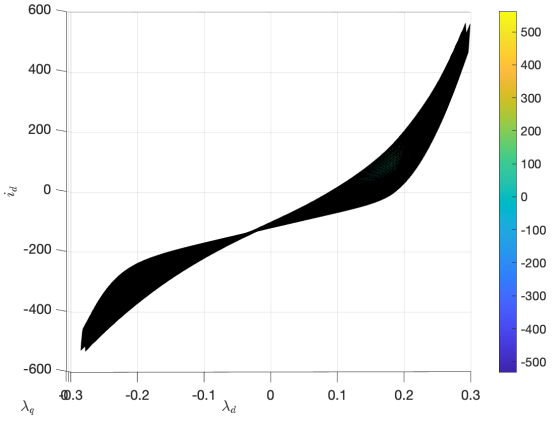

Figure 2.11: $i_d(\lambda_d, \lambda_q, i_f = 6)$.

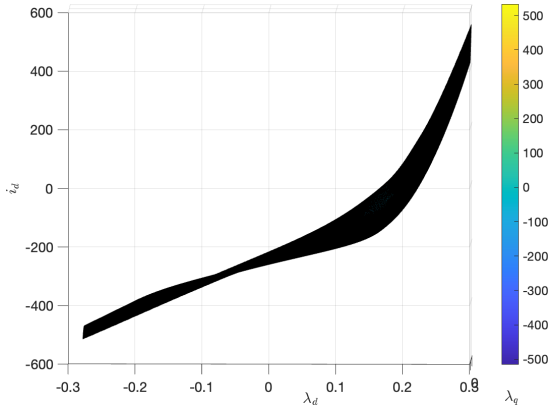

Figure 2.12: $i_d(\lambda_d, \lambda_q, i_f = 9)$.

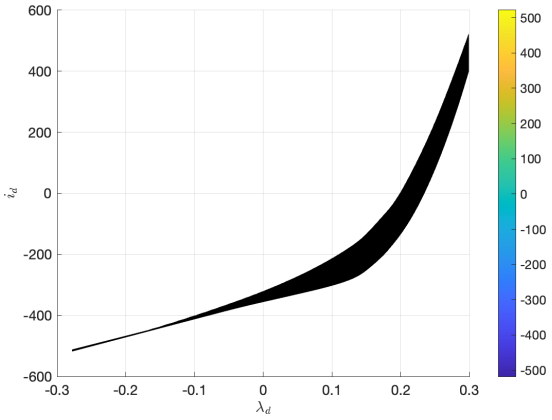

Figure 2.13: $i_d(\lambda_d, \lambda_q, i_f = 14)$.

As already mentioned, current maps are crucial for motor simulation, for example, in a *Simulink* environment, where motor and converters are simulated together, to get a first look to the final system to be controlled. Indeed, next chapter provides some converters theory simultaneously applied in a simulation environment where the whole system is tested.

Chapter 3

eDrive design and validation

3.1 Converters design and simulation

Figure (1.6) gives a first look to an EV drivetrain, from battery to electric motor. DC supplying battery pack feeds the motor with AC three-phase voltages, thanks to the power electronic between the battery pack itself, and the motor. Indeed, DC input voltage is converted in AC by a Voltage Source Inverter, crucial element for control purposes as well, since, as already mentioned in Chapter 2, reference quantities are turned into reference voltages for the power electronics.
However, in the case of WFSM, voltage regulation must be done for rotor field voltage as well, this time involving a DC to DC converter able to handle both positive and negative voltage levels, as the case of H-Bridge DCDC converer (also known as 4 quadrants DCDC converter).

Next sections provide a an overview of the two main converters employed in control simulation, with all their key aspects for traction applications. Then, thanks to the magnetic model exploited and identified Chapter 2, EV drivetrain is simulated to get a first validation of the whole system.

3.1.1 Voltage Source Three-Phase Inverter

Working principle of a Voltage Source Invertes is exploited starting from one of its simplest configurations: a single phase half bridge inverter, with a PWM based switching function, together with an averaged dynamic model, instead handled by duty cycles.

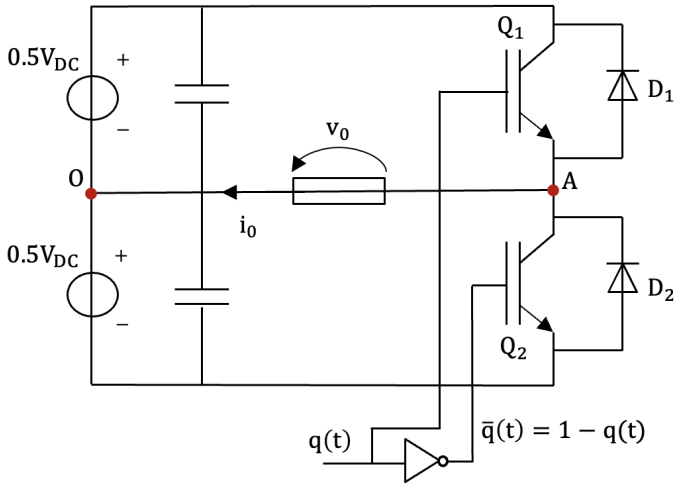

Figure 3.1: Single phase half bridge VSI.

Figure (3.1) represents one bidirectional switching cell with symmetrical DC voltage supply ($\pm 0.5 V_{DC}$), where the AC load is connected between cell output (A) and central supply point (O). With the assumption of an ideal switching cell, output depends only on input voltage and switching function $q(t)$

$$\begin{aligned} q = 1 \Rightarrow v_o &= +\frac{V_{DC}}{2} \\ q = 0 \Rightarrow v_o &= -\frac{V_{DC}}{2} \end{aligned} \tag{3.1}$$

then

$$v_o(t) = [2 \cdot q(t) - 1] \cdot \frac{V_{dc}}{2} \tag{3.2}$$

If the switching function is generate by a PWM block with unpolar carrier at frequency $f_s = \frac{1}{T_s}$, the switching function is generated comparing a command signal and a carrier, as shown in fig (3.2)

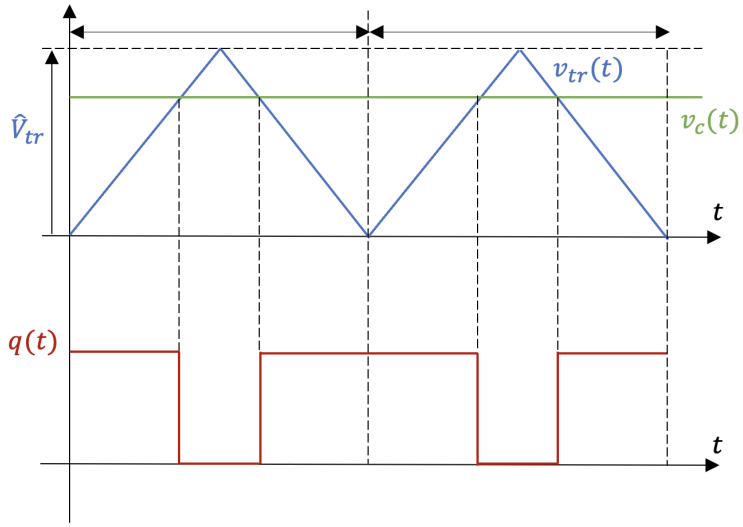

Figure 3.2: PWM modulation example.

Since VSI must generate a sinusoidal mobile mean value output

$$\bar{v}_o^* = \hat{V}^* \cdot \sin(\omega t) \tag{3.3}$$

and output mobile mean voltage is

$$\begin{aligned} \bar{v}_o = \frac{1}{T_s}\int_0^{T_s} v_o(t)\,dt = \frac{V_{dc}}{2T_s}\cdot\int_0^{T_s}[2\cdot q(t)-1]\,dt \\ \Rightarrow \bar{v}_o = V_{dc}\cdot\left[\frac{v_c(t)}{\hat{V}_{tr}} - 0.5\right] \end{aligned} \tag{3.4}$$

Simplification obtained considering that duty cycle definition stands that

$$\frac{1}{T_s}\int_0^{T_s} q(\tau)\,d\tau = d(t) = \frac{v_c(t)}{\hat{V}_{tr}} \tag{3.5}$$

then, according to (3.3), it becomes

$$\bar{v}_o = V_{dc}\cdot\left[\frac{v_c(t)}{\hat{V}_{tr}} - 0.5\right] \tag{3.6}$$

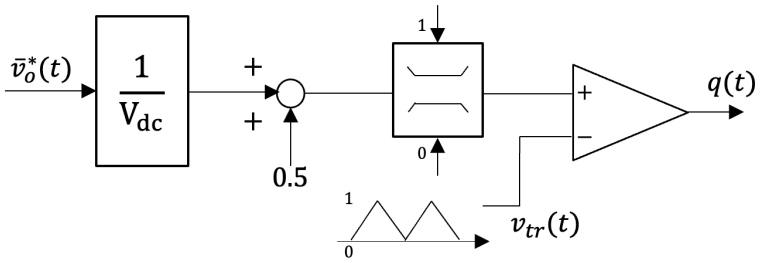

Figure 3.3: Switching function generation.

and the command must be sinusoidal

$$v_c(t) = \left[\frac{\hat{V}^*}{V_{dc}} \cdot \sin \omega t + 0.5\right] \cdot \hat{V}_{tr} \tag{3.7}$$

Where the offset of 0.5 results from unipolar PWM modulation, and $\omega = 2\pi f_0$ (Hz) is the desired outpout frequency.
Nevertheless, inverter analysis can be performed considering a PWM modulation technique based on a unitary peak value carrier $v_{tr}(t)$, as the case of the inverter that will be simulated. This way the PWM command $v_c(t)$ coincides with duty cycle, and command generation is exploited in fig 3.3.

The mobile mean value of the voltage output generated by an half bridge single-phase inverter is limited by $V_{dc}/2$ (3.1): this value reaches V_{dc} in a full bridge configuration, but remains stuck at most to $V_{dc}/\sqrt{3}$ in a three-phase inverter with zero sequence injection, always under the assumption of a sinusoidal linear modulation, valid when

$$m_a = \frac{\hat{V}^*}{0.5 \cdot V_{dc}} \Rightarrow m_a \leq 1 \tag{3.8}$$

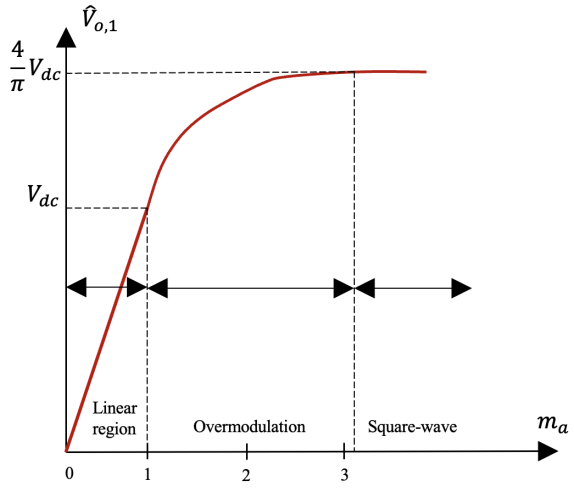

Figure 3.4: Modulation regions.

Now the focus will be on the configuration employed in traction applications, i.e. a three-phase inverter, made up with three bidirectional switching cells, fed by a single DC voltage supply [4].

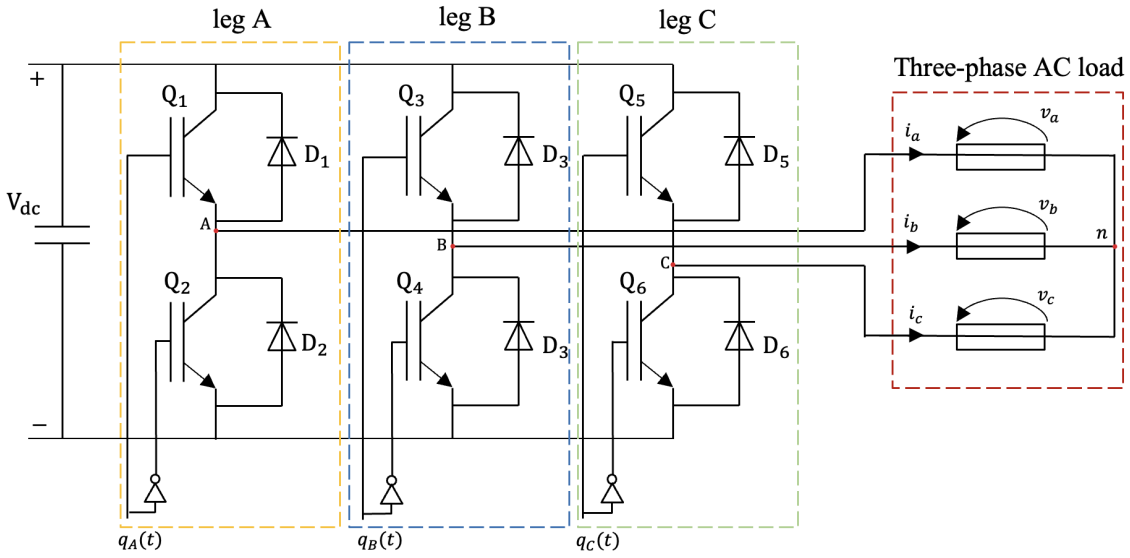

Figure 3.5: Three-phase VSI.

A virtual DC link midpoint O is considered (same as reported in Fig.3.1), as well as a PWM modulation technique with unitary carrier amplitude.

Again, with the hypothesis of ideal switching cell, instantaneous output voltages are function of input and switching function

$$\begin{aligned} v_{AO}(t) &= [2q_A(t) - 1] \cdot \frac{V_{DC}}{2} \\ v_{BO}(t) &= [2q_B(t) - 1] \cdot \frac{V_{DC}}{2} \\ v_{CO}(t) &= [2q_C(t) - 1] \cdot \frac{V_{DC}}{2} \end{aligned} \tag{3.9}$$

This equation turns out to be the same used for an single phase half bridge VSI. The inverter imposes a symetrical three-phase voltage system (in terms of mobile mean values) with respect to the DC link midpoint O. As already mentioned, commands must be sinusoidal, in this case represented by

$$\begin{cases} v_{cA}(t) = d_A(t) = \frac{\hat{V}^*}{V_{dc}} \cdot \sin(\omega t) + 0.5 \\ v_{cB}(t) = d_B(t) = \frac{\hat{V}^*}{V_{dc}} \cdot \sin(\omega t - \frac{2\pi}{3}) + 0.5 \\ v_{cC}(t) = d_C(t) = \frac{\hat{V}^*}{V_{dc}} \cdot \sin(\omega t + \frac{2\pi}{3}) + 0.5 \end{cases} \tag{3.10}$$

since desired output mobile mean voltages are

$$\begin{cases} \bar{v}_{AO}(t) = \hat{V}^* \cdot \sin(\omega t) \\ \bar{v}_{BO}(t) = \hat{V}^* \cdot \sin(\omega t - \frac{2\pi}{3}) \\ \bar{v}_{CO}(t) = \hat{V}^* \cdot \sin(\omega t + \frac{2\pi}{3}) \end{cases} \tag{3.11}$$

Assuming a balanced active three-phase load, the common mode voltage (at point n) is obtained as

$$v_{nO}(t) = \frac{1}{3} \cdot (v_{AO} + v_{BO} + v_{CO}) \tag{3.12}$$

Furthermore, instantaneous voltages of a connected three-phase load (e.g. electric motor) are given by the difference between instantaneous inverter output voltages and common mode voltages

$$\begin{aligned} v_a(t) &= v_{AO}(t) - v_{nO}(t) = \frac{2}{3} \cdot v_{AO}(t) - \frac{1}{3} \cdot [v_{BO}(t) + v_{CO}(t)] \\ v_b(t) &= v_{BO}(t) - v_{nO}(t) = \frac{2}{3} \cdot v_{BO}(t) - \frac{1}{3} \cdot [v_{AO}(t) + v_{CO}(t)] \\ v_c(t) &= v_{CO}(t) - v_{nO}(t) = \frac{2}{3} \cdot v_{CO}(t) - \frac{1}{3} \cdot [v_{AO}(t) + v_{BO}(t)] \end{aligned} \tag{3.13}$$

Least but not last, average dynamic model allows to represent output mobile mean voltages as function of duty cycles:

$$\begin{aligned} \bar{v}_a(t) &= \frac{V_{DC}}{\sqrt{3}} \cdot (2 \cdot d_A(t) - d_B(t) - d_C(t)) \\ \bar{v}_b(t) &= \frac{V_{DC}}{\sqrt{3}} \cdot (2 \cdot d_B(t) - d_A(t) - d_C(t)) \\ \bar{v}_c(t) &= \frac{V_{DC}}{\sqrt{3}} \cdot (2 \cdot d_C(t) - d_A(t) - d_B(t)) \end{aligned} \tag{3.14}$$

Zero Sequence Injection Modulation Technique

The phase fundamental voltage for a three-phase inverter supplying a star-connected load is the same as for the single phase half-bridge inverter, with the same modulation regions exploited in Fig. (3.4). Since motor control approaches prefer inverter linearity region operations, a solution to extend inverter linearity range is found in PWM with *zero-sequence injection*.
This modulation technique acts within PWM command generation, adding a third armonic in the mobile mean value of the common mode voltage (Fig.3.6). Common mode component, with the hypothesis of modulation index $m_a = 1$ is computed as

$$v_{CM}(t) = -\frac{1}{2} \cdot [\max(v^*_{a,norm}, v^*_{b,norm}, v^*_{c,norm}) + \min(v^*_{a,norm}, v^*_{b,norm}, v^*_{c,norm})] \tag{3.15}$$

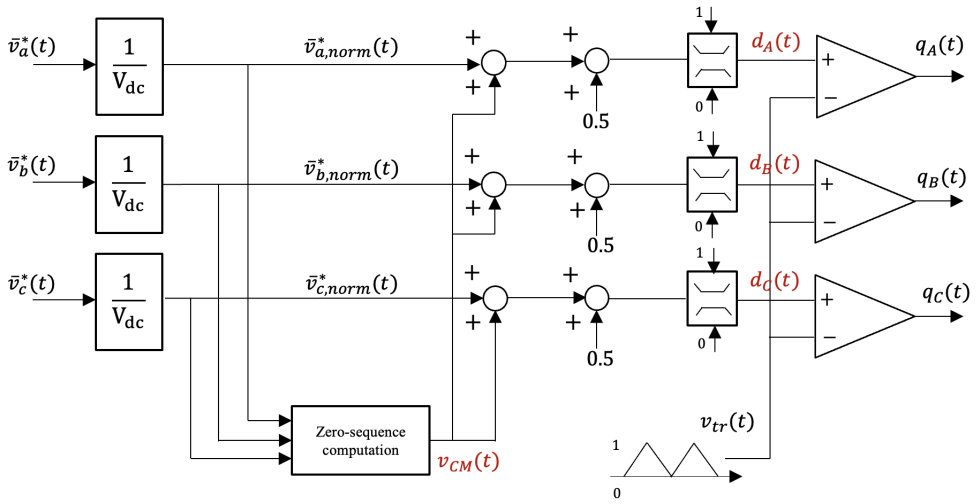

Figure 3.6: Command generation with ZSI.

Since duty cycles now saturate at

$$\hat{V}^* = 1.15 \cdot \frac{V_{DC}}{2} \tag{3.16}$$

Iinverter linear region turns out to be extended by 15.4%.

Graphic results and differences between techniques with and without ZSI are reported in section 3.2, where all of the proposed power electronics design solutions are exploited and simulated in a *Simulink* environment.

3.1.2 H-bridge DC-DC converter

As already mentioned, rotor quantities must be regulated too, and field voltage is regulated with a solution that allows to geerate both positive and negative voltage levels at the output. The DC to DC converter considered in this work is thus an H-bridge DCDC converter, also known as 4 quadrants converter, for obvious reasons.

As it is represented in Fig.3.7, it is built on two switching cells connected to the same input V_{DC}, while load is connected between the two respective cell outputs A and B.

With the hypothesis of a PWM modulation, one command $v_c(t)$ and the same triangular carrier reported in 3.2, if command signal is such that

$$-\hat{V}_{tr} \leq v_c(t) \leq \hat{V}_{tr} \tag{3.17}$$

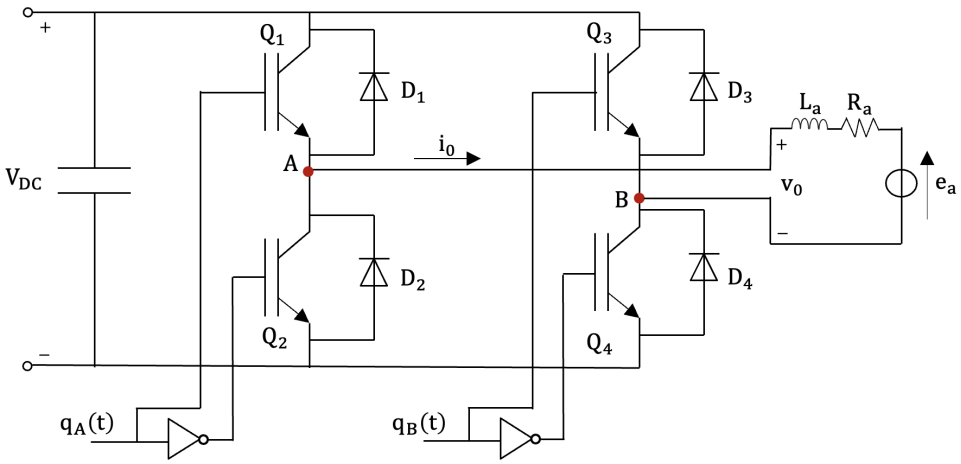

Figure 3.7: H-Bridge DCDC converter.

and duty cyles are computed as

$$\begin{aligned} d_A(t) &= 0.5 + \frac{1}{2\hat{V}_{tr}} \cdot v_c(t) \\ d_B(t) &= 0.5 - \frac{1}{2\hat{V}_{tr}} \cdot v_c(t) \end{aligned} \tag{3.18}$$

Output mean voltages between nodes AN and BN:

$$\begin{aligned} \bar{v}_{AN}(t) &= 0.5 \cdot V_{in} + \frac{V_{in}}{2\hat{V}_{tr}} \cdot v_c(t) \\ \bar{v}_{BN}(t) &= 0.5 \cdot V_{in} - \frac{V_{in}}{2\hat{V}_{tr}} \cdot v_c(t) \end{aligned} \tag{3.19}$$

where

$$0 \leq \bar{v}_{kN}(t) \leq V_{in}$$

Then output mean voltage is obtained from difference between equations (3.19), as

$$\bar{v}_o(t) = \bar{v}_{AN}(t) - \bar{v}_{BN}(t) = \frac{V_{in}}{\hat{V}_{tr}} \cdot v_c(t) = k_{PWM} \cdot v_c(t) \tag{3.20}$$

Notice that k_{PWM} is constant, and command $v_c(t)$ behaves like (3.17), then it's true that

$$-V_{in} \leq \bar{v}_o(t) \leq V_{in} \tag{3.21}$$

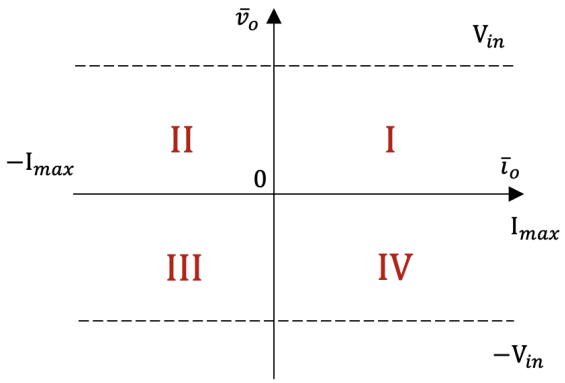

Figure 3.8: H-Bridge converter working areas

In practice is applied the same trick as VSI case: a carrier with unitary peak value is considered, then command coincides with duty cycle (now limited between 1 and -1).
At the end, this solution allows to obtain bidirectional current flowing (same as a bidirectional switching cell, made with a buck+boost combination) plus two levels output voltage. In Fig.3.8 are summarised the H-Bridge working areas.

3.2 EV drivetrain simulation

All of the notions and equations written in previous section turns out to be crucial for design and control purposes. Before to get into control field, the whole system provided by converters and motor has been designed and simulated in *Simulink*.

Starting from this capter's topic, converters are modelled exactly following equations in section 3.1, while giving as system input a set of three-phase reference voltages (plus a constant voltage for H-Bridge converter), all the possible cases are tested, as well as a band-pass filter implementation in order to compare reference voltages with the fundamental component of PWM voltage as inverter output.
A first simulation is made without applying ZSI modulation technique, and the following reference quantities are taken into account:

switching frequency	f_s	2 [kHz]
ref signal frequency	f^*	50 [Hz]
DC-link voltage	V_{DC}	350 [V]
modulation index	m_a	1
reference voltage amplitude	$\hat{V}^*$	175 [V]

Table 3.1: 1st simulation reference values.

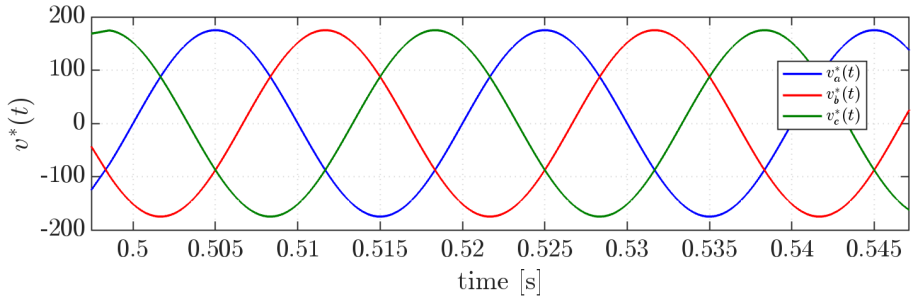

Figure 3.9: reference voltages.

Note that reference voltage ampitude is just 175V, with respect to V_{DC} that reaches 350V, due to theory regarding section 3.1.1. Thus, reference voltages are reported in Fig.3.9.
From reference voltages, duty cycle is computed following block scheme 3.3. Since m_a is equal to 1, they are well defined between 0 and 1.

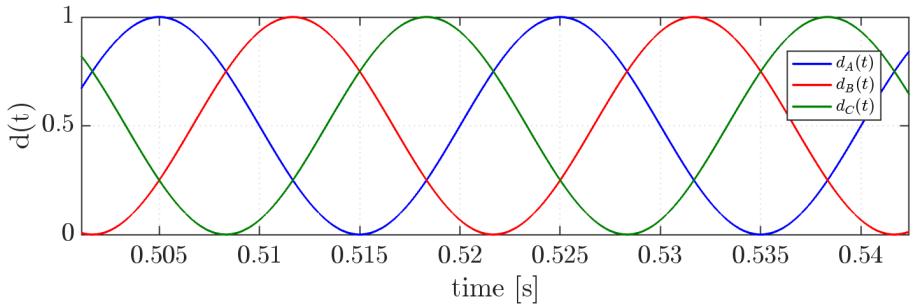

Figure 3.10: duty cycles.

This configuration leads to voltages generated with respecto to DC link midpoint O exploited in Fig.3.12. They represent bipolar voltage pulses with amplitude $\pm V_{DC}/2$, while mobile mean values sre phase shifted by 120 electrical degrees with respect to the fundamental frequency.
Furthermore, AC load phase voltages, with respect to neutral point n, are voltage pulses with values $\pm 2/3V_{DC}, \pm 1/3V_{DC}, 0$ (Fig.3.11), and fundamental voltages are close to their mobile mean value, with the hypothesis of linear PWM (modulating in linear region exploited in Fig.3.4), i.e.

$$v_{a,1}(t) \simeq \bar{v}_a(t)$$

Indeed, useful voltage for power conversion begins to the fundamental component $v_{0,1}(t)$, while voltage distorsion includes all the remaining harmonics $v_h(t)$ generated by switching activity, with the frequency

$$f_h = k_1 \cdot f_s \pm k_2 \cdot f_0$$

Harmonics are grouped in sidebands around switching frequency and multiples.
On the other hand, load inductance is able to filter the load current, that turns out to be sinusoidal plus a current ripple, generated by switching operations, that depends on duty cycle (maximum value when $d = 0.5$).

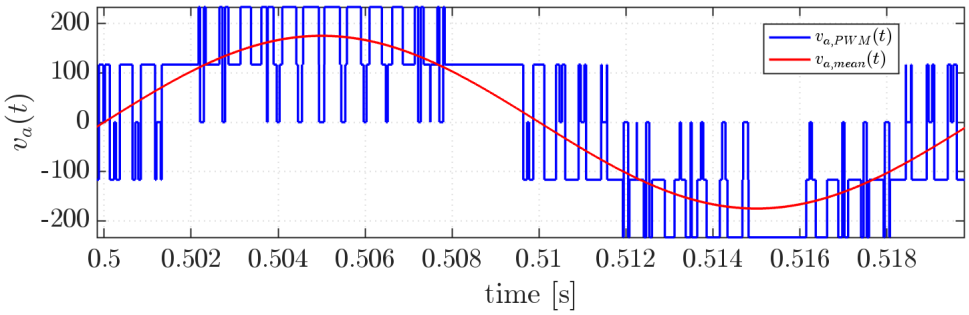

Figure 3.11: AC load instantaneous and mobile mean voltage.

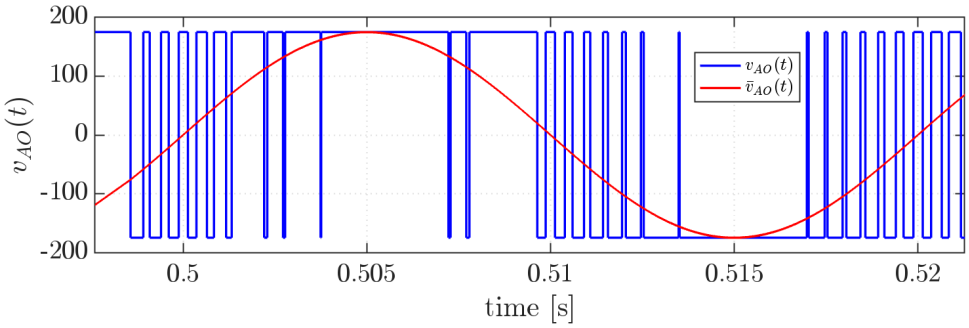

Figure 3.12: voltage pulses with respect to DC link midpoint O.

If the modulation index is incresed to values greater than 1, that means reference voltage amplitude

$$\hat{\mathrm{V}}^* > \frac{\mathrm{V_{DC}}}{2}$$

Simulations is performed incresing modulation index to

$$\mathrm{m_a} = 1.25$$

and leaving all the previous parameters constant.
Within overmodulation region (since $\mathrm{m_a} > 1$, duty cycle starts to become a trapezoidal waveform, clamped at 0 and 1: during saturation transients, cell does not switch, and, moreover, instantaneous output voltage starts to experience low order odd harmonics (undesired due to torque ripple), while output currents are distorted since load inductance cannot filter anymore.

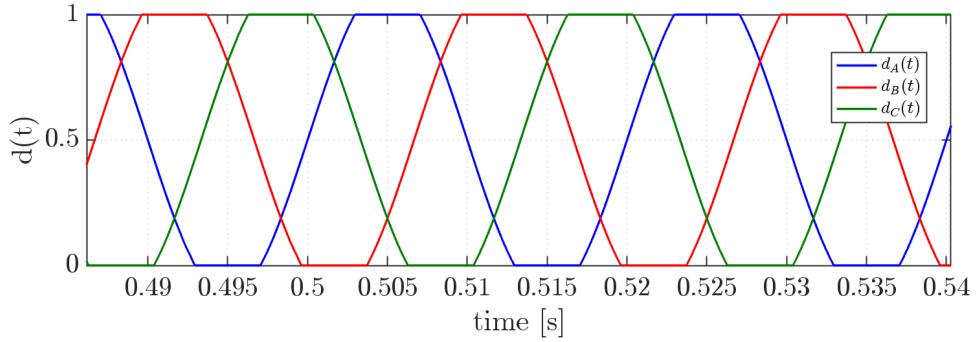

Figure 3.13: Duty cycles during overmodulation with $m_a = 1.25$.

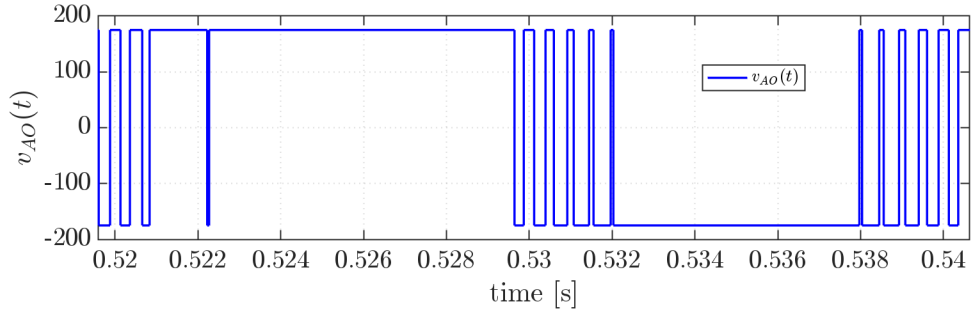

Figure 3.14: voltage pulses with respect to DC link midpoint O.

As already mentioned, ZSI is taken into account in order to extend inverter linear operation range. A third harmonic is added to the common mode voltage in order to extend PWM linear range.

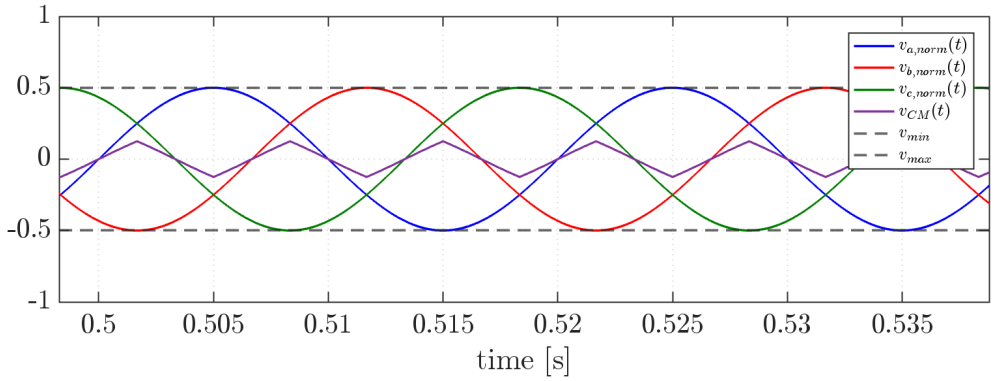

Figure 3.15: Common mode voltage and references, with $m_a = 1$.

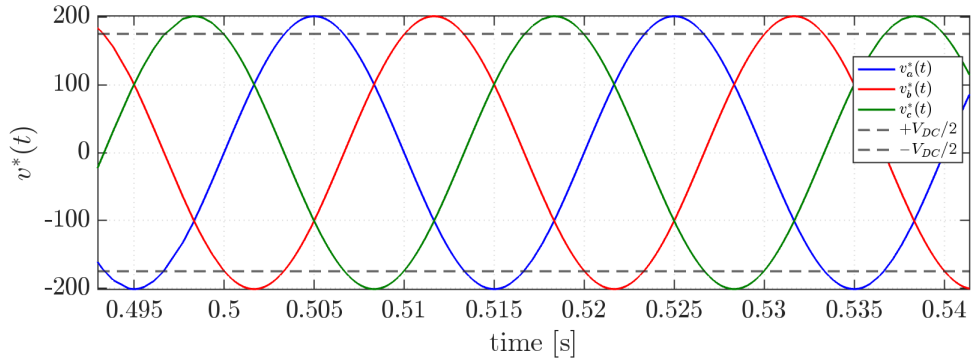

Figure 3.16: v^*_{abc} with ZSI and $m_a = 1.15$.

Extending linear region by 15.4% allows to increase modulation index until $m_a = 1.15$ without entering overmodulation region, thus exploiting a maximum output voltage amplitude

$$\hat{V}^* = \frac{V_{DC}}{\sqrt{3}}$$

This happens since duty cycle does not saturate. Moreover, zero sequence injection does not have any influence on phase voltages of the load.

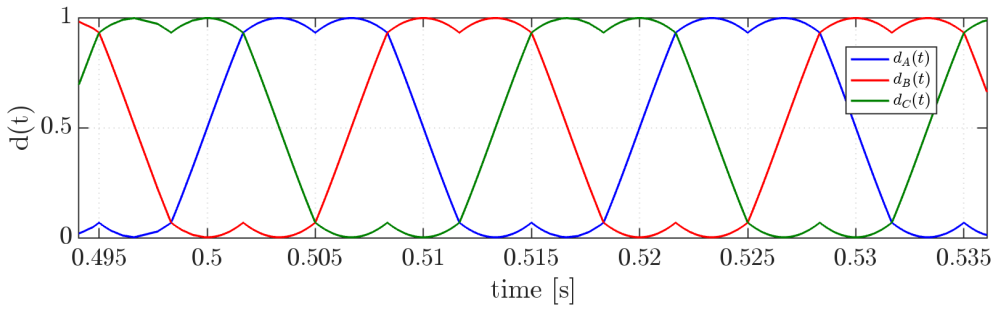

Figure 3.17: Duty cycles with ZSI and $m_a = 1.15$.

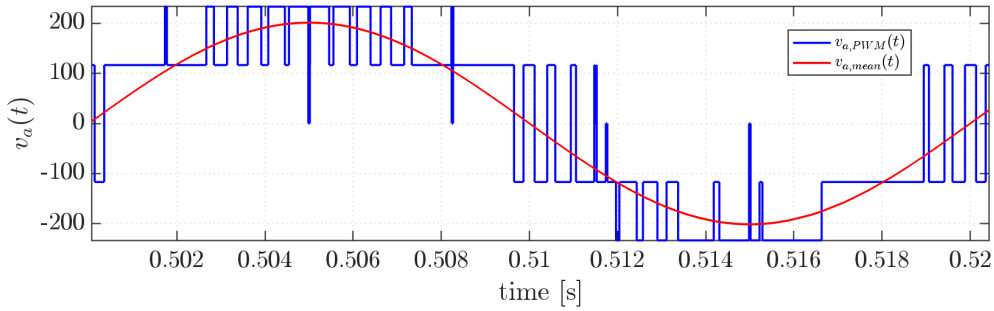

Figure 3.18: AC load instantaneous and mobile mean voltage with ZSI and $m_a = 1.15$.

At the end, simulation is validated comparing reference voltage, with instantaneous output voltage (to the motor), once it passes through a band pass filter, to extract its fundamental component.

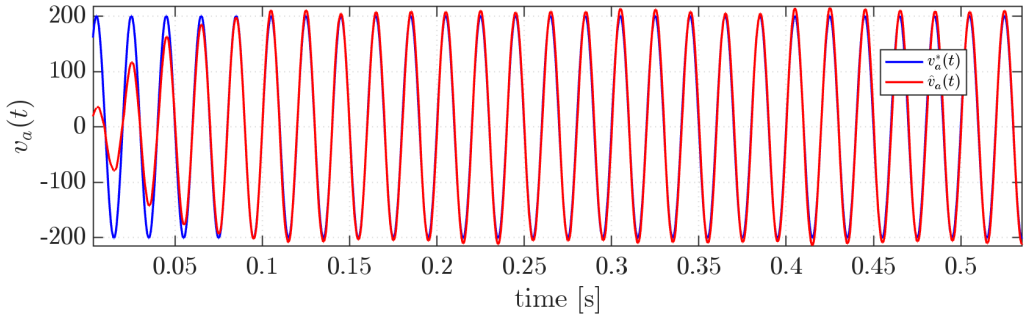

Figure 3.19: Reference voltage and filtered output voltage.

Applying zero sequence injection, obtained output voltage are now the input of a motor block, once reference voltages are now computed fixing reference currents and letting they generate reference voltages through simple PI regulators. However, a first flux control is implemented, since reference currents generate reference fluxes from flux maps (Chapter 2).
Thus, motor block (exploited in Fig.3.21) receives inverter and DCDC converter voltages, and must be able to give output currents and fluxes (they are then feed-backed to PI regulators block).

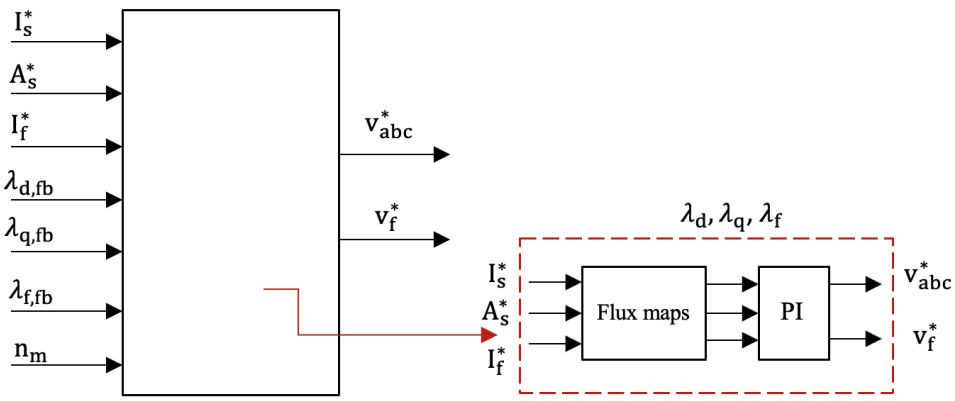

Figure 3.20: From reference current to reference inverter voltages.

Reference voltages feed the motor through steps explained in section 3.1, while motor block outputs machine fluxes and currents. Output currents are then compared with input reference, and results are reported in Fig.3.22. What is expected is the same input waveform reported to output, apart from the current ripple.

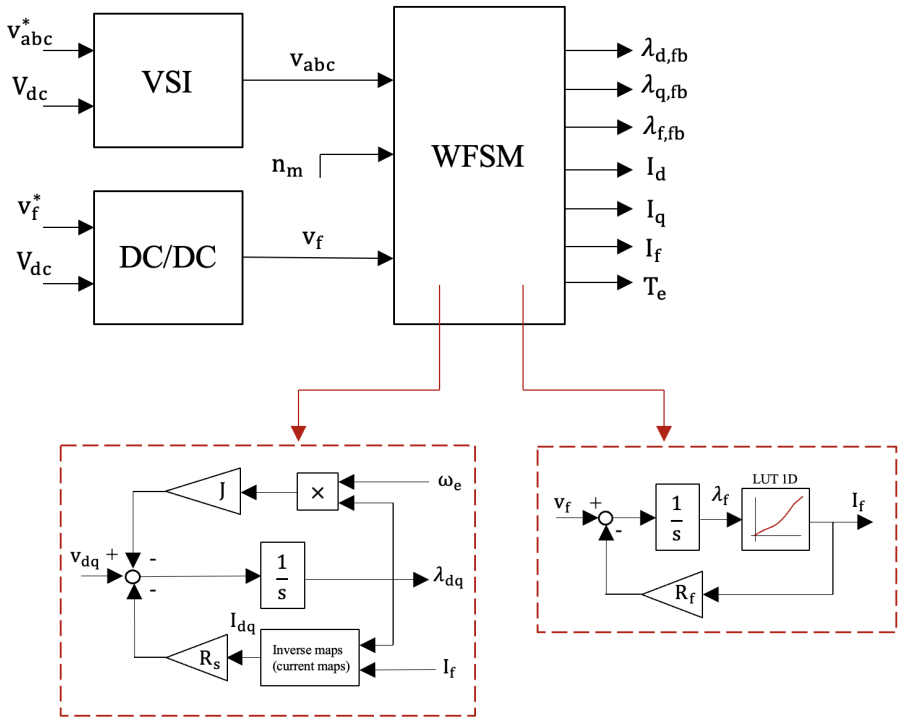

Figure 3.21: Motor block scheme.

Figure 3.21 shows that motor block scheme is represented by magnetic model exploited in Chapter 2, both for stator and rotor quantities.

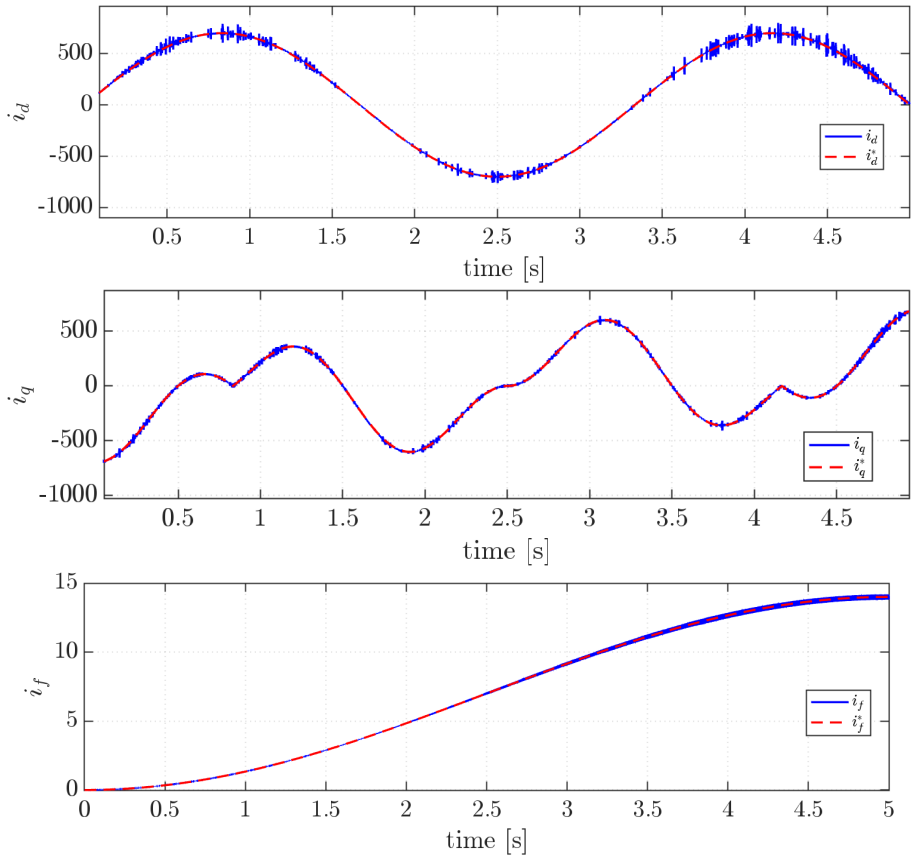

Figure 3.22: $(i_d, i_d^*), (i_q, i_q^*), (i_f, i_f^*)$.

Chapter 4

Control maps

4.1 Background

Chapter 1 shows that Flux Polar Control is implemented apart from a LUT able to perform linear torque regulation, the one related to load angle δ (see block scheme in Fig.4.1)(a).

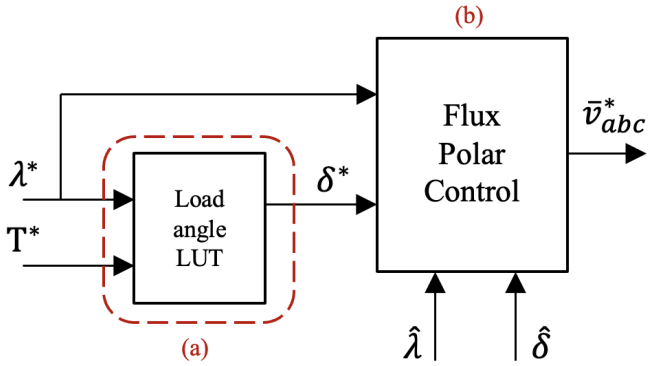

Figure 4.1: FPC scheme.

Load angle LUT computation is crucial for control purposes, since it must include all the machine limitations, as well as the ability to generate reference within MTPA, MTPV and MEPT profile.

peak stator current	I_{max}	400 [A]
peak rotor current	$I_{f,max}$	14 [A]
peak torque	$T_{e,max}$	265 [Nm]
peak speed	$n_{m,max}$	1200 [rpm]
peak power	$P_{e,max}$	100 [kW]
DC-link voltage	V_{DC}	350 [V]

Table 4.1: Renault ZOE specifications.

All the maps needed to perform FPC must lie within limits provided by table 4.1, to guarantee motor operating conditions of maximum efficiency.
Let's say the torque range for Renault ZOE WFSM is

$$\mathrm{T_e} \in [0, \mathrm{T_{e,max}}] \tag{4.1}$$

Each of the iso-torques produced by the motor can be established with a wide set of currents (i_d, i_q, i_f), thus the challenge is to find a set of minimum currents able to make that certain torque affordable. Same approach is applied with fluxes, thus defining a maximum torque per-ampere (MTPA) and maximum torque per-volt (MTPV) profiles.
All of the next figures and results are obtained within a MATLAB environment, starting just from flux and current maps exploited in Chapter 2.

4.2 Constrained profiles

The trajectory in dq plane corresponding to the maximum torque for a given current amplitude is defined as MTPA, maximum torque per-Ampere, usually close to the maximum efficiency locus. On the other hand, maximum torque for a given magnetic flux amplitude (MTPV, maximum torque per volt) turns out to assume a crucial importance as well.
Through Matlab, in the specific case of a WFSM, all the iso-torque electrical parameters can be extracted directly from maps: the procedure is trivial and is reported in the appendix (A.2). Iso-torque electrical quantities are extracted for each torque level (in the range (4.1)) and for each value of the field current, that is

$$\mathrm{I_f} \in [0, \mathrm{I_{f,max}}]$$

Figure 4.2 from (a) to (b) shows MTPA and MTPV profile in dq plane, including all the torque levels. Note that, as already mentioned in Chapter 1, this WFSM behaves like a SyR motor for low field current (then, MTPA profile holds in the 1^{st} quadrant), while for high fiel currents behaves like an IPM, since MTPA profile slides into 2^{nd} quadrant. Moreover, all the computations are made following (4.1), since, for negative torque levels the behaviour is the same, except for a minus sign.

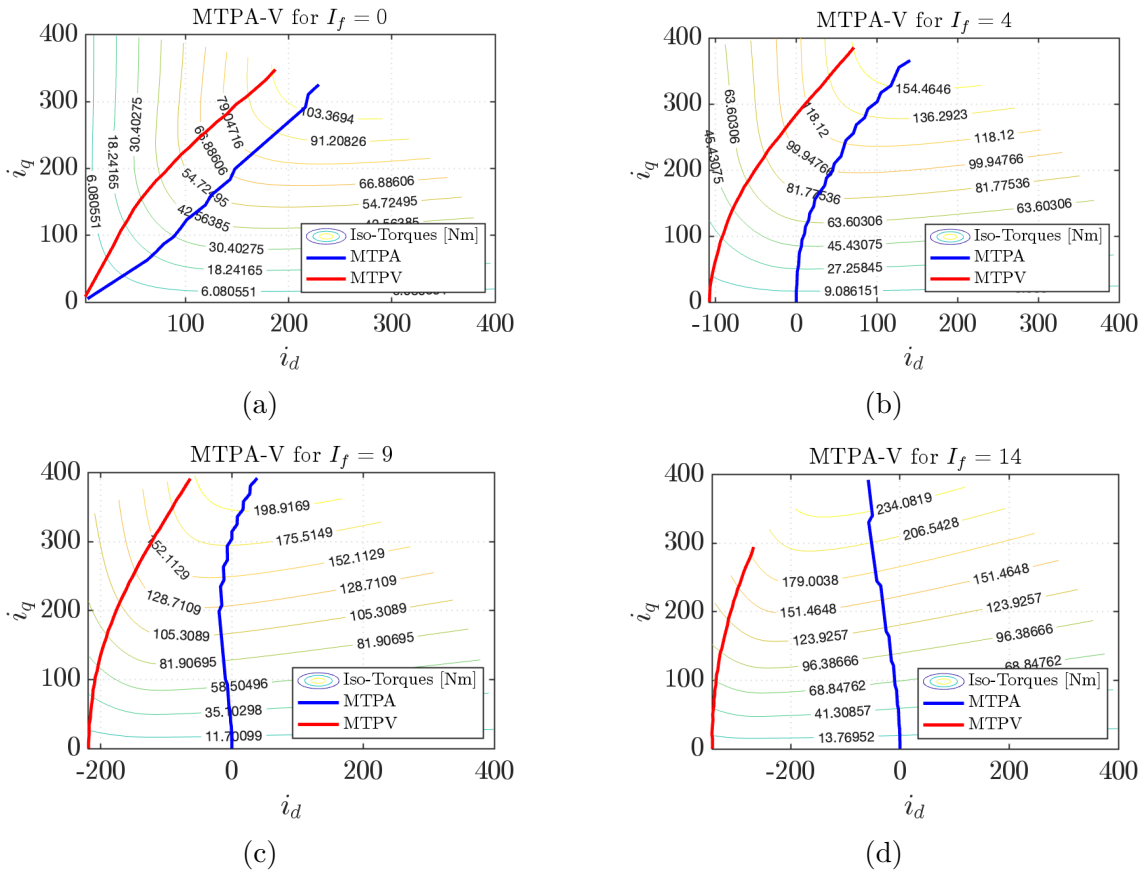

Figure 4.2: MTPA and MTPV profile for different field current values.

Load angle LUT is obtained from flux and torque maps, but they must include MTPA, MTPV and current limitation (I_{max}), so here the first challenge is to build constrained maps, that lie between MTPA and MTPV limitation, represented by the curves of Fig.4.2.

Some other data elaboration must be done, iso-values are again extracted for each torque levels and each field current: the following condition is applied and results are reported in Fig.4.4, for two field current levels, for sack of simplicity.

$$\begin{aligned} i_{d,iso} &\leq i_{d,MTPA} \\ i_{d,iso} &\geq i_{d,MTPV} \\ I_{s,iso} &< I_{max} \end{aligned} \tag{4.2}$$

Constraints in (4.2) are applied to all the electrical quantities of interest, thus to load angle map as well.

Trying to scan Fig.4.4 for both (a) and (b), turns out that, including all the machine and efficiency limitations, for each i_f there is a maximum torque affordable (lower or equal to $T_{e,max}$): these torque limits are crucial and and more details are provided in section 4.4.

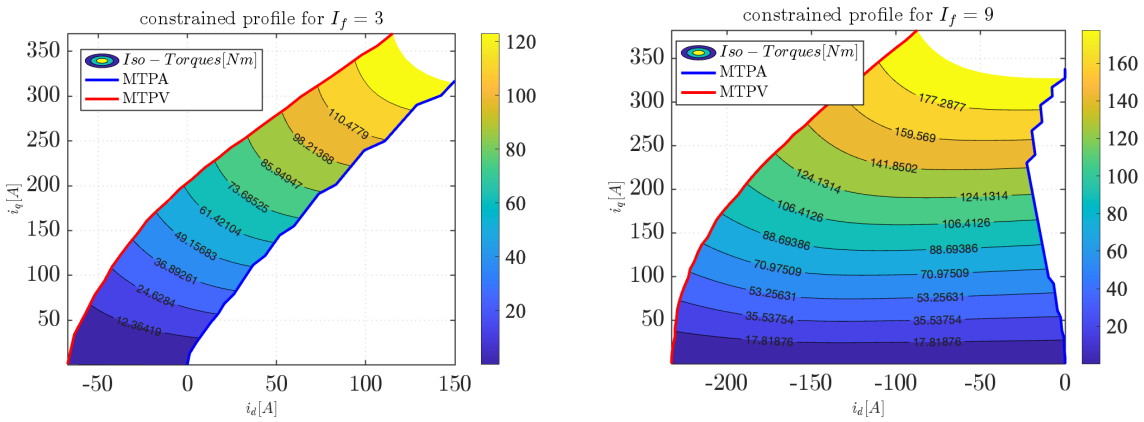

(a) (b)

Figure 4.3: Constrained torque profile for different field current values.

4.3 Load angle LUT

Once torque and flux maps, with their limitation, are exploited, it is possible to report it into load angle map as function of torque and stator flux amplitude, since it is defined as

$$\delta = \text{atan2}(\lambda_q, \lambda_d) \stackrel{\text{def}}{=} \text{atan}\left(\frac{\lambda_q}{\lambda_d}\right) \tag{4.3}$$

$$\lambda = \text{hypot}(\lambda_d, \lambda_q)$$

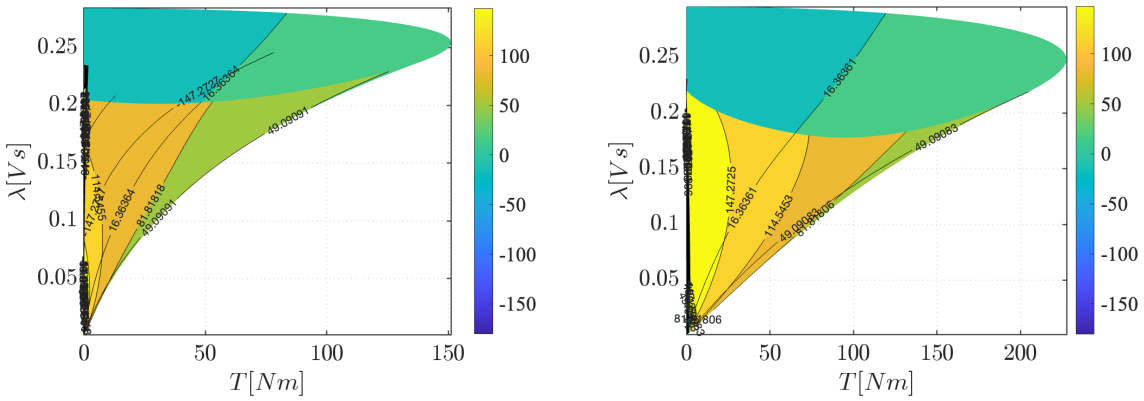

(a) (b)

Figure 4.4: $\delta(\lambda, \mathrm{T})$

Torque regulation by means of load angle δ is set to include all the limitations (4.1), then, all operating points of a given torque level are sorted to get increasing value of the stator flux amplitude [2].

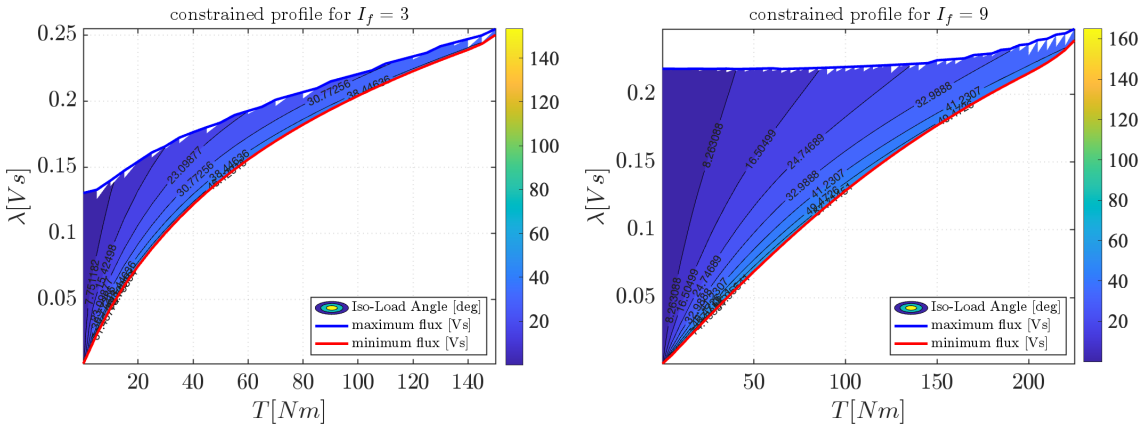

(a) (b)

Figure 4.5: constrained profile $\delta(\lambda, \mathrm{T})$.

MTPA and MTPV limits (where CL profile turns to be merged with MTPV, to represent just one prifle) respectively denote, for each torque level and each field current, maximum and minimum values that stator flux amplitude can assume to obtain that torque level.
Nevertheless, Fig.(4.5) shows an irregular profile, not the best to be interpolated within SM dynamics. The key is to exploit stator flux amplitude, for a given torque level, in *per-unit* values λ_{pu}: flux amplitude domain is now a regular one limited between 0 pu and 1 pu (Fig.4.7 (a) and (b)), where these limits represent minimum and maximum profile for each torque level and each field current.

According to the absolute torque reference torque T^* (more details on Chapter 5, Fig.), maximum and minimum flux are extracted (trivial, their profiles are intrinsically inside MTPA and MTPV+CL profile) as λ_{high} and λ_{low}. In the case of a WFSM, this procedure has to be repeated for each field current as well. Then, starting from reference stator flux amplitude λ^* (4.10), its corrisponding value in *pu* is computed as

$$\lambda^*_{\mathrm{pu}} = \frac{\lambda^* - \lambda_{\mathrm{low}}}{\lambda_{\mathrm{high}} - \lambda_{\mathrm{low}}} \tag{4.4}$$

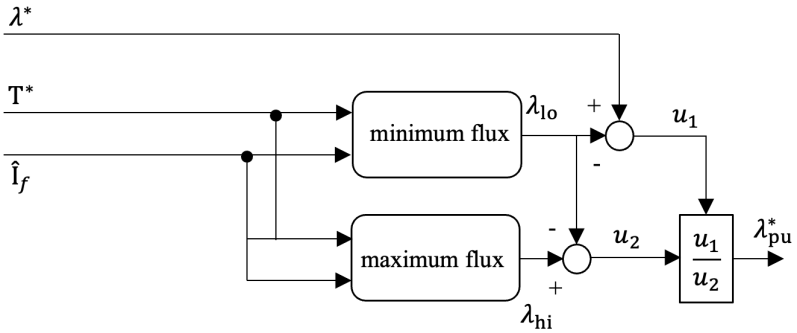

Figure 4.6: reference stator flux amplitude computation (per-unit).

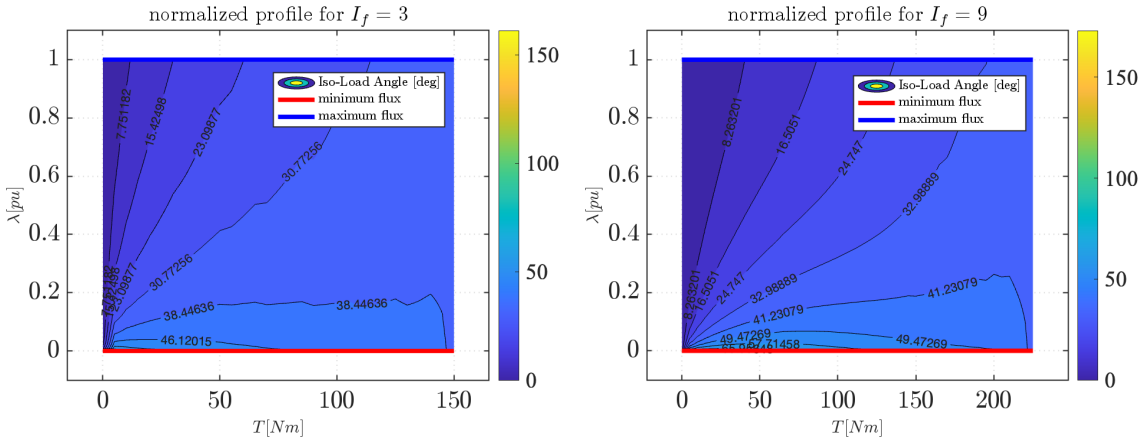

(a) (b)

Figure 4.7: Load angle map [pu], function of torque levels and stator flux amplitude.

4.4 Complementary maps

Flux polar control block scheme (Fig.4.1) misses some details related to how reference stator flux amplitude and torque reference are obtained in order to properly interpolate the load angle LUT.

First of all, input torque is limited to its maximum value ($T_{e,max}$) and, according to the actual injected field current, it must be properly limited as well. Moreover, since input torque is asked from the driver, if a certain field current able to afford that torque exists, reference field current is computed.
However, the other electrical parameter that limits torque in function of the actual field current, is the flux limit (related to stator flux amplitude, and it is the maximum value affordable with that specific field current).

Stator flux amplitude is limited by DC-link voltage and electrical synchronous speed

$$\lambda_{\text{lim}} = \frac{\text{V}_{\text{DC,max}}}{\omega_{\text{e}}} \cdot \text{k}_{\text{fw}} = \frac{\text{V}_{\text{DC}}}{\sqrt{3} \cdot \omega_{\text{e}}} \cdot \text{k}_{\text{fw}} \tag{4.5}$$

$$\omega_e = pp \cdot \omega_m = pp \cdot \frac{2 \cdot \pi}{60} \tag{4.6}$$

Where k is a gain with the purposes of accounting for inverter's voltage errors, and getting enough voltage margin to perform torque regulation with high dynamic also in FW operations:

$$0.85 < \text{k}_{\text{fw}} < 0.95 \tag{4.7}$$

This way, flux weakening operating points are taken into account, and, approaching to base speed, current and fluxes are reduced, thus reducing actual torque and getting higher speeds.

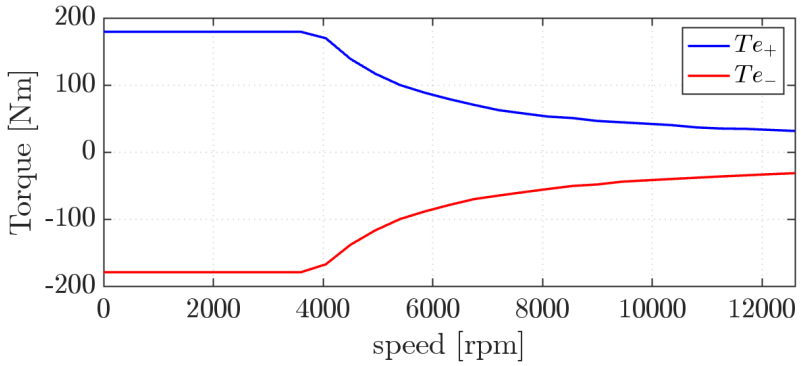

Figure 4.8: maximum torque per-speed profile for $i_f = 5[A]$.

Maps that allow to extract reference field current from actual flux limit and torque input, as well as torque limit from actual field current and flux limit, must be obtained. However, their computation is again trivial, since flux limit vector as function of torque levels and field current is instrinsically present into constrained maps (section 4.2).

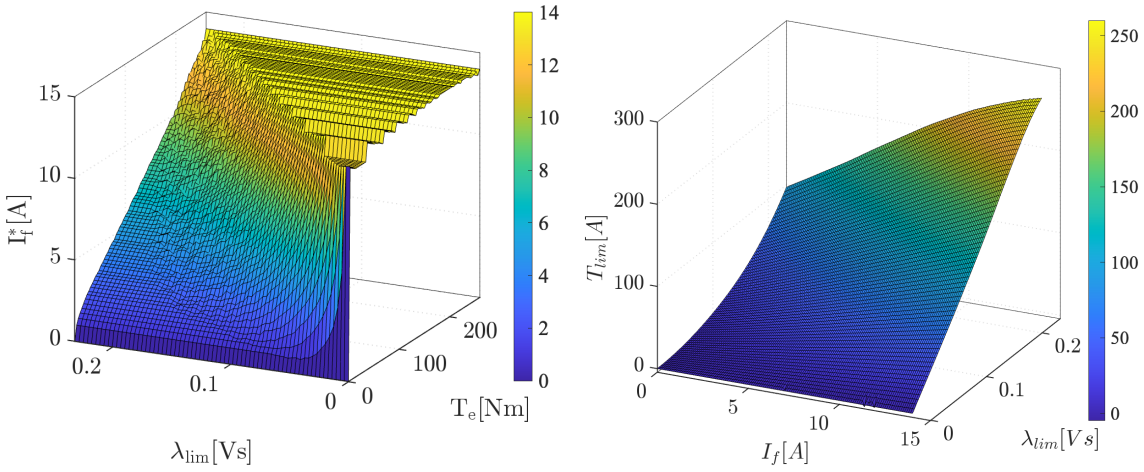

(a) (b)

Figure 4.9: Field current reference map (a), torque limit map (b).

Figure 4.9 (a) and (b) clearly shows limitations on the actual torque affordable by the machine in the specific working point, when a certain value of field current is injected, and when the actual speed limits the stator flux amplitude. For sack of clarity, according to (a), asking high torques at low flux limit needs high field current to be accomplished.

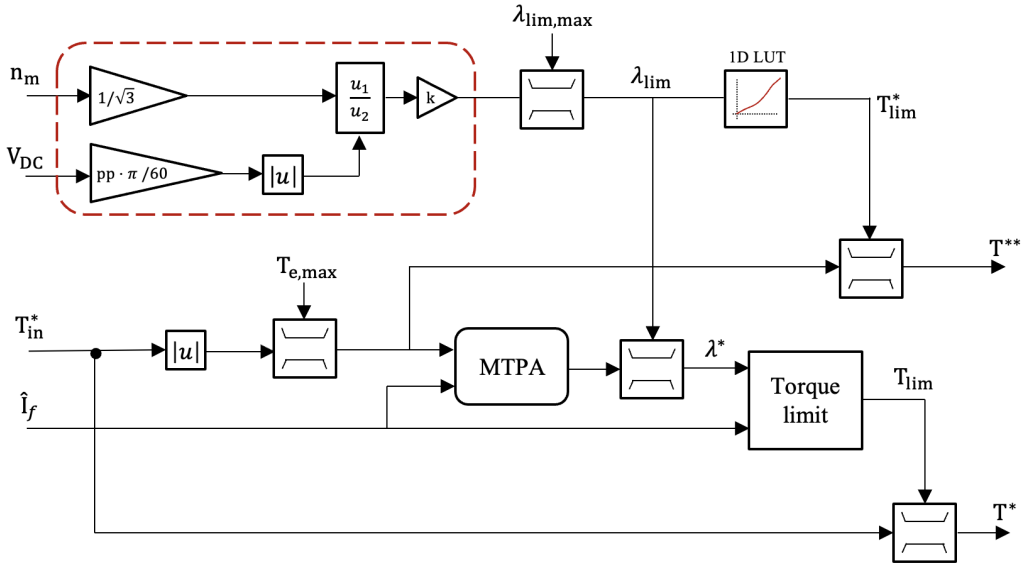

Figure 4.10: Reference generation block scheme.

Reference torque T** is the desired one, not taking into account actual field current limitation. It is crucial since, thanks to reference field current map (Fig.4.9 (a)), it will generate the field current needed to afford that torque level.

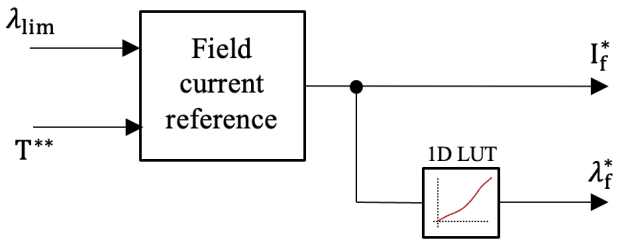

Figure 4.11: Reference field current interpolation.

4.4.1 Maps validation

Fluk Polar Control is established apart from load angle LUT, that generate reference load angle to be closed loop regulated. Thus, building this map is a delicate operation and must not include an error percentage that affects output controlled torque.
Once maps are computed, a validation test is performed: a Montecarlo test is taken into account, where a number of samples

$$N = 1.000.000$$

is tested to interpolate the load angle look-up table.
The bottom portion of the block scheme in Fig.4.10 is implemented in a Matlab script, starting from two reference vectors, one related to torque and the other related to speed, each of them filled with one million random numbers within the ranges

$$\begin{aligned} T_i &\in [0, T_{e,max}] \\ n_{m,i} &\in [0, n_{m,max}] \\ i &= 1, ..., N \end{aligned} \tag{4.8}$$

Once field current is fixed to a constant value, reference torque and stator flux amplitude are obtained according to 4.10, per-unit flux is computed and normalized load angle LUT is interpolated N times. From obtained values, fluxes in d and q axis are effortless reconstructed, since

$$\begin{aligned} \lambda_d &= \lambda \cdot \cos(\delta) \\ \lambda_q &= \lambda \cdot \sin(\delta) \end{aligned} \tag{4.9}$$

while currents in dq axis are obtained through inverse maps interpolation, so they are tested as well. These operations are repeated for each value of the field current.

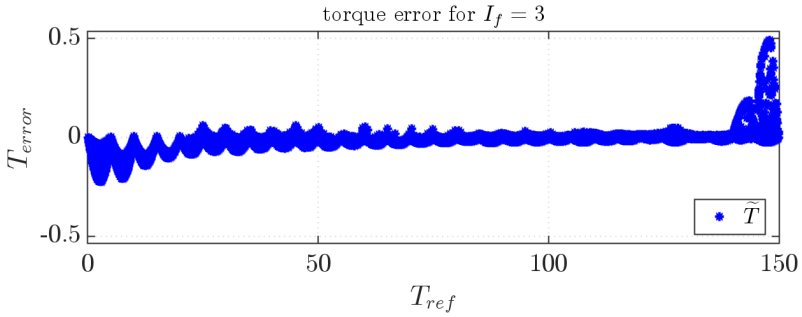

Figure 4.12: Montecarlo torque error (1).

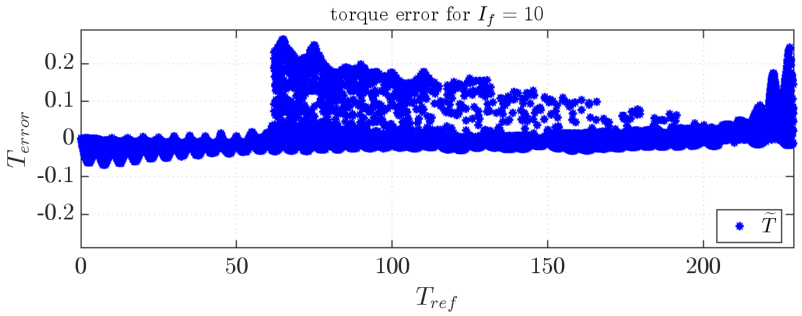

Figure 4.13: Montecarlo torque error (2).

Figures 4.12 and 4.12 show that, for instance, at field current equal to 3 and 10 [A], maximum torque error is 0.5 and 0.25 [Nm], respectively, out of a maximum torque affordable of 150 and 245 [Nm].
Obviously, torque error is computed for each field current level, then a total average torque error can be computed as

$$\bar{\tilde{T}}_{e,\%} = \frac{\sum_{i=1}^{n} \tilde{T}_{e,i,\%}}{n} \simeq 0.27\% \tag{4.10}$$

Equation (4.10) shows a quite good result from computed maps, since not even maximum error reaches more than 1% torque error qith respect to its maximum value.
Chapter 5 follows, where, since control maps are now computed, FPC missing details are reported, as the case of stator flux observer that feeds the closed loop control in stator *dqs* frame. Then, control algorithm can be established and tested in a simulation software environment, as the case of Simulink.

Chapter 5

FPC control

5.1 Background

According to section 1.3.4, FPC-based torque controllers perform closed loop regulation within stator *dqs* reference frame. Since *ds* axis corresponds to the position of the stator flux vector, whose angular displacement from the d axis exploit the load angle δ, voltage equations in *dqs* frame correspond to (1.15), and are reported again for sack of clarity

$$\begin{cases} v_{ds} = R_s \cdot i_{ds} + \frac{d}{dt}\lambda \\ v_{qs} = R_s \cdot i_{qs} + \lambda \cdot \frac{d}{dt}\delta + \omega \cdot \lambda \end{cases} \tag{5.1}$$

together with state-space equations

$$\frac{d}{dt}\lambda \simeq v_{ds} \tag{5.2}$$

$$\lambda \cdot \frac{d}{dt}\delta \simeq v_{qs} - \omega \cdot \lambda \tag{5.3}$$

Once resistive voltage drops are considered negligible.
At this point is well known that (5.3) shows no dependance on differential inductances, and, moreover, load angle control loop is independant on the machine's operating point.
Furthermore, (5.2) suggests that FPC operates with decoupled voltage margins: indeed, machine's back emf only focuses on *qs* axis, then, controlling stator flux amplitude requires only a negligible voltage margin to compensate for voltage drops in *ds* axis.

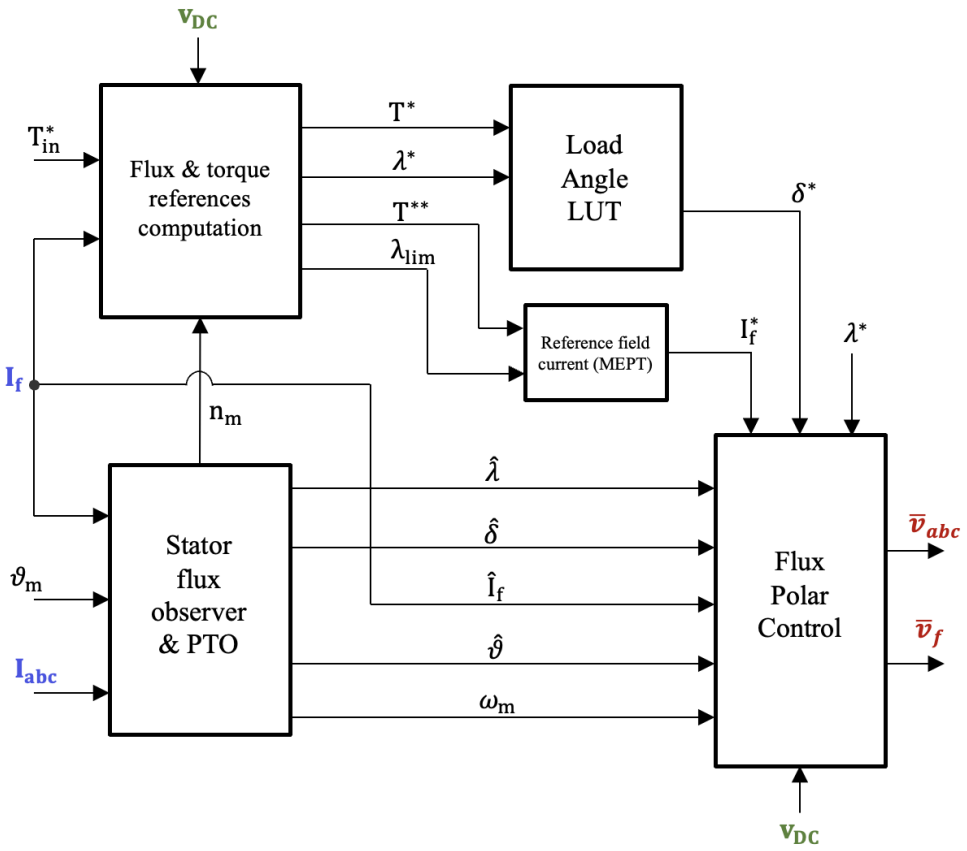

Figure 5.1: Proposed FPC-based torque controller.

This means that *qs* axis (where load angle closed loop regulation is performed) regulator can exploit almost all the voltage range made available by the inverter, thus leading to a very high torque regulation dynamic performance, even under voltage constraints [2]. Since closed loop control is expressed in *dqs* reference frame, a transformation, as function of the stator angle must be performed, once transformation angle is extracted directly from the motor, through stator flux amplitude. Despite the fact that stator flux amplitude is not measured, it is anyway obtained from the motor, but it will be observed through a stator flux observer.
Figure 4.1 shows that closed loop regulation needs stator flux amplitude and load angle to be feedbacked from the motor.

The following sections provide stator flux observer design, as well as a position tracking observer, able to provide mechanical speed from machine's angular displacement. The complete FPC-based torque controller block scheme becomes the one in Fig.5.1.

5.2 Stator Flux Observer

Stator flux observer is designed starting from *current-to-flux* relationship, i.e. flux maps already established in Chapter 2, and easily interpolated, once giving as input current amplitude and phase, as well as actual rotor field current.

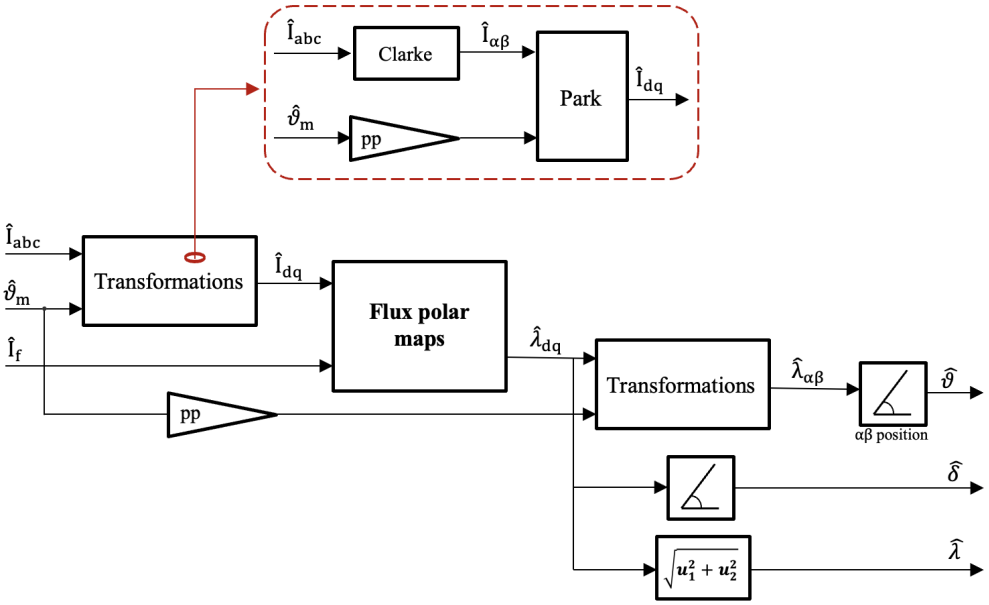

Figure 5.2: Stator flux observer.

Indeed, the estimator only requires a feedback from motor phase currents (I_{abc}) and rotor mechanical position (ϑ_m). Hence, Clarke and Park transformation are applied to bring currents in rotor dq frame, where flux polar maps are computed and interpolated to get fluxes in corresponding axes, as shown in Fig.5.2.
Then, stator flux in $\alpha\beta$ coordinates allows to directly compute the ds-axis position $\hat{\vartheta}$, while load angle and stator flux amplitude are straightforwardly computed from $\hat{\lambda}_{dq}$.

5.3 Position Tracking Observer

On the other hand, mechanical rotational speed is phyisically defined from angular position time derivative, but it's not the best choice when approaching digital control. If ω_m is obtained from discrete difference normalized by sampling time

$$\frac{\vartheta_m^{(k)} - \vartheta_m^{(k-1)}}{T_s} \tag{5.4}$$

the result leads to highly noisy output when discontinuities are encountered. As alternative it is possible to consider the sine of the difference, since, for small variations, its behaviour is considered linear and sine function is equal to its argument. Nevertheless, output must be filtered as well.

$$\frac{sin(\vartheta_m^{(k)} - \vartheta_m^{(k-1)})}{T_s} \tag{5.5}$$

Problems arise when the difference is not small enaugh, since error increases and linearity is lost.
Indeed, a better approach is a one including integrals instead of derivatives. It can be found in solutions that try to emulate the real physical system, feedbacking measured signals and letting the computed error to be input of a regulator

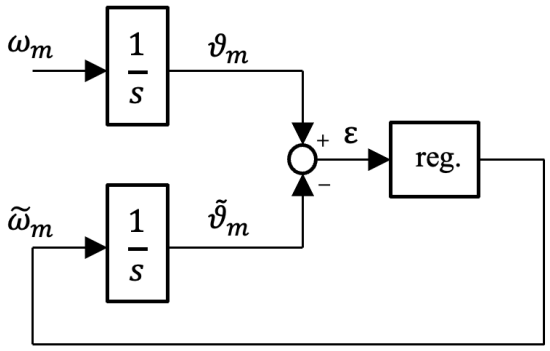

Figure 5.3: Position Observer structure.

The only variable to be measured is the angular position (ϑ_m), the observer generates an estimate of the same variable, with an approach based on minimizing the error, thus including a PI regulator.
Again, to avoid discontiuity errors, difference between measured and estimated angular position is considered within a sine function: however, this time its argument will be always small, as PI forces error to zero.

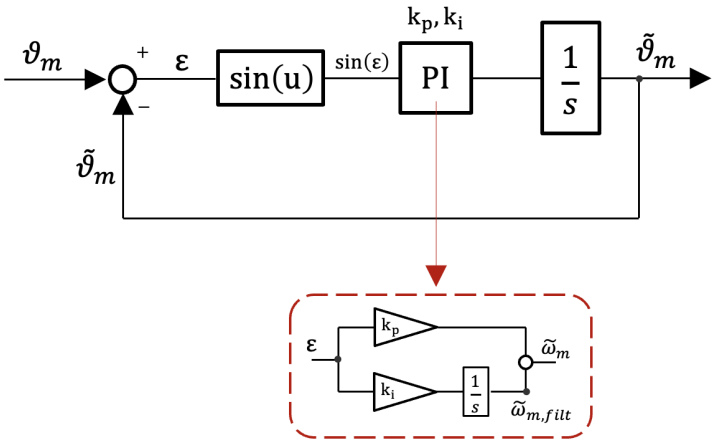

Figure 5.4: PTO block scheme.

Then, mechanical angular speed ($\tilde{\omega}$) can be obtained, already filtered, by integration, as shown in the complete observer scheme (Fig.5.4)
From block scheme 5.4 it is possible to extract PI gains in function of the phase margin (φ_m) and cut-off frequency (ω_b)

$$\begin{cases} k_p = \frac{\omega_b \cdot \tan(\varphi_m)}{\sqrt{1+\tan^2(\varphi_m)}} \\ k_i = \frac{\omega_b^2}{\sqrt{1+\tan^2(\varphi_m)}} \end{cases} \tag{5.6}$$

where phase margin is kept to 60° and bandwidth doesn't need to be too much wide, hence

$$\begin{cases} \varphi_m = 60° \\ \omega_b = 2 \cdot \pi \cdot f_b \end{cases} \tag{5.7}$$

where

$$f_b = 20 \div 30[\text{Hz}] \tag{5.8}$$

Moreover, (Fig.5.4) represents the structure of a model reference adaptive system, as it is based on system mathematical model: this particular adaptation is instead known as Position Tracking Observer (PTO).

5.4 Closed Loop Control

5.4.1 Stator Flux Amplitude and Load Angle regulators

Observed stator flux amplitude and load angle are the feedbacks of the FPC torque controller block scheme in Fig.5.1, together with stator angle $\hat{\vartheta}$, required to implement the control in *dqs* reference frame.
Indeed, closed loop control of stator flux amplitude and load angle is implemented with PI regulators, and reference phase voltages $\bar{v}^*_{abc}$ are reconstructed from *dqs* voltages v^*_{ds}, v^*_{qs}, to be able to exploit all the advantages mentioned in Section 5.1. Again, according to Section 5.1, *ds* axis reference voltage v^*_{ds} must only compensate

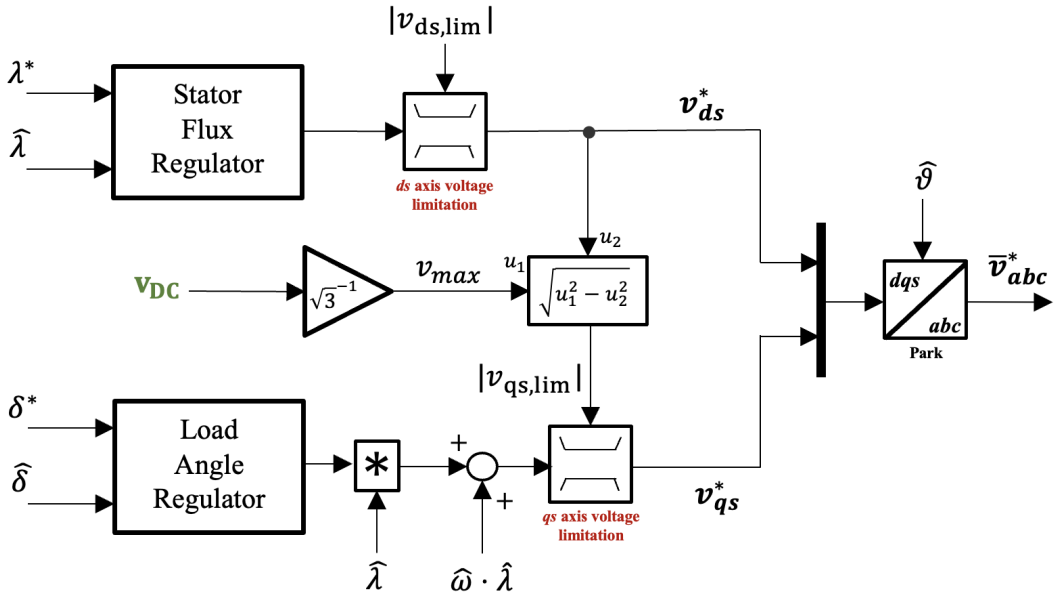

Figure 5.5: Stator flux amplitude and load angle closed loop control.

for a resistive voltage drop (eq.(1.15)), then, to avoid a useless reduction of the voltage margin in *qs* axis, v^*_{ds} is properly limited to a lower voltage level, with respect to v^*_{qs}. Moreover, this limit must ensure the control of the stator flux amplitude in any operating condition [2].
With the hypothesis of an ideal inverter, *ds* axis voltage limit is computed as

$$v_{ds,lim} = (2 \div 5) \cdot R_s \cdot I_{max} \tag{5.9}$$

Simulations in this thesis work are performed taking 5 as a multiplying constant.

On the other hand, qs axis and load angle are handled considering that: (i) feedforward term ($+\omega \cdot \lambda$) is strongly recommended to increase torque regulation dynamic performances, even in deep FW operations; (ii) load angle regulation can be straightforwardly pinned to any machine's operating point once its output is properly normalized (scaled) to the feedbacked (observed) stator flux amplitude (as shown in Fig.5.5.
Further advantage obtained from FPC resides within PI tuning, that turns out to be immune on machine's operating point (no inductances dependance) and machine's topology. As a matter of fact, according to the open loop transfer function of load angle (formally the same as stator flux amplitude one), proportional anf integral gain can be computed as follows:

$$\begin{cases} k_p = g_r \cdot k_i \\ k_i = \omega_b^2 \cdot \sqrt{\frac{1+(\tau_d \cdot \omega_b)}{1+(g_r \cdot \omega_b)}} \end{cases} \tag{5.10}$$

where

$$g_r = \frac{\tan(\varphi_m + \arctan(\tau_d \cdot \omega_b))}{\omega_b}$$

Moreover, in (5.10), ω_b [rad/s] refers to the crossover frequency of the loops, while phase margin is represented by φ_m.
Instead, term τ_d refers to the overall execution delay introduced by digital controller and PWM modulation, and it is exploited as

$$\tau_d = \frac{1}{f_s} + 0.5 \cdot \frac{1}{f_{sw}} \tag{5.11}$$

where f_s and f_{sw} respectively represent sampling and switching frequency.
Simulations are made considering a crossover frequency $\omega_b = 3$ [kHz].

5.4.2 Field current control loop

In the case of a WFSM, rotor electrical quantities must be controlled as well: PI regulator is considered to regulate field current, starting from the one measured from the motor.
According to section 4.4 and block scheme in Fig.(5.1), field current reference (I_f^*) is computed and compared with the one output from the motor ($\hat{I}_f$).

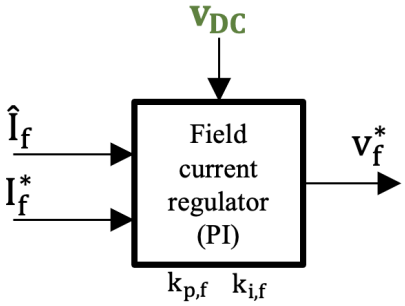

Figure 5.6: Field current regulator.

Here the regulation will be the same as a one employed for a FOC controller, thus gains are modeled on the rotor field differential inductance l_f and same problems related to FOC are expected

$$\begin{cases} k_{p,f} = l_f \cdot \omega_b \\ k_{i,f} = R_f \cdot \omega_b \end{cases} \tag{5.12}$$

where l_f is taken around the order of mH, e.g. $l_f = 50mH$.
Nevertheless, adapting the field current according to the differential inductance is not a big issue as happens for FOC, since rotor windings dynamics doesn't need to be pushed to high values. In this case crossover frequency is taken as $\omega_b = 1.5[kHz]$. Then, control algorithm can be fully established, once MCU block (which contains observer, control maps and closed loop control) is properly designed in a discrete-time domain, thus considering a clock signal that triggers MCU ones.

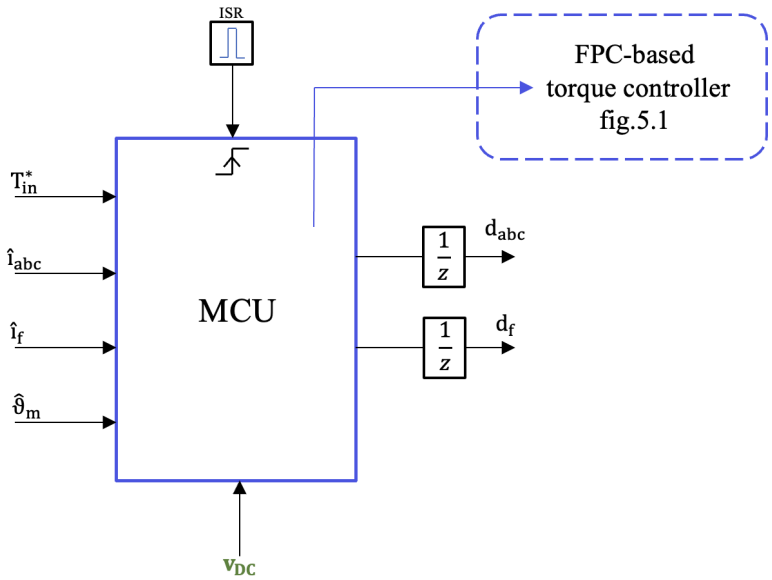

Figure 5.7: FPC torque controller, MCU scheme.

According to Fig.5.7, MCU block is triggered to clock *rising edges*, related to the ISR block (Interrupt Service Routine). Furthermore, duty cyle from both VSI and DCDC converters is applied at next sampling point, once they are interposed by unit delay blocks.

5.5 Results

Simulation results of the proposed FPC control algorithm, tested on the model of a Wound Field Synchronous motor are performed in the following conditions:

I. *Maximum torque per speed (MTPS) profile*

II. *Fast torque reversals*

I. Maximum Torque per Speed (MTPS) Maximum torque per speed profile represents maximum torque affordable my the machine when approaching to increasingly higher speeds, exploiting FW operations (Fig.4.8).

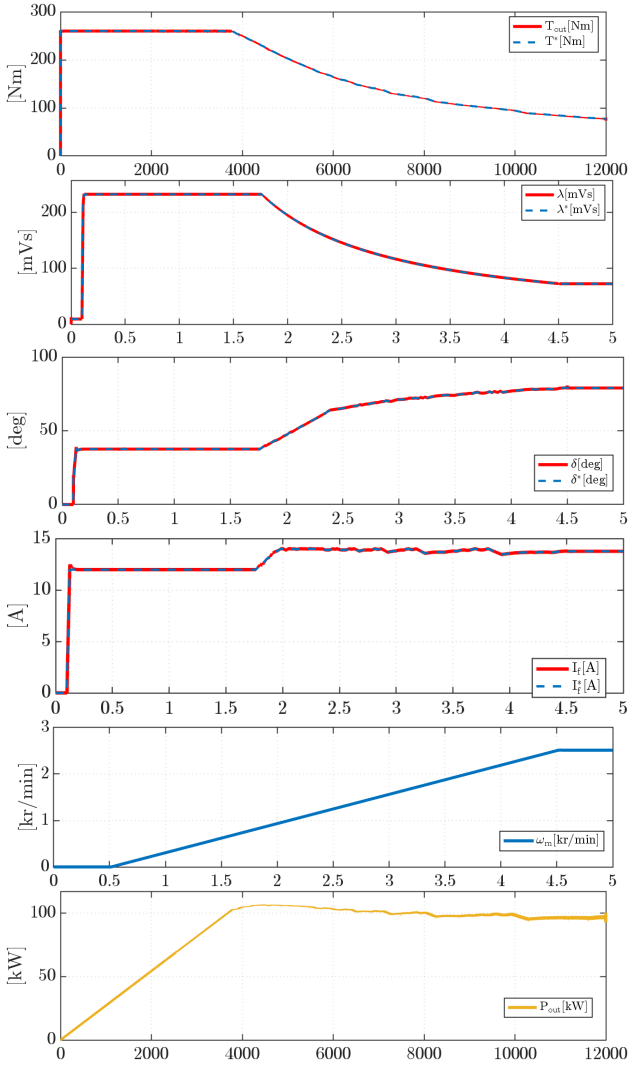

Figure 5.8: WFSM MTPS profile in the range 0-12000 rpm and $v_{DC} = 350V$.

Input torque is the maximum one affordable by the machine, imposed by a step variation, from zero to $T_{e,max}$: as speed approaches to base speed, it increases apart from a torque reduction, imposed by magnetic flux reduction.

II. Fast torque reversal Second test is instead made once feeding torque input with pulses from $T_{e,max}$ to $-T_{e,max}$, thus asking maximum and minimum torque with a period of 0.25s along MPTS profile.

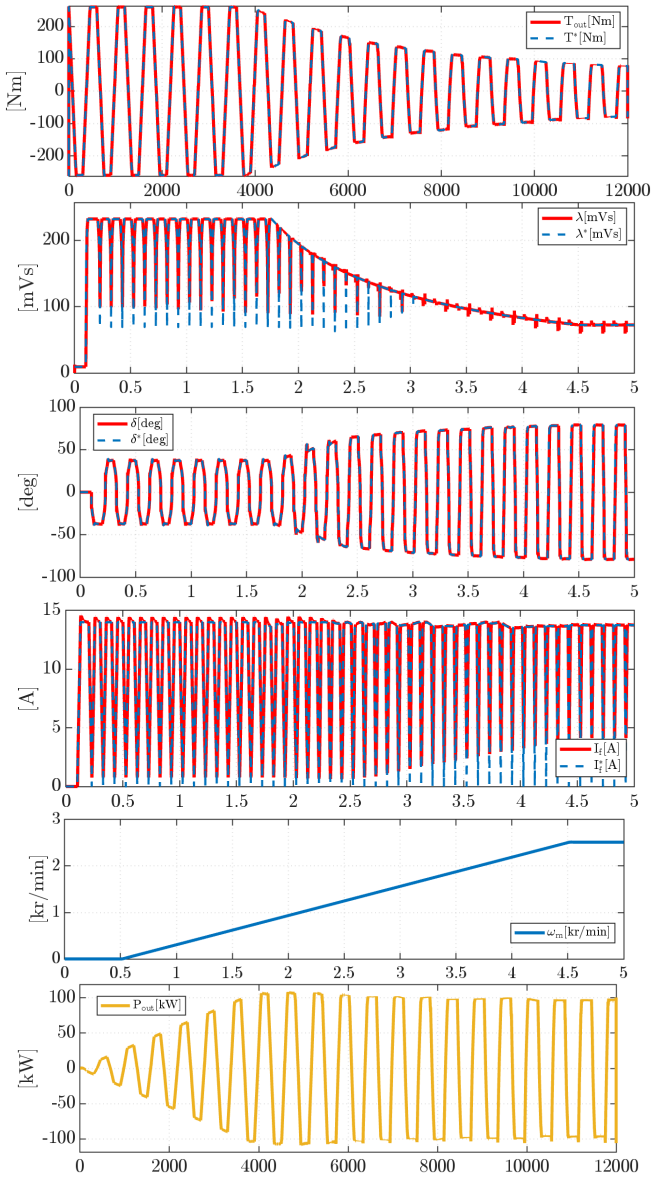

Figure 5.9: WFSM fast torque reversal test in the range 0-12000 rpm and $v_{DC} = 350$V-

This test doesn't reflect a real scenario, but turns out to be a good one to demonstrate the high dynamic performances of the proposed FPC control, applied on a WFSM. Indeed, according to the bottom plot of Fig.5.9, FPC allows to extract almost all the power range of the machine, thanks to decoupled voltage margins exploited in last sections: this result is not easily reachable with, for example, a CVC-FOC control algorithms.

Chapter 6

Experimental validation

6.1 Working environment

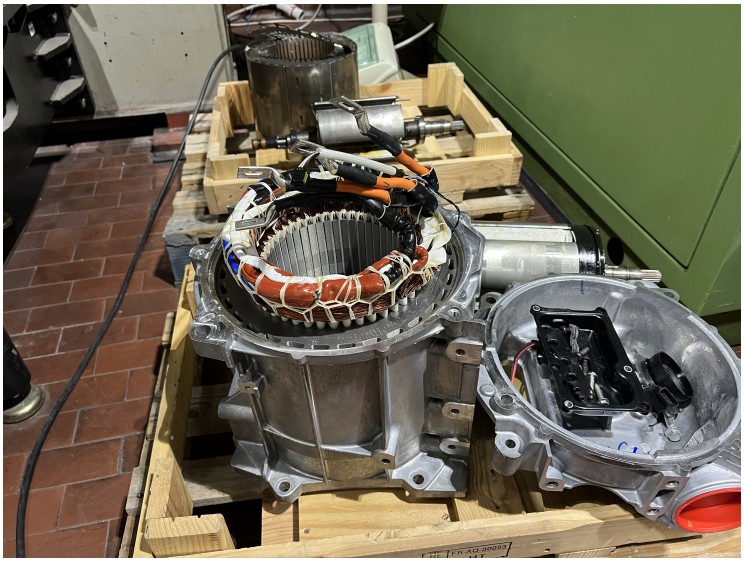

Figure 6.1: Machine under test, Renault ZOE 135 WFSM.

As already mentioned in Chapter 2, MUT is connected to a driving machine (usually bigger than MUT), that imposes the speed, beyond which tests are performed.

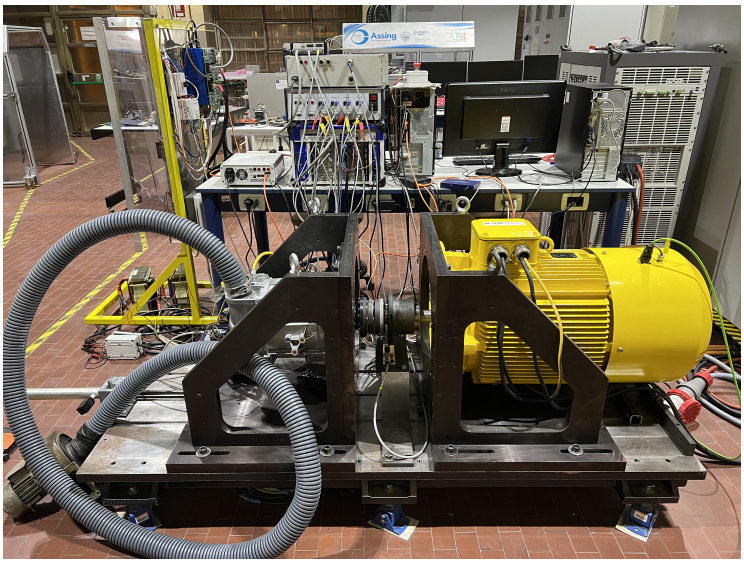

Figure 6.2: Test bench: driving machine (right), MUT (left).

The motor used for experimental validation is a 100kW EESM adopted by Renault ZOE R135, whose primary data are listed in table 4.1.
The motor under test (MUT) has been mounted on a test rig for the identification of the flux and torque maps first, then validation of the proposed motor control algorithm.

The MUT has been connected to a driving machine (DM) acting as a prime mover, as shown in Fig.6.2. The torque transducer T40B from HBK Gmbh has been mounted along the machanical coupling between the MUT and DM. The power converter feeding the stator consists of a three-phase inverter module, rated 600V, 800A, fed at 350V by a bidirectional DC source. It is noted that the power rating of the VSI is much higher than the motor maximum power. Indeed, this VSI is a laboratory prototype for generic high voltage and current applications. The power converter feeding the rotor, instead consists of a H-bridge DCDC converter, rated 600V, 45A, connected to the same DC-link used by the stator VSI.

The digital controller, where motor identification procedure and motor control algorithm have been implemented is the fast prototyping board dSPACE MicroLab-Box. All the control algorithms have been developed in C code. Switching and sampling frequency of both power converters have been set at 5kHz for the identification procedures. Conversely, the motor control algorithms will be implemented using 16-20kHz to provide a compatible scenario with the automotive implementations.

The measurements setup is shown in Fig.6.3. It is noted that for the stator winding, two line to line voltages and phase currents have been measured, emulating an Aron configuration. The phase currents have been measured using the closed loop

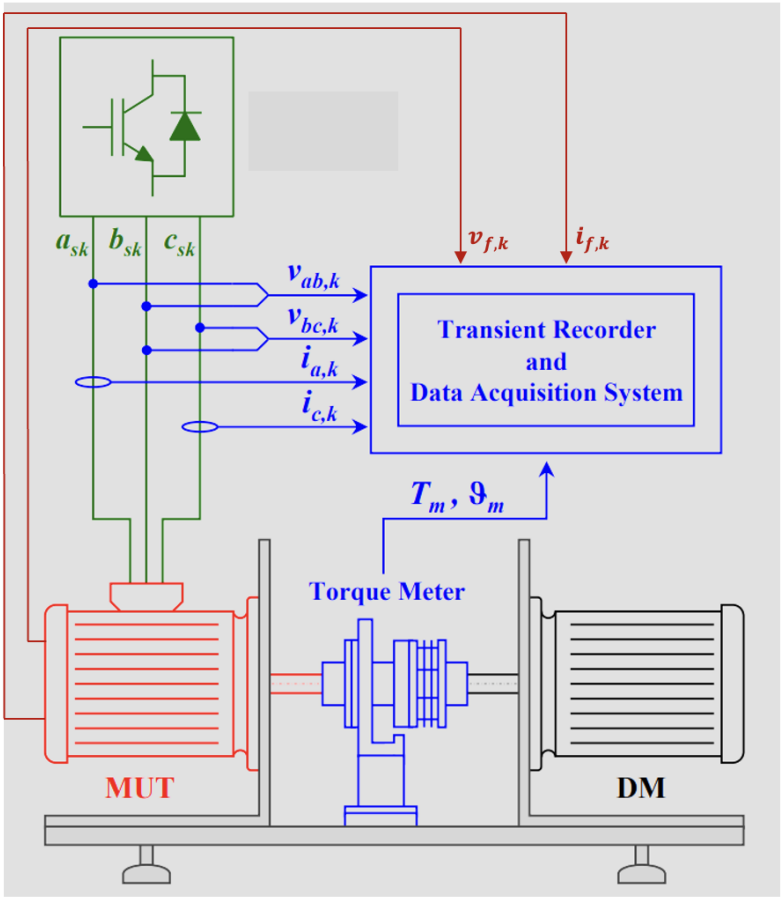

Figure 6.3: Measurements block scheme at sampling point k.

current transducers IT 605-S Ultrastab from LEM, consisting of closed loop Hall effect sensors. The line to line voltages have been measured using shielded cables (due to PWM) connected to high voltage/high resolution voltage cards GN610B from HBM Gmbh. Regarding the rotor winding, the field current has been measured using the closed loop current transducer IT200-S Ultrastab from LEM, while the field voltage has been measured similarly with respect to the stator ones.
Finally, all data have been collected by the calibrated transient recorder and data acquisition system GEN7tA from HBM Gmbh. The identification procedure of flux and torque maps has been performed at a MUT speed of 240rpm, imposed by the DM.

6.2 Results

This section provides all the results coming from experimental identification of the machine's magnetic model, with performance profiles, as well as inductances maps. Nevertheless, experimental identificaion is compared with finite element ones. Just for reminder, all the proposed results are obtained for each field current level, in the range

$$\mathrm{I_f} \in (0, 14)[\mathrm{A}] \tag{6.1}$$

First of all, MMI sample points of current and fluxes in dq frame are considered, then torque is computed and compared with the one measured, as they coincide, according to Fig.6.6

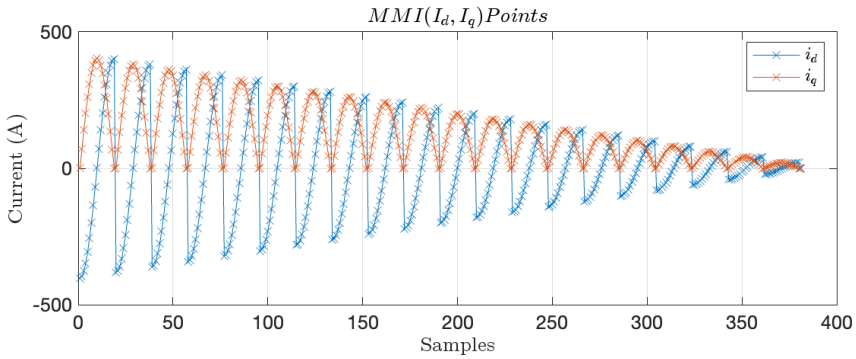

Figure 6.4: $\mathrm{I_d}, \mathrm{I_q}$ sample points for $\mathrm{I_f} = 0$.

Where negative q-axis currents are not considered thanks to symmetry properties.

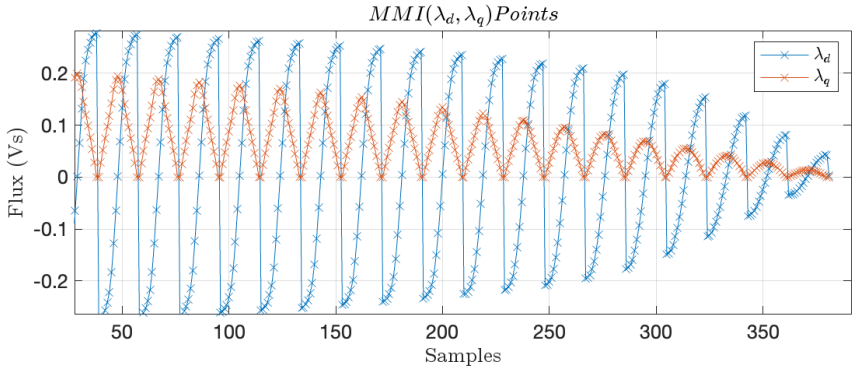

Figure 6.5: $\lambda_{\mathrm{d}}, \lambda_{\mathrm{q}}$ sample points for $\mathrm{I_f} = 0$.

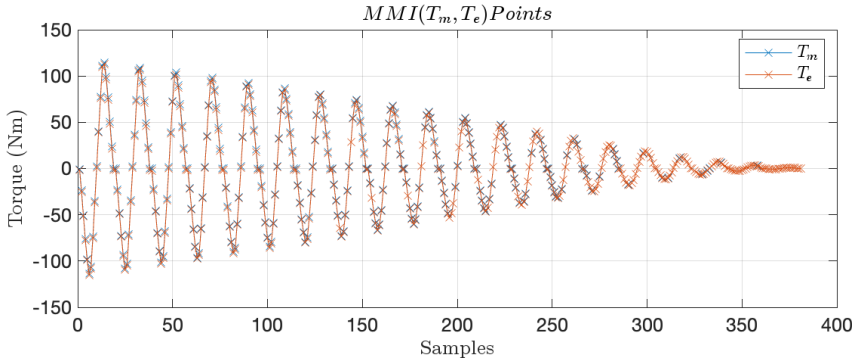

Figure 6.6: $\mathrm{T_e}, \mathrm{T_m}$ sample points for $\mathrm{I_f} = 0$.

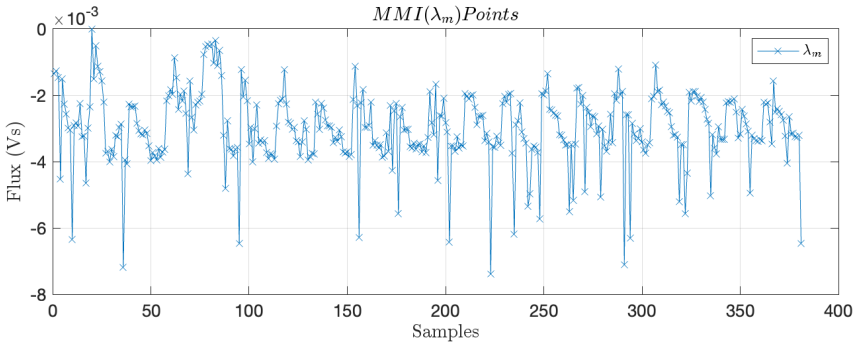

Figure 6.7: Rotor flux for $\mathrm{I_f} = 0$.

Here it's important to mention that Fig.6.7 represents the rotor flux, that it's not varying with temperature, as the case, for example, of a PMSM.
Then maps are computed in the same way as it's expressed in Chapter 2, as shown in following figures.

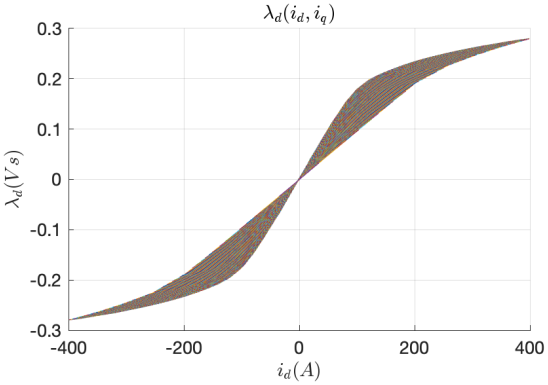

Figure 6.8: $\lambda_d(i_d, i_q, i_f = 0)$.

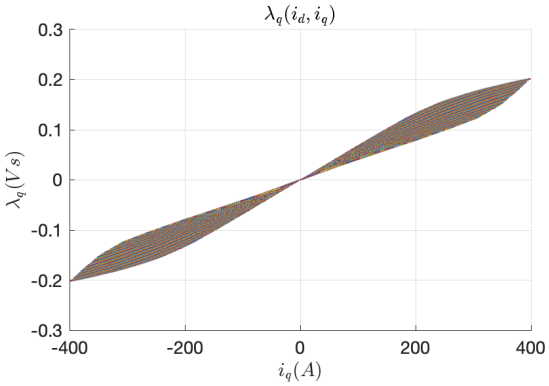

Figure 6.9: $\lambda_q(i_d, i_q, i_f = 0)$.

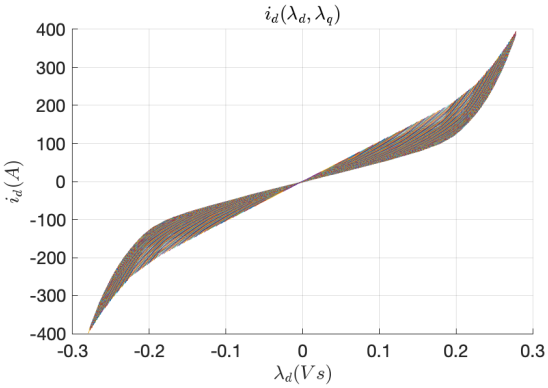

Figure 6.10: $i_d(\lambda_d, \lambda_q, i_f = 0)$.

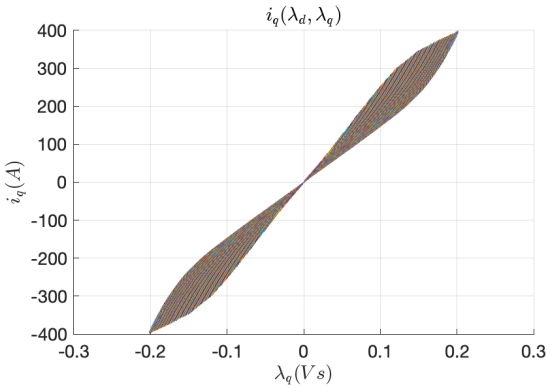

Figure 6.11: $i_q(\lambda_d, \lambda_q, i_f = 0)$.

Starting from data exploited in figures from 6.4 to 6.11, MTPA, MTPV and MTPS profiles are reported

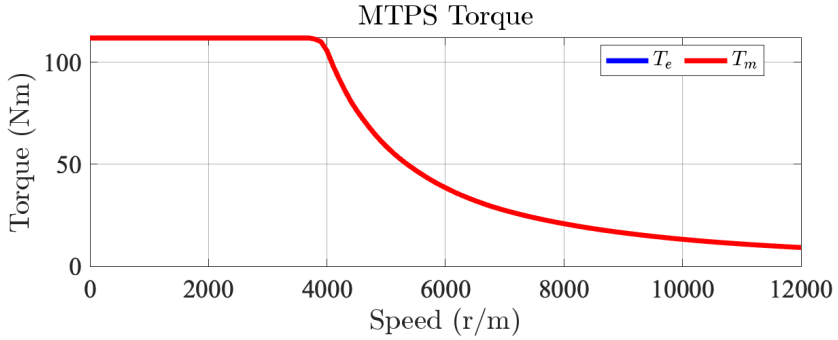

Figure 6.12: MTPS torque for $I_f = 0$.

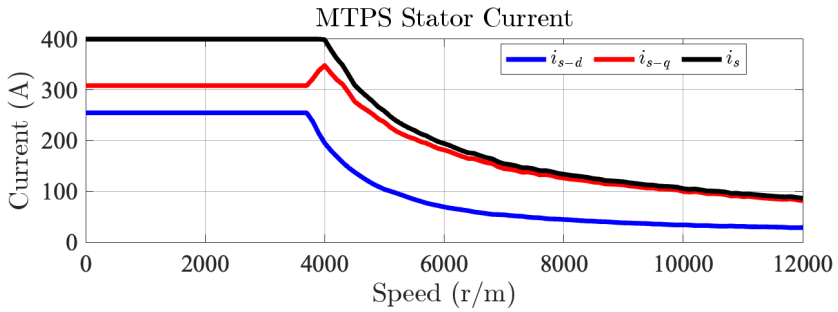

Figure 6.13: MTPS stator currents for $I_f = 0$.

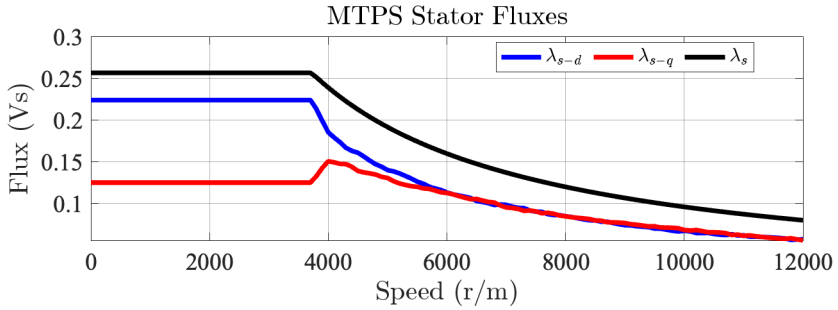

Figure 6.14: MTPS stator fluxes for $I_f = 0$.

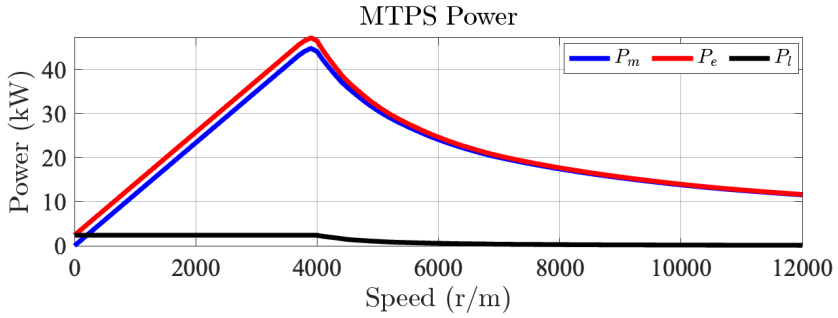

Figure 6.15: MTPS power for $I_f = 0$.

Power contribution related to Jaule losses is reported for sack of clarity, but it's not considered in this thesis work, since control is focused on achieving high dynamic performances.

Again, according to A.2, MTPA and MTPV profiles are computed, but FEM and experimental profiles are compared.

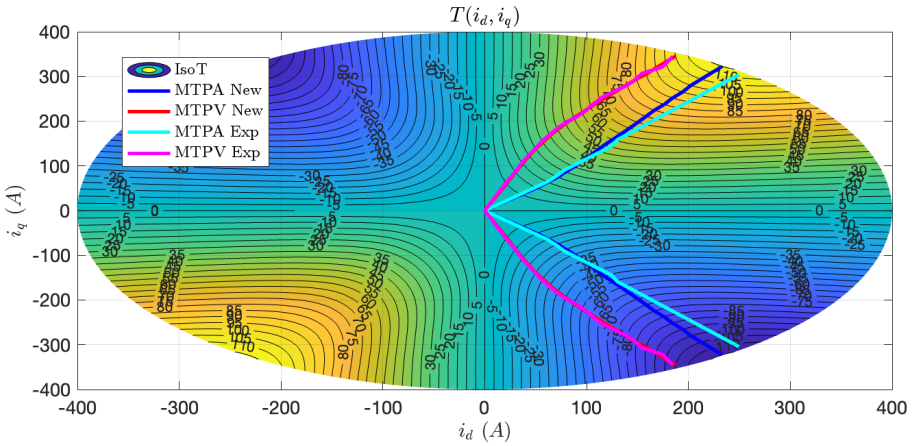

Figure 6.16: MTPA-V, FEM vs Experimental for $I_f = 0$.

Here is some error between Fem and experimental maps, related to experimental noises. Nevertheless, it will be less evident when considering higher field currents. Indeed, all the figures provided so far are referred to the first field current level, i.e. $I_f = 0$, hence, for instance, figures from 6.12 to 6.15 show a maximum torque and a maximum power that are not the machine's absolute one, instead affordable at maximum field current.

$$I_f = 14[A]$$

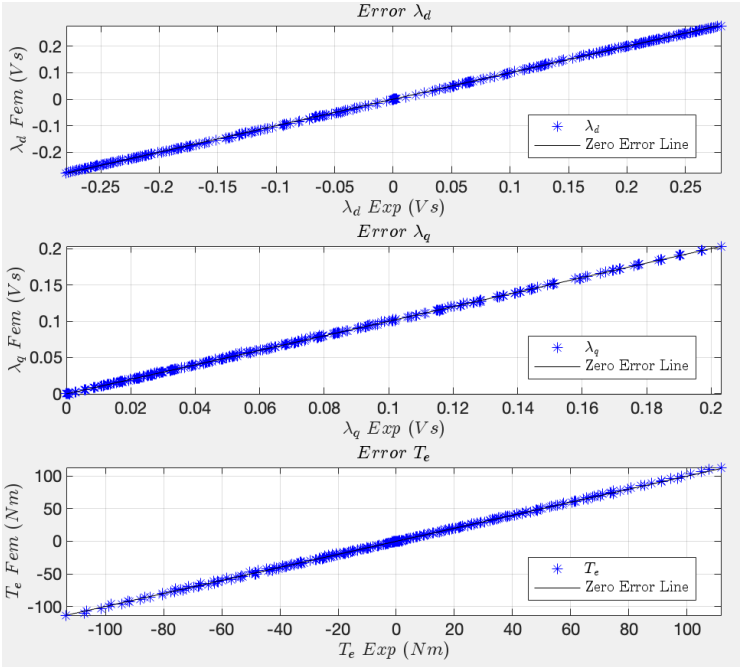

Figure 6.17: fem vs exp error for $I_f = 0$.

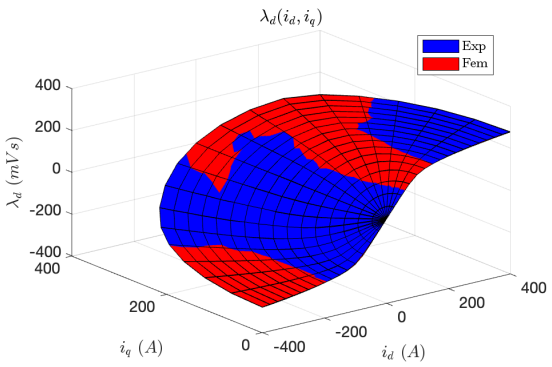

Figure 6.18: $\lambda_d(i_d, i_q, i_f = 0)$, fem vs exp.

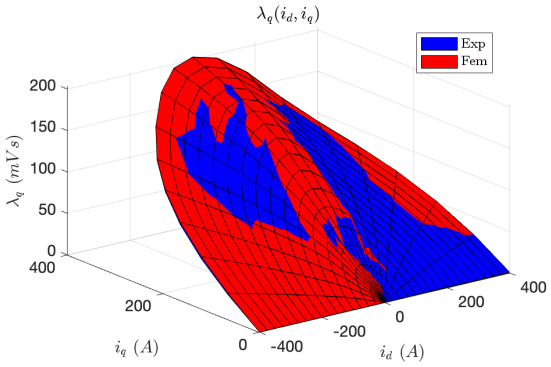

Figure 6.19: $\lambda_d(i_d, i_q, i_f = 0)$, fem vs exp.

As already mentioned, all of the reported profiles are repeated for each field current value, with a decreasing error once approaching higher field current values. For sack of clarity, next figures are related to a maximum field current.

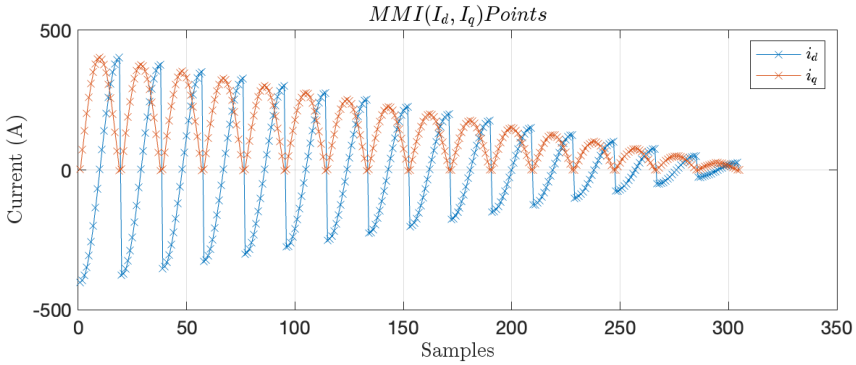

Figure 6.20: I_d, I_q sample points for $I_f = 14$.

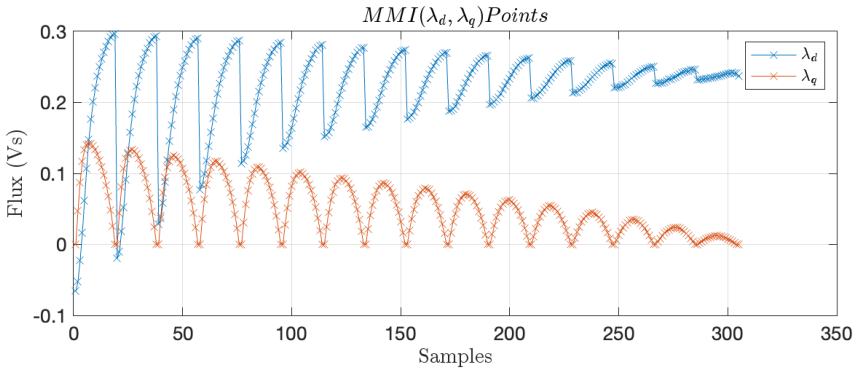

Figure 6.21: $\lambda_{\mathrm{d}}, \lambda_{\mathrm{q}}$ sample points for $\mathrm{I_f} = 14$.

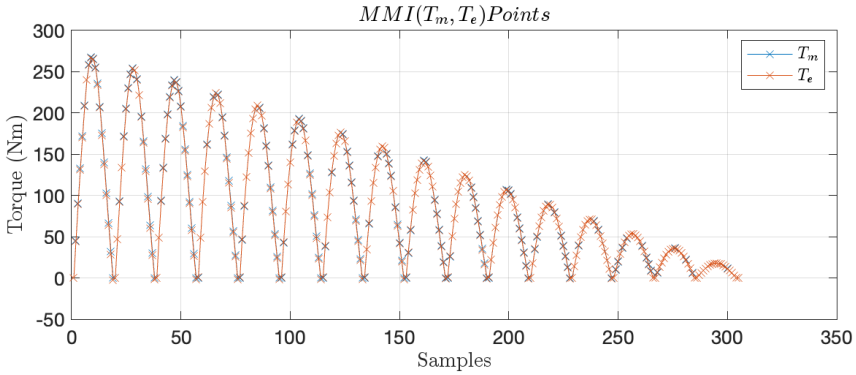

Figure 6.22: $\mathrm{T_e}, \mathrm{T_m}$ sample points for $\mathrm{I_f} = 14$.

Notice that, from Fig.6.22, maximum torque affordable by the machine corresponds with the maximum one reported in table 4.1.

Same results are obtained when considering MTPS profiles, that exploit maximum machine performances, regarding output power as well.

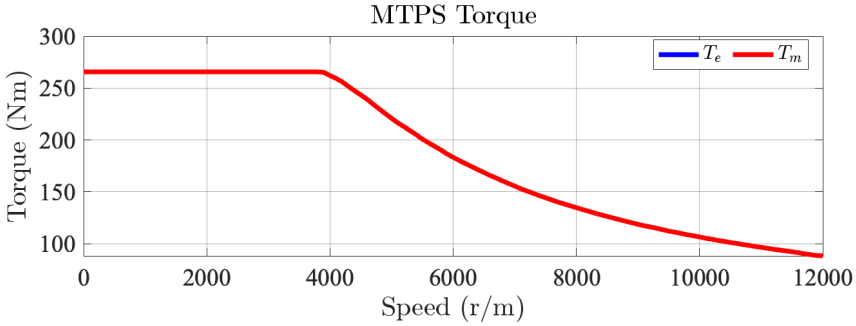

Figure 6.23: MTPS torque for $\mathrm{I_f} = 14$.

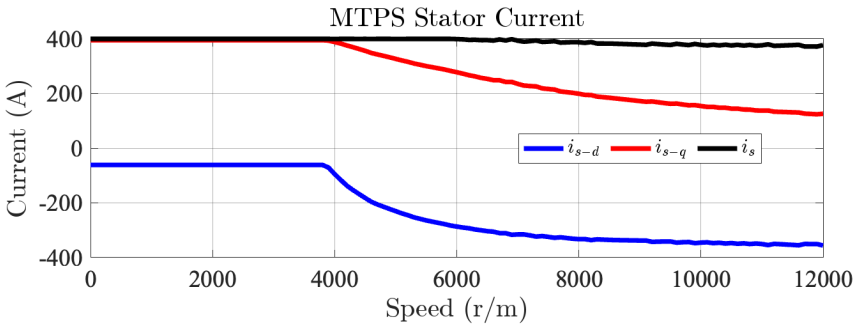

Figure 6.24: MTPS stator currents for $I_f = 14$.

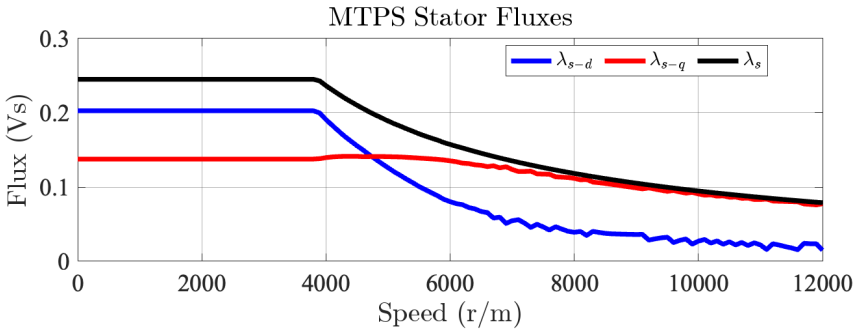

Figure 6.25: MTPS stator fluxes for $I_f = 14$.

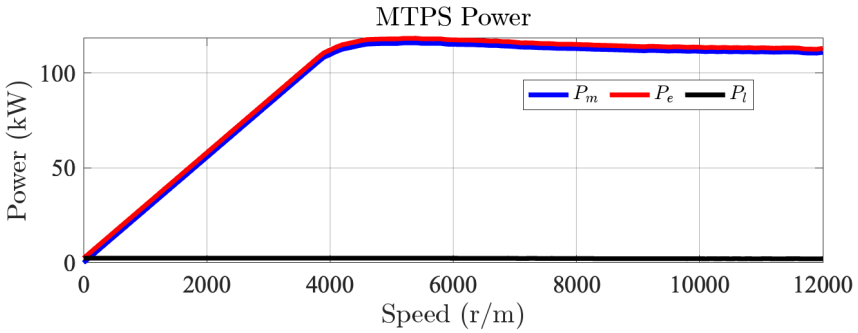

Figure 6.26: MTPS power for $I_f = 14$.

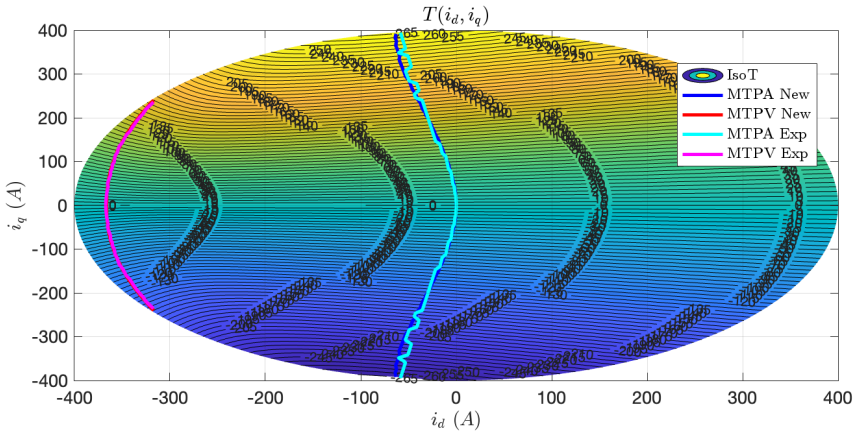

Figure 6.27: MTPA-V, FEM vs Experimental for $I_f = 14$.

Again, these profiles are compared with FEM ones (same as Fig.6.16), with a predicted error that is lower with respect to previous one, as shown in Fig.6.27

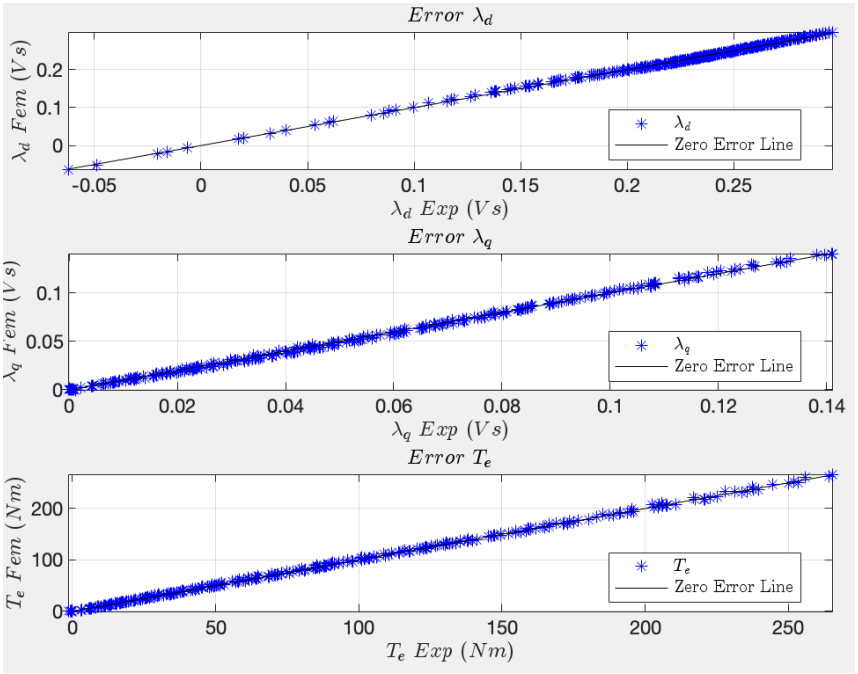

Figure 6.28: fem vs exp error for $I_f = 14$.

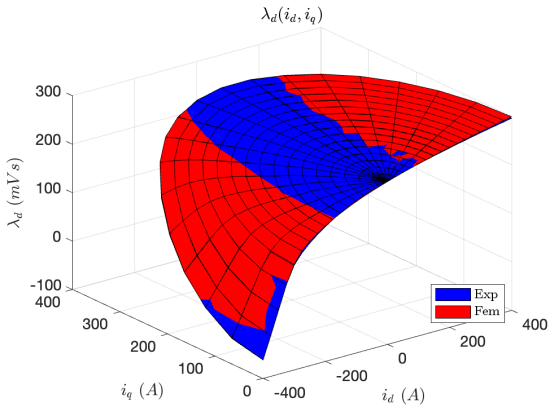

Figure 6.29: $\lambda_d(i_d, i_q, i_f = 14)$, fem vs exp.

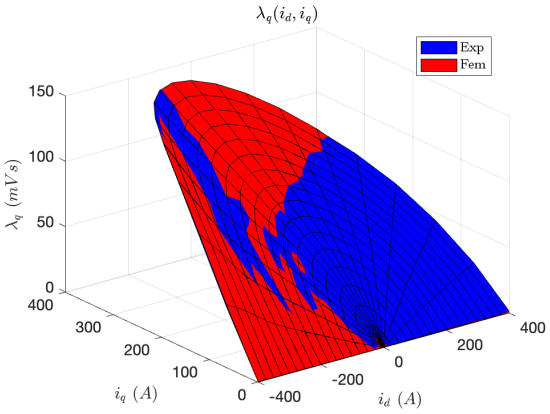

Figure 6.30: $\lambda_d(i_d, i_q, i_f = 14)$, fem vs exp.

Eventhough the applied torque control algorithm is a FPC-based one, that is immune to non-linear inductances variations (see equations(5.2) and (5.3)), inductances mapping is anyway performed, as shown in the following figures

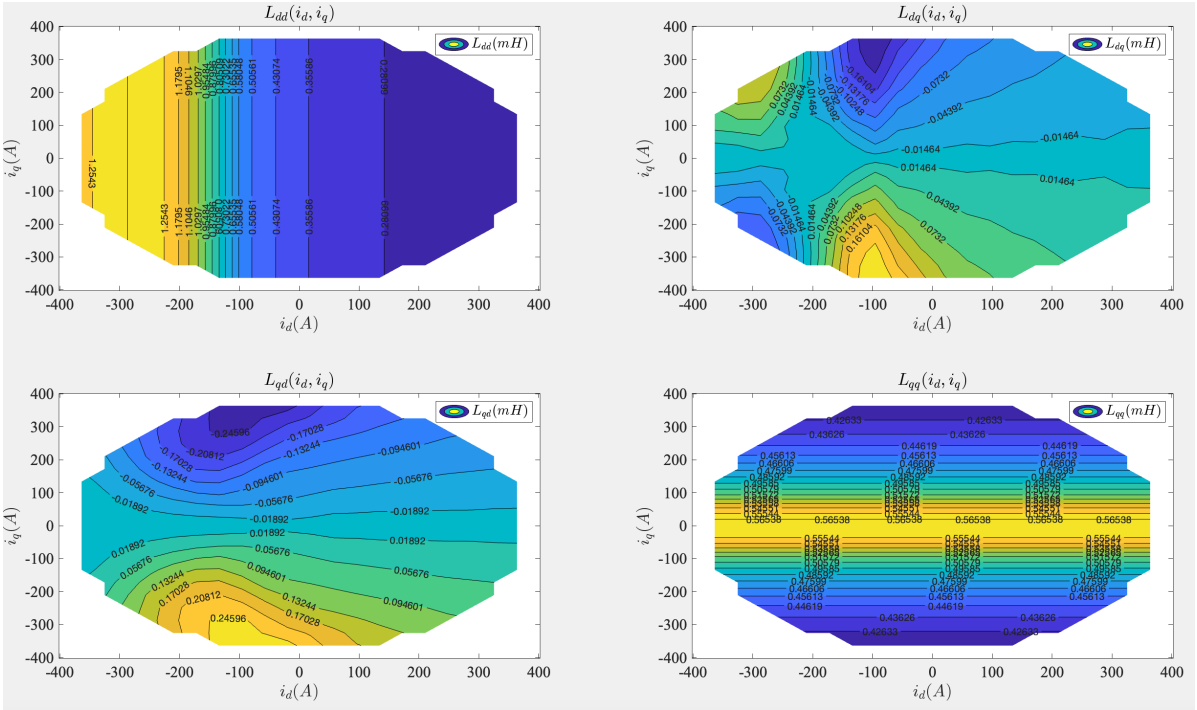

Figure 6.31: Apparent inductances mapping for $I_f = 7$.

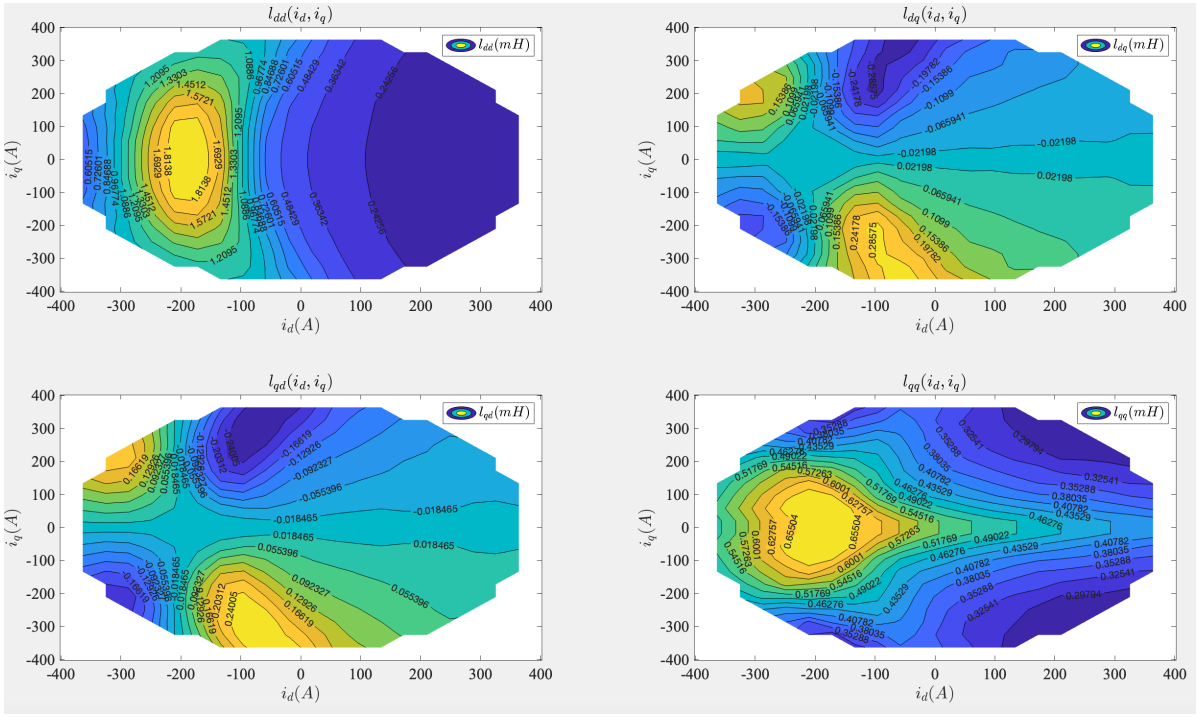

Figure 6.32: Differential inductances mapping for $I_f = 7$.

Chapter 7

Conclusion

This project showed how a torque controller for high dynamic performance purposes can be designed, proving that FPC-based ones are one of the best choices.
As a matter of facts, FPC respects all the demanding technical requirements needed to implement a torque controller for traction eDrives, summarized as: (i) unified torque controller, able to deal with any AC motor, from syncrhonous machines to induction motors, without changing its structure; (ii) torque regulation must be linear and has to include all the machine's limitations, as well as MTPA, MTPV and MTPS profiles; (iii) the performances of all inner control loops must be independant of machine's operating point, otherwise, the execution of tuning procedures requiring dedicated test rings is necessary; (iv) the control must guarantee high dynamic performances, again, in each operating point, including deep flux weakening operations, as it is not unusual to perform fast torque reversal in these demanding considitions; (v) at the end, the algorithm should adopt a control scheme that is easy to implement, thus minimizing the number of control modules.
Furthermore, apart from what is written in the introduction, high dynamic performances can be also obtained from a kind of motor, like the WFSM, that is highly saturated and lacks of the advantages of permanent magnets. This is just one of the solutions adopted to improve BEVs sustainability, while research will lead to more and improved solutions.
Indeed, eventhough experimental results (to be compared with simulated ones in Chapter 5) are not included, these topics will be faced in the next years, during my post graduate studies.

Appendix A

Appendix

Listing A.1: Magnetic model intentification

```
%% Flux maps computation (MAIN)
Np = 127;

%% extracting parameters from motor measurements
M = readtable("measurements.xlsx");
M = table2array(M(:,3:7));

% data provided is made up with voltage Vs, active
% and reactive power (P,Q)
P  = M(:,3);
Q  = M(:,4);
Vs = M(:,5);

nm = mean(M(1,2));
wm = (nm/60)*2*pi;
p  = 5;
w  = p*wm;
Rs = 5.5e-3;
J  = [0 -1;1 0];

% upload test currents
load idq_test.mat
```

```
%% voltage computation
% solution of a system with two unknowns vd1,vq1 (v+1)
% then, selection of the 1st component of the power P and Q
P1 = [];
Q1 = [];
for i = 1:4:length(P)
    P1v = P(i);
    P1 = [P1;P1v];
    Q1v = Q(i);
    Q1 = [Q1;Q1v];
end

% voltage is then computed from power and currents (linear sys)
vdq1 = zeros(381,2);
for i = 1:381
    A = 3/2*[id_test_vct(i), iq_test_vct(i);
    -iq_test_vct(i), id_test_vct(i)];
    B = [P1(i);Q1(i)];

    sol = linsolve(A,B);
    vdq1(i,:) = sol;
end

vd1 = vdq1(:,1);
vq1 = vdq1(:,2);

% solution of a system with two unknowns vd2,vq2 (v-)
P2 = [];
Q2 = [];
for i = 2:4:length(P)
    P2v = P(i);
    P2 = [P2;P2v];
    Q2v = Q(i);
    Q2 = [Q2;Q2v];
end
```

```
vdq2 = zeros(381,2);
for i = 1:381
    A = 3/2*[id_test_vct(i), -iq_test_vct(i);
    iq_test_vct(i), id_test_vct(i)];
    B = [P2(i);Q2(i)];

    sol = linsolve(A,B);
    vdq2(i,:) = sol;
end

vd2 = vdq2(:,1);
vq2 = vdq2(:,2);

% solution of a system with two unknowns vd3,vq3 (v+)
P3 = [];
Q3 = [];
for i = 3:4:length(P)
    P3v = P(i);
    P3 = [P3;P3v];
    Q3v = Q(i);
    Q3 = [Q3;Q3v];
end

vdq3 = zeros(381,2);
for i = 1:381
    A = 3/2*[id_test_vct(i), iq_test_vct(i)
    ;-iq_test_vct(i), id_test_vct(i)];
    B = [P3(i);Q3(i)];

    sol = linsolve(A,B);
    vdq3(i,:) = sol;
end

vd3 = vdq3(:,1);
vq3 = vdq3(:,2);

% initialize flux vectors
Fd = zeros(381,1);
```

```
Fq = zeros(381,1);

for i = 1:381
    Fd(i,:) = ((vq1(i)+vq3(i))/2+vq2(i))/(2*p*wm);
    Fq(i,:) = -((vd1(i)+vd3(i))/2-vd2(i))/(2*p*wm);
end

Fdq = [Fd Fq];

% current maps plots
figure(), hold on, grid on
plot3(Fd,Fq,id_test_vct,'*')
xlabel('\lambda_{d}'), ylabel('\lambda_{q}'), zlabel('i_{d}')
title('i_{d}(\lambda_{d},\lambda_{q})')

figure(), hold on, grid on
plot3(Fd,Fq,iq_test_vct,'*')
xlabel('\lambda_{d}'), ylabel('\lambda_{q}'), zlabel('i_{q}')
title('i_{q}(\lambda_{d},\lambda_{q})')
```

Listing A.2: MTPA,MTPV and constrained maps computation

```
Te      = 3/2*pp*(Fd.*Iq-Fq.*Id);
Fs      = hypot(Fd,Fq);
delta   = atan2d(Fq,Fd);
step    = 5;
t       = 0:step:380;
t(1) = 0.1;

% here variables of insterest must be declared and initialized

for k = 1:size(If,3)
j = 1;
for i = 1:length(t)

    if k == 1
       range_as = find(abs(As(:,1,k)) <= 90);
```

```
    isoT = contourc(Is(1,:,1),As(range_as,1,1),...,
    Te(range_as,:,1),[t(i),t(i)]);
else
    isoT = contourc(Is(1,:,k),As(:,1,k),Te(:,:,k),[t(i),t(i)]);
end

if ~isempty(isoT)
     pos_isoT     = isoT(2,1);
     T_hp         = NaN;
     if pos_isoT+2 <= length(isoT)
          T_hp = isoT(1,pos_isoT+2);
     end

%% no duplicates case
if isoT(1,1) ~= T_hp
     T_av(j) = isoT(1,1);
     Is_isoT = isoT(1,2:end);
     As_isoT = isoT(2,2:end);
end

%% duplicates handling
if isoT(1,1) == T_hp
     ind(1)  = 1;
     val(1)  = isoT(2,1);
     Tval(1) = isoT(1,1);
     T_av(j) = isoT(1,1);

     for l = 2:length(isoT)
          ind(l) = ind(l-1)+val(l-1)+1;

if ind(l) < length(isoT)
     val(l)  = isoT(2,ind(l));
     Tval(l) = isoT(1,ind(l));
end

if ind(l) > length(isoT)
     break
end
```

```
    end

    val      = val(val ~= 0);
    Tval     = Tval(Tval ~= 0);
    ind      = ind(1:length(val));

    dim      = length(ind);

    isov     = isoT(:, ~ismember(1:size(isoT, 2), ind));
    Is_isoT  = isov(1,:);
    As_isoT  = isov(2,:);
end

    %% other electrical parameters
    Fd_isoT      = interp2(Is(1,:,k),As(:,1,k),Fd(:,:,k)...
    ,Is_isoT,As_isoT);
    Fq_isoT      = interp2(Is(1,:,k),As(:,1,k),Fq(:,:,k)...
    ,Is_isoT,As_isoT);

    Fs_isoT      = hypot(Fd_isoT,Fq_isoT);
    AsF_isoT     = atan2d(Fq_isoT,Fd_isoT);

    %% currents
    [Ismtpa_temp, Ismtpa_idx]    = min(Is_isoT);
    AsImtpa_temp                 = As_isoT(Ismtpa_idx);

    [~, Ismtpv_idx] = min(Fs_isoT);
    AsImtpv_temp    = As_isoT(Ismtpv_idx);
    Ismtpv_temp     = Is_isoT(Ismtpv_idx);

    Idmtpa(j) = Ismtpa_temp.*cosd(AsImtpa_temp);
    Iqmtpa(j) = Ismtpa_temp.*sind(AsImtpa_temp);
    Idmtpv(j) = Ismtpv_temp.*cosd(AsImtpv_temp);
    Iqmtpv(j) = Ismtpv_temp.*sind(AsImtpv_temp);

    Ismtpv(j) = Ismtpv_temp;
    Ismtpa(j) = Ismtpa_temp;
    Asmtpa(j) = AsImtpa_temp;
```

```
        %% fluxes
        [Fsmtpv_temp, Fsmtpv_idx]    = min(Fs_isoT);
        AsFmtpv_temp                 = AsF_isoT(Fsmtpv_idx);

        [~, Fsmtpa_idx] = min(Is_isoT);
        AsFmtpa_temp    = AsF_isoT(Fsmtpa_idx);
        Fsmtpa_temp     = Fs_isoT(Fsmtpa_idx);

        Fsmtpa_temp(Ismtpa_temp >= Imax) = NaN;
        Fsmtpv_temp(Ismtpv_temp >= Imax) = NaN;

        Fdmtpv(j) = Fsmtpv_temp.*cosd(AsFmtpv_temp);
        Fqmtpv(j) = Fsmtpv_temp.*sind(AsFmtpv_temp);
        Fdmtpa(j) = Fsmtpa_temp.*cosd(AsFmtpa_temp);
        Fqmtpa(j) = Fsmtpa_temp.*sind(AsFmtpa_temp);

        Fsmtpv(j)   = Fsmtpv_temp;
        Fsmtpa(j)   = Fsmtpa_temp;
        AsFmtpa(j)  = AsFmtpa_temp;

        Temtpa(j) = 3/2*pp*(Fdmtpa(j).*Iqmtpa(j)-Fqmtpa(j).*Idmtpa(j));
        Temtpv(j) = 3/2*pp*(Fdmtpa(j).*Iqmtpa(j)-Fqmtpa(j).*Idmtpa(j));

        j = j + 1;
    end
end

idmtpa_if{k} = Idmtpa;
idmtpv_if{k} = Idmtpv;
iqmtpa_if{k} = Iqmtpa;
iqmtpv_if{k} = Iqmtpv;
ismtpa_if{k} = Ismtpa;
ismtpv_if{k} = Ismtpv;
fdmtpa_if{k} = Fdmtpa;
fdmtpv_if{k} = Fdmtpv;
fqmtpa_if{k} = Fqmtpa;
fqmtpv_if{k} = Fqmtpv;
```

```
fsmtpa_if{k} = hypot(Fdmtpa,Fqmtpa);
fsmtpv_if{k} = hypot(Fdmtpv,Fqmtpv);
temtpa_if{k} = 3/2*pp*(Fdmtpa.*Iqmtpa-Fqmtpa.*Idmtpa);
temtpv_if{k} = 3/2*pp*(Fdmtpv.*Iqmtpv-Fqmtpv.*Idmtpv);
maxTv_if(k) = max(temtpv_if{k});
maxTa_if(k) = max(temtpa_if{k});

end

%% constrained profile
constrained_profile = cell(size(If,3)+1,length(t));
% constrained_profile = {};
for k = 1:size(If,3)

for i = 1:length(t)
    isoT = contourc(Is(1,:,k),As(:,1,k),Te(:,:,k),[t(i),t(i)]);

    if ~isempty(isoT)
        pos_isoT = isoT(2,1);
        T_hp = NaN;
        if pos_isoT+2 <= length(isoT)
            T_hp = isoT(1,pos_isoT+2);
        end

    %% no duplicates case
    if isoT(1,1) ~= T_hp
        T_av(j) = isoT(1,1);
        Is_isoT = isoT(1,2:end);
        As_isoT = isoT(2,2:end);
    end

    %% duplicates handling
    if isoT(1,1) == T_hp
        ind(1)  = 1;
        val(1)  = isoT(2,1);
        Tval(1) = isoT(1,1);
        T_av(j) = isoT(1,1);
```

```
    for l = 2:length(isoT)
        ind(l) = ind(l-1)+val(l-1)+1;

if ind(l) < length(isoT)
    val(l)  = isoT(2,ind(l));
    Tval(l) = isoT(1,ind(l));
end

if ind(l) > length(isoT)
    break
end
    end

    val     = val(val ~= 0);
    Tval    = Tval(Tval ~= 0);
    ind     = ind(1:length(val));

    dim     = length(ind);

    isov    = isoT(:, ~ismember(1:size(isoT, 2), ind));
    Is_isoT = isov(1,:);
    As_isoT = isov(2,:);
end

    l = 0;
    %% other electrical parameters
    Fd_isoT     = interp2(Is(1,:,k),As(:,1,k),Fd(:,:,k)...
    ,Is_isoT,As_isoT);
    Fq_isoT     = interp2(Is(1,:,k),As(:,1,k),Fq(:,:,k)...
    ,Is_isoT,As_isoT);
    Fs_isoT     = hypot(Fd_isoT,Fq_isoT);
    delta_isoT    = atan2d(Fq_isoT,Fd_isoT);

    Id_isoT     = Is_isoT.*cosd(As_isoT);
    Iq_isoT     = Is_isoT.*sind(As_isoT);

    tmp_idmtpa      = idmtpa_if{k};
    tmp_idmtpv      = idmtpv_if{k};
```

```
        tmp_deltamtpv    = atan2d(fqmtpv_if{k},fdmtpv_if{k});
        tmp_deltamtpa    = atan2d(fqmtpa_if{k},fdmtpa_if{k});

        mask1 = ~isnan(tmp_idmtpa);
        tmp_deltamtpv    = tmp_deltamtpv(mask1);
        tmp_deltamtpa    = tmp_deltamtpa(mask1);
        tmp_idmtpv       = tmp_idmtpv(mask1);
        tmp_idmtpa       = tmp_idmtpa(mask1);

        if i <= length(tmp_idmtpa)
           av_range     = find(Id_isoT <= tmp_idmtpa(i)
& ...
                                Id_isoT >= tmp_idmtpv(i)
& ...
                                delta_isoT <= tmp_deltamtpv(i)
& ...
                                Is_isoT < Imax
& ...
                                Iq_isoT >= 0);
        else
            break
        end
        Id_con = Id_isoT(av_range);
        Iq_con = Iq_isoT(av_range);

        Is_con = hypot(Id_con,Iq_con);
        As_con = atan2d(Iq_con,Id_con);

        Fd_con = interp2(Is(1,:,k),As(:,1,k),Fd(:,:,k)...
        ,Is_con,As_con);
        Fq_con = interp2(Is(1,:,k),As(:,1,k),Fq(:,:,k)...
        ,Is_con,As_con);
        Fs_con = hypot(Fd_con,Fq_con);

        [~, sort_idx] = sort(Fs_con,'ascend');
        Id_con = Id_con(sort_idx);
        Iq_con = Iq_con(sort_idx);
        Fd_con = Fd_con(sort_idx);
```

```
        Fq_con = Fq_con(sort_idx);

        constrained_profile{1,i} = t(i);
        constrained_profile{k+1,i} = [Id_con; Iq_con; Fd_con; Fq_con];

    end
end

end

%% evaluating constrained profile maximum length
max_dim = zeros(1,14);
for k = 1:size(If,3)
len = zeros(length(t),1);
for i = 1:length(t)
    l = constrained_profile{k+1,i};
    len(i) = length(l);
end
max_dim(k) = max(len);
end

widht = max(max_dim);

%% building proper maps
% again, variables must be declared and initialized

for k = 1:size(If,3)
    Idcon = zeros(length(t),widht)+NaN;
    Iqcon = zeros(length(t),widht)+NaN;
    Fdcon = zeros(length(t),widht)+NaN;
    Fqcon = zeros(length(t),widht)+NaN;
for i = 1:length(t)
    temp_len = size(constrained_profile{k+1,i},2);
    if temp_len > 0
        tmp_var = constrained_profile{k+1,i};
        tmp_id  = tmp_var(1,:);
        tmp_iq  = tmp_var(2,:);
        tmp_fd  = tmp_var(3,:);
```

```
        tmp_fq  = tmp_var(4,:);

        Idcon(i,:) = cat(2,tmp_id,NaN*ones(1,widht-length(tmp_id)));
        Iqcon(i,:) = cat(2,tmp_iq,NaN*ones(1,widht-length(tmp_iq)));
        Fdcon(i,:) = cat(2,tmp_fd,NaN*ones(1,widht-length(tmp_fd)));
        Fqcon(i,:) = cat(2,tmp_fq,NaN*ones(1,widht-length(tmp_fq)));
    end
end
    idcon_if(:,:,k) = Idcon;
    iqcon_if(:,:,k) = Iqcon;
    fdcon_if(:,:,k) = Fdcon;
    fqcon_if(:,:,k) = Fqcon;

    tecon_if(:,:,k) =  3/2*pp*(Fdcon.*Iqcon-Fqcon.*Idcon);
    fscon_if(:,:,k) = hypot(Fdcon,Fqcon);
    tmp_delta = atan2d(Fqcon,Fdcon);

    %% finding columns associated to zero torque, then set to zero
    zero_T = find(cell2mat(constrained_profile(1,:)) == 0);
    tmp_delta(zero_T,:) = 0;
    delta_if(:,:,k) = tmp_delta;
end
```

Bibliography

[1] E. Armando, I. R. Bojoi, P. Guglielmi, G. Pellegrino, and M. Pastorelli. Experimental identification of the magnetic model of synchronous machines. *IEEE Transactions on Industry Applications*, 49(5):2261–2268, September/October 2013.

[2] S. Rubino, L. Tolosano, F. Mandrile, E. Armando, and I. R. Bojoi. Flux polar control (fpc): A unified torque controller for ac motors. *IEEE Transactions on Industry Applications*, 59(4):4140–4163, July/August 2023.

[3] Marta Schulte-Fischedick and Klaus Hubacek Yuli Shan. Implications of covid-19 lockdowns on surface passenger mobility and related co2 emission changes in europe. *Elsevier, Applied Energy*, 202q.

[4] Professor Dr. Guy Seguier and Professor Dr. Francis Labrique. *Power Electronic Converters*. Springer-Verlag Berlin Heidelberg, 1993.

[5] B. Stumberger, G. Stumberger, D. Dolinar, A. Hamler, and M. Trlep. Evaluation of saturation and cross-magnetization effects in interior permanent-magnet synchronous motor. *IEEE Transactions on Industry Applications*, 39(5):1264–1271, September/October 2023.